Ph.D. Dissertation

Development of Programmable Multi-Channel Low-Power Wireless Microstimulators for Sensory Neural Prostheses

감각 신경 보철물을 위한 프로그래밍 가능한
다중 채널 저전력 무선 미세 자극기 개발

2023 년 2 월

서울대학교 융합과학기술대학원
융합과학부 나노융합전공

이 채 은

Development of Programmable Multi-Channel Low-Power Wireless Microstimulators for Sensory Neural Prostheses

지도교수 송 윤 규

이 논문을 공학박사 학위논문으로 제출함
2022 년 11 월

서울대학교 융합과학기술대학원
융합과학부 나노융합전공
이 채 은

이채은의 공학박사 학위논문을 인준함
2023 년 1 월

위 원 장 이재규 (인)

부위원장 송윤규 (인)

위 원 박원철 (인)

위 원 서종모 (인)

위 원 전상범 (인)

Abstract

Development of Programmable Multi-Channel Low-Power Wireless Microstimulators for Sensory Neural Prostheses

Chae-Eun Lee

Program in Nano Science and Technology

Graduate School of Convergence Science & Technology

Seoul National University

The continued growth of microfabrication technology and the proliferation of wireless devices and systems have broken down barriers to the implantation of electronic devices into the human body. As interest in human neural networks, including artificial intelligence, increases, research on brain interfaces are also being actively conducted. A brain interface is a technology that can analyze or control brain activity or stimulate a neural network generated by an electrical

signal. The technology that artificially encodes desired data by applying an external stimulus to the neural network is being utilized to replace damaged sensory nerves and activate the senses. In general, an action potential is generated by applying an electrical stimulus to a cell from an electrode connected to a brain interface device.

In this dissertation, we develop a multichannel, high-density, low-power, efficient wireless ultra-small stimulator for neural electrical stimulation, optimize the performance of each stimulation target based on this, and design a distributed stimulation system and addressing method for it.

In the case of a system inserted into the body, a multichannel high-density electrode structure is required due to the nature of spatiotemporal dense neural tissue, and optimization of the stimulation method and stimulation threshold is required. The first part of this dissertation briefly introduces the concept of neural network interference by external current stimulation and the development history of stimulation devices and describes the biological and electronic engineering background that requires high-density, low-power stimulators.

Given the basic concept of neural stimulation and the challenges following, a current-controlled current stimulator with a biphasic pulse generator is designed. The second chapter proposes a modified biphasic pulse generator with high output impedance and evaluates the overall performance.

A neurostimulator inevitably requires an analytical instrument to observe the stimulus-response and is integrated into one system in a bidirectional neural interface structure such as a brain-machine interface. At this time, components

such as a recorder, a stimulator, wireless data, and a power transmission/reception stage are integrated into an integrated circuit for the miniaturization of the system. Therefore, we developed and verified a bidirectional brain-machine interface microsystem based on a low-power system for Electrocorticography (ECoG) recording and implanted it in a non-human primate, which is discussed in the third part of this paper.

Finally, the design method and analysis of the distributed stimulation system, including the photodiode address generation circuit, are discussed. The proposed system creates a flexible multichannel stimulator by extending the replication module. In this case, an address to distinguish individual modules is essential. Due to the characteristics of micro-integrated circuits, technologies for minimizing the area of the addressing circuit and encoding after semiconductor processing is required. To this end, an address-generation circuit using a photodiode and an anti-fuse without an aluminum pad is proposed.

Keywords: low-power microstimulator, implantable system, sensory neural prostheses, wireless multichannel stimulator, distributed microstimulator

Student Number: 2017-21784

Table of Contents

List of Figure

List of Table

Note

Parts of the dissertation are extracted and adapted from the journal publications based on the course of this study:

Lee, Chae-Eun, et al. "8-Channel Biphasic Current Stimulator Optimized for Retinal Prostheses." Journal of Nanoscience and Nanotechnology 21.8 (2021): 4298-4302.

Lee, Chae-Eun, et al. "Microscale Wireless Electrical Stimulators for Electroceutical Applications: a Review." Journal of Integrated Circuits and Systems 8, no. 3 (2022).

Lee, Cha-Eun, Jungwoo Jang, et al. “A Wireless 128-channel Recording 32-channel Stimulation Neural Interface Microsystem for Bidirectional Brain-Machine Interface.” (2023)

Chapter 1. Introduction

1.1. Study Background

In the biomedical area, research into artificial manipulation of neural activity by applying electrical stimulation has existed for a long time. Altering nerve activity by targeted stimuli to specific nerve areas in the body, called neuromodulation, works in two types: replacing the function of the damaged network or interposing to treat the malfunctioning network. The first area, called neural prosthetics, is to rehabilitate the nervous system damaged by disease or accident with electronic devices, such as cochlear implants, artificial retinas, and brain-machine interfaces. In the 1980s, as cochlear implants successfully restored hearing, research to apply neural prosthetics to various sensory nerves followed [1], [2]. Brain-machine interface (BMI), for example, attempts to provide feedback from devices to the brain in the form of somatosensory sensations [3]–[5]. The other area, called electroceuticals, stimulates brain or nerve functions with energy, such as electric current or magnetic fields, to produce therapeutic effects. In 1997, the US Food and Drug Administration (FDA) approved DBS for treating essential tremors and Parkinson's disease [6] (followed by approval for dystonia in 2003 [7] and epilepsy in 2018[8]).

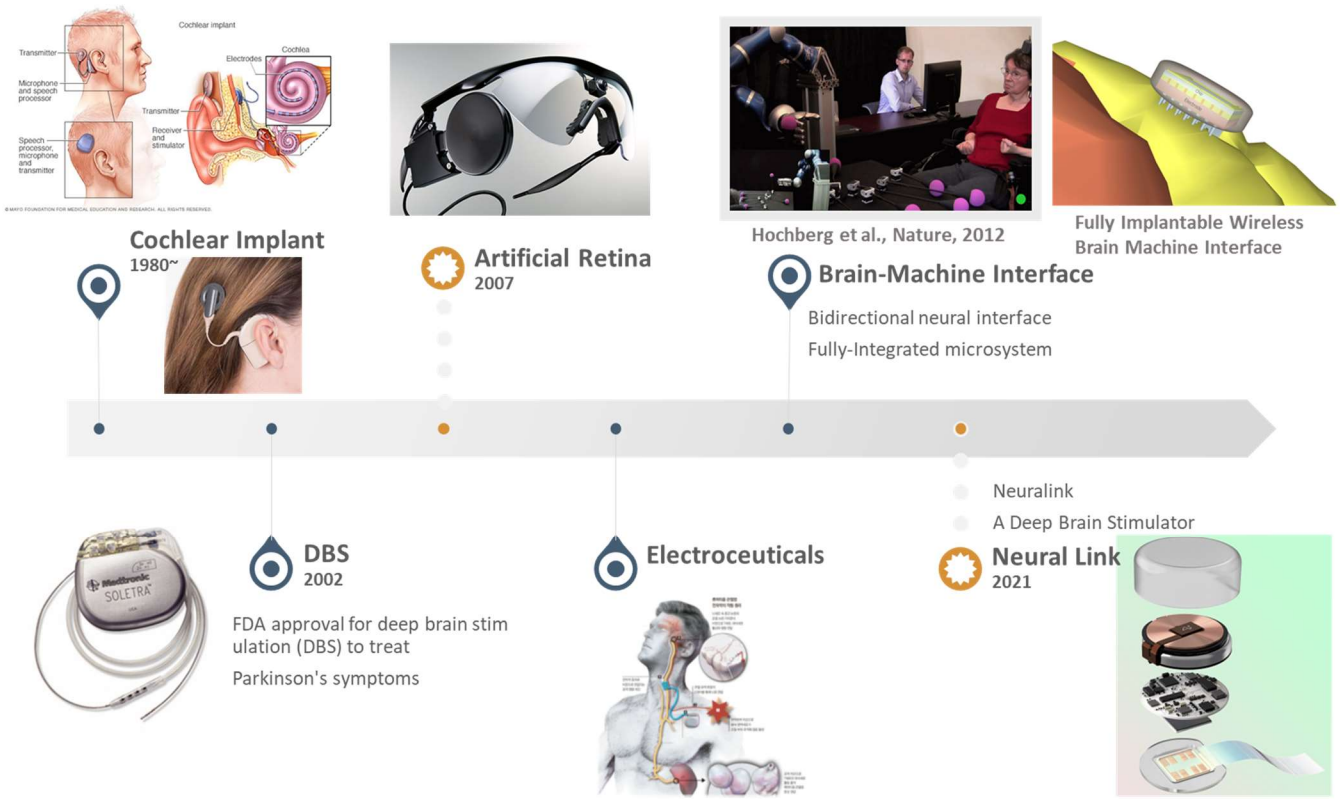

Figure 1. 1. The emergence of neural prosthetic devices and research and development trends over time

Researchers have investigated for many years, and commercialized products are diverse, but several challenging problems still need to be overcome. Figure 1.1 is the timeline of neural prosthetic devices and their emergence. The essence of stimulation is to make the brain believe it is actual neural data. However, it is much harder for the artificial signal to mimic the actual neural data. Because it is hard to generate various neural signals that the brain believes, using a remaining neural network is a possible option. When giving direct stimulation, different types of cells should transmit various neural signals continuously. Figure 1.2 classified the neural prosthetic stimulators associated with two pulse parameters: pulse width and amplitude.

Meanwhile, computing technology that could interpret the brain's electrical activity was developed to give adequate electrical stimulation to the target neuron. Deep neural networks, for instance, are the available option that analyzes the data and provides adequate information for stimulation.

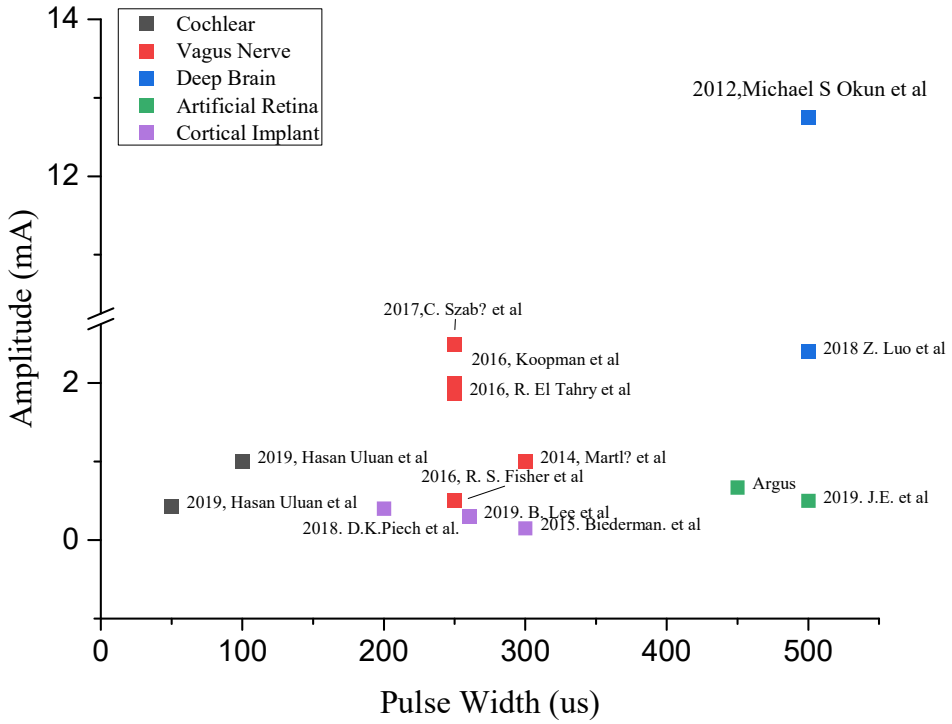

Figure 1. 2. Distribution according to the current size and pulse width of the stimulator developed for each application

1.1.1. Stimulation Mechanism

The mechanism of stimulation is to elicit an action potential (AP) regulated by an ion channel in a nerve in the form of an electromagnetic signal. Modifications or intermediates for signal conversion are needed to interact with the neural network. Optogenetics, for instance, genetically encodes the target neuron with a light-sensitive ion channel to control its activity with light. Similarly, ultrasound as an external source needs a material that can produce electric energy upon application of mechanical stress, such as piezoelectric materials.

The generation of an action potential in neurons through electrical stimulation is achieved by delivering a sufficient charge to its membrane. Charges move at the interface between the electrode connected to the system and the tissue when current stimulation is applied. At this time, when the transferred charges accumulate, the Na+ channel of the nerve cell opens. As the excess charge accumulates outside the cell membrane, a potential reversal occurs, triggering an action potential (Figure 1.3). At this time, a positive charge exceeding the threshold must be applied to cause an action potential. The action voltage generated by nerve cells is about 0.1 V and occurs for about 1/1000 second.

The length and amplitude of an action potential are always the same. However, increasing the stimulus intensity increases the frequency of action potentials. Action potentials propagate along nerve fibers without reducing or attenuating amplitude or length. The response of the stimulation propagates in

one direction and is generated by the ion channels. Since a series of processes consume the time of one cycle, action potentials may not be generated if the following stimulus is applied within one cycle. Therefore, the energy efficiency of electrical stimulation is highly dependent on the generated voltage and current waveforms and the electrodes' characteristics.

Given the mechanism of the action potential, various approaches to manually generate action potential were investigated. Charge injection stimulation is the most direct approach to delivering desired action potentials. On the other hand, voltage gradient stimulation uses voltage and electric fields across the target to move ions. It is less efficient than charge injection. As a disadvantage, since the charge is dispersed along the surface, it is better to direct the E-field with the return electrode.

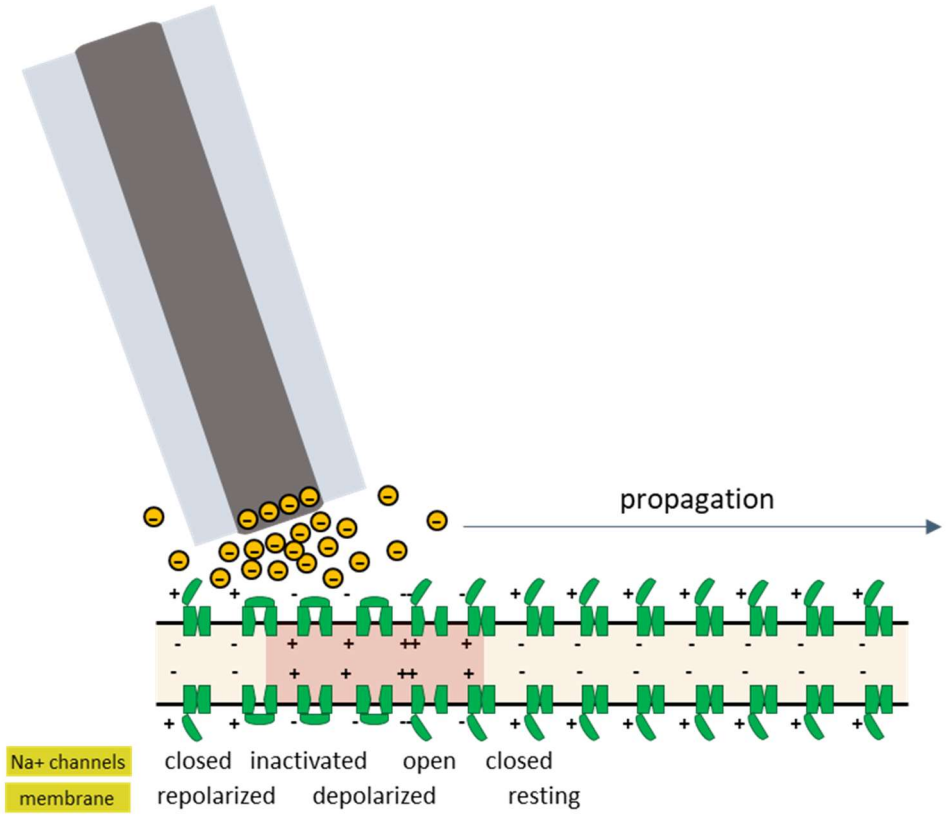

Figure 1. 3. Electromagnetic stimulation mechanism

The extracellular stimulation injects current into the tissue of interest (TOI) using electrodes placed nearby. On all neurons' surfaces (cell membrane), there are more negative ions than positive ions inside and more positive ions than negative ions outside, so a potential difference (voltage) occurs between the cell membranes.

1.1.2. Stimulation Model

In order to accurately calculate the applied charge in the system, it is necessary to model the electrodes, the electrode-tissue interface, and the tissue itself, which can be configured with capacitors and resistors, as shown in Figure 1.4. The amount of charge arriving at the target point can be calculated by adjusting the system's output. The electrode and tissue interface contributes to the charge per phase of a stimulus pulse and charge density. Building an interface model helps estimate the average charge delivered to the target. The charge density calculation according to the electrode's surface area employed the Shannon equation [9]. The impedance of the electrode-tissue interface, which the stimulator gets as the load, is as follows:

$$Z_C = R_S + \frac{R_f}{1 + j\omega C_{dl} R_f}$$

where a capacitance (C_{dl}) is formed between the electrode and tissue, the model also has a parallel charge transfer resistance Rf that accounts for reactions and exchange currents that result at the interface. Both C_{dl} and R_f are electrode material dependent and scale with the effective surface area of the electrode, with the capacitance increasing and the resistance decreasing.

The calculation is based on a single electrode. Additional impedance occurs at the interface between the tissue when inserted into the living body (Figure 1.5). The tissue damaged by the electrode, such as scar tissue, sticks to the surface, and the interface impedance further increases. While the Shannon equation has proved helpful in assessing the likely occurrence of tissue damage, it is hard to get the exact impedance that the stimulator feels. In particular,

microelectrodes do not abide by the charge per phase and charge density co-dependences reflected in the Shannon equation [9].

The key to stimulation is that the required amount of stimulation charge arrives at the target. The amount of current going out to the output multiplied by the total impedance is the compliance voltage applied to the system. The smaller the size of the electrode, the larger the compliance voltage for the same output current. It uses various design techniques to supply considerable voltage headroom to endure the large load impedance. However, this type of technology also increases power consumption and ASIC size.

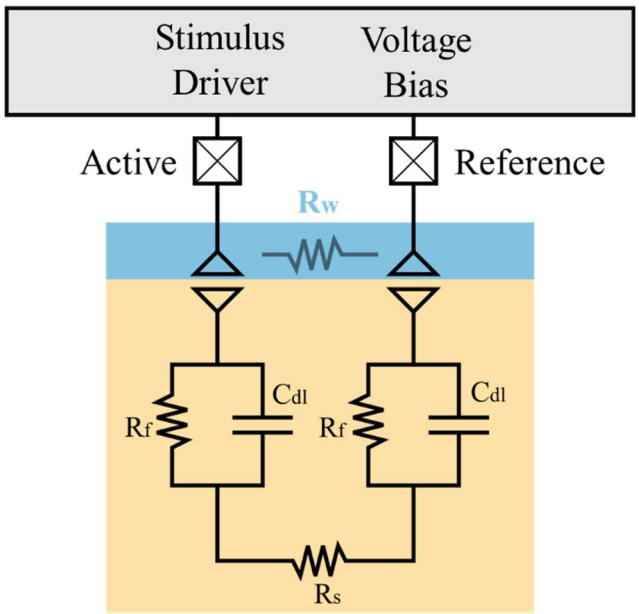

Figure 1. 4. Equivalent circuit model of the electrode-tissue interface

Since the bipolar configuration is equivalent to having the active and reference electrodes connected in series, the stimulator senses a doubled impedance. Although the tissue's resistance is relatively high (>1 MΩ) to the stimulator, the capacitance of the electrolyte reduces it.

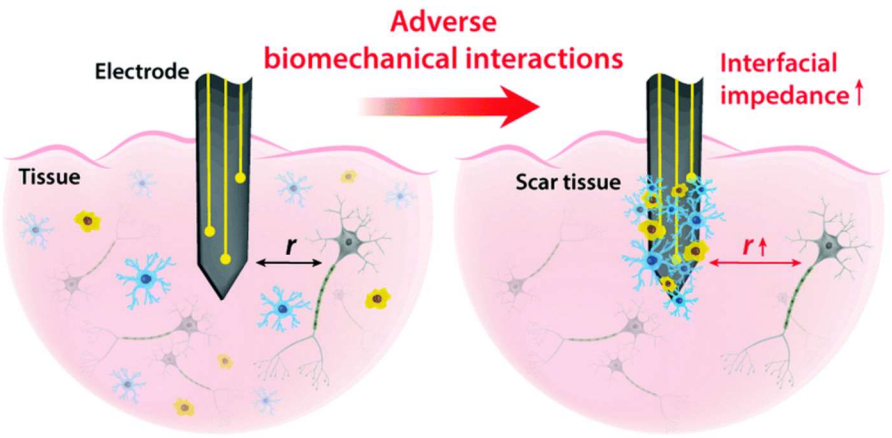

Figure 1. 5. Description of impedance variation at the electrode-tissue interface [10]

After the electrodes are inserted into tissue or placed near it, the emission of the electromagnetic stimulation waveform creates an electrolytic environment. The delamination and corrosion of the electrode and scar tissue from biomechanical interactions increases the interfacial impedance.

1.1.3. Stimulation Methods

Stimulation methods differ in their output source type: Constant voltage (CV) stimulation and Constant Current (CC) stimulation. After determining the stimulation structure, nerve stimulation was achieved by the electrical stimulation waveform from CV or CS stimulators. As shown in Figure 1.6, CV gives output voltage in parallel at the bipolar electrode or between the active and the reference, while CS delivers current regarding the output interface as a series connection.

CV was used in medical devices in the past due to its simple structure, but clinical trials showed that patients preferred CC stimulation and pain relief over CV stimulation and felt satisfied [11], [12]. Compared to the same results, CC stimulation is mainly used because it has advantages such as excellent charge control, calibration accuracy, and stimulation efficiency. It is also believed that CC stimulators provide a constant charge regardless of changes in the impedance of the electrode-tissue interface. CC stimulators also have disadvantages. It is easy to observe current mismatches that cause charge imbalances in the output stage. In addition, even if the amount of charge reached is calculated through impedance modeling, it is affected by environmental variables before moving to the neuron. Recent studies have demonstrated strategies to address this issue in addition to primary stimulation ICs.

The stimulation pulse shape is also an important part that affects the result. Monophasic pulses were generally used in clinical trials. However, considering charge neutrality after long-term stimulation, researchers worried about charge

stacking at the surface, which causes tissue damage and electrode erosion. Even calcium deposits in electrolytes can occur near the electrodes if the charge is continuously injected. Furthermore, charge balancing biphasic pulse is more favored to prohibit the increase of the DC offset. Recent studies have shown that the negative-phase first, then positive-phase charge injection seems more effective in generating action potentials [13]. Also, stimulation with ultra-short pulses effectively opens the sodium channels [14].

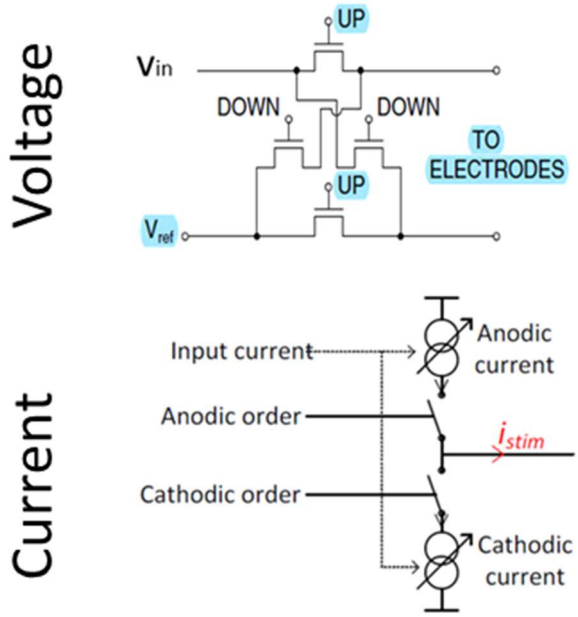

Figure 1. 6. Circuit diagram of two different stimulation sources: Constant voltage stimulator and Constant current stimulator

The stimulation source is again classified with the modulation method. The current-controlled current source and the voltage-controlled current source show different performances at charge control and power consumption.

1.1.4. Stimulator architecture

The waveform is determined based on the circuit structure of the output stage and the form of the electrode combined. Table I illustrates details of microstimulators in different architectures. Electrode connections in bipolar and monopolar electrodes are a widely chosen architecture for neuromodulation. Mostly CV stimulators take bipolar structure, while CS stimulators have relative freedom of choice. Both formats have all the pros and cons in the application, hence selected based on their purposes. The bipolar configuration needs pairs of electrodes and stimulates a limited area while exhibiting a greater compliance voltage because of the circuit structure.

The electrode's size and impedance must also be considered prior to the electrode configuration. Size should be small enough compared to the neural cells (~10 μm) to ensure selective stimulation and charge density, while impedance should be low enough to permit effective stimulation. The charge density is determined by the amount of the charge executed and the apparent area of the electrode interface. Conventionally, if the size of the electrode interface reduces, the impedance and the load on the stimulator increase. Therefore, it is vital to find a suitable compromise between them.

In addition to the physical structure of the stimulator, current steering stimulation started with the concept of increasing virtual channels for effective stimulation. Usually, cochlear implants investigate virtual channel discrimination to increase spectral resolution [15], [16]. In cochlear implants, simultaneous stimulation of adjacent physical electrodes creates virtual channels by current steering [17]. Some studies assessed whether this method

could be adapted for retinal implants [18]. In 2009, researchers compared the area of cortical activation by hexapolar, bipolar, and tripolar current steering techniques [19]. The result indicated that the architecture of electrodes affected the concentration area with the proven result of the hexapolar electrode.

Table I Comparison of microstimulator in diverse architecture

	[20]	[21]	[22]	[23]	[24]	Our System
Stimulation Type	Current controlled (CCS)	Current controlled (CCS)	Current controlled (CCS)	High-frequency, switched-capacitor	Current controlled (CCS)	Current controlled (CCS)
Supply	3.3 V	3.2 V	Adaptive (~3.3 V)	1.8 V	1 V	3.3 V
Voltage compliance	± 6 V	12.8 VHV	6.7 – 12.3 V	5 V	2.5 V	3 V
Charge balancing method	Discharge (Electrode shorting)	Modulation (Anodic current modulation & electrode shorting)	Discharge (Electrode shorting)	Discharge (Electrode shorting - active charge balancing)	Passive charge balancing	Modulation (Anodic current modulation)
Current	± 3 mA	1 mA	2.4 mA	34 nC and 120 nC	60 µA – 1.86 mA	40 – 330 µA
Pulse width	60 µs, 10 µs interphase delay	100 µs with 20 µs of interphasic	0.5 ms pulse width, 2.5 ms period	2.37 µs clock period	9.5 – 304 µs width, 9.5 – 304 µs delay	100 µs – 2 ms
Target	Parkinson's disease	Universal use	DBS	DBS	Hippocampal CA1,3	Cortical
Stimulus	Monopolar biphasic	Bipolar Biphasic	Biphasic	Biphasic	Biphasic	Biphasic
technology	180 nm LVCMOS	180 nm CMOS	180 nm LV CMOS	180 nm HV CMOS	130 nm CMOS	180 nm TSMC CMOS

1.2. Neural Prostheses

1.2.1. State of Arts

Through the ex vivo experiments or the preclinical trials, the stimulator's characteristics and stimulation methods have built a database for each target neural network. With the advantage of realistic signal generation and a safer method than direct brain stimulation, most sensory neural prostheses use the remaining neural network for rehabilitation. Various US FDA-approved implantable medical devices (IMDs) have shown their effectiveness with clinical results. However, their design mechanism remains the same: small, low-power devices for long-term implant.

A cochlear implant is a well-known successful sensory prosthesis for hearing impairment developed since the 1970s [25]. The multichannel implant consists of an internal insertion device and an external signal-processing device. An external device extracts the audio information in the acoustic signal and processes it to produce a decoded version of the electrical stimulation signal transmitted as a radio frequency (RF) signal to the receiver-stimulator. The RF signals transmitted by the external sound processor are decoded into electrical impulses that stimulate the auditory nerve through electrodes in an internally implanted device providing various stimulation sites within the cochlea. The high-rate stimulation provides sound information around the patient to the brain along the auditory nerve [26].

When the function of the central nervous system, the cranial nervous system, is damaged, various nervous system diseases such as stroke, depression,

epilepsy, and Parkinson's disease occur, and the damaged function can be replaced with artificial nerve stimulation. This treatment, called neuromodulation, has been proven effective and operates under FDA approval. Deep brain stimulation (DBS) is considered an alternative surgical treatment for patients with long-term complications such as refractory tremor or levodopa-induced motor agitation and severe dyskinesia [27], [28]. The depth probe stimulates the thalamic region with electrical stimulation.

Retinal prostheses Argus II [29], [30] and Alpha IMS [31], [32] are the most popular state-of-the-art retinal prostheses acquiring the US FDA approval and the European CE mark, respectively. The key to this device is to mimic the function of the retina, which converts and transmits external light into bioelectrical signals that the human nervous system can interpret. The composition of the retinal prostheses could be divided into an image acquisition unit, an image processing unit, a signal transmission unit, a nerve cell stimulation unit, and a power supply unit, according to the function. Depending on the position of the stimulator, it can be divided into subretinal and epiretinal stimulators, optic nerve stimulators, and optic cortex stimulators that stimulate the post-retinal area (Figure 1.7).

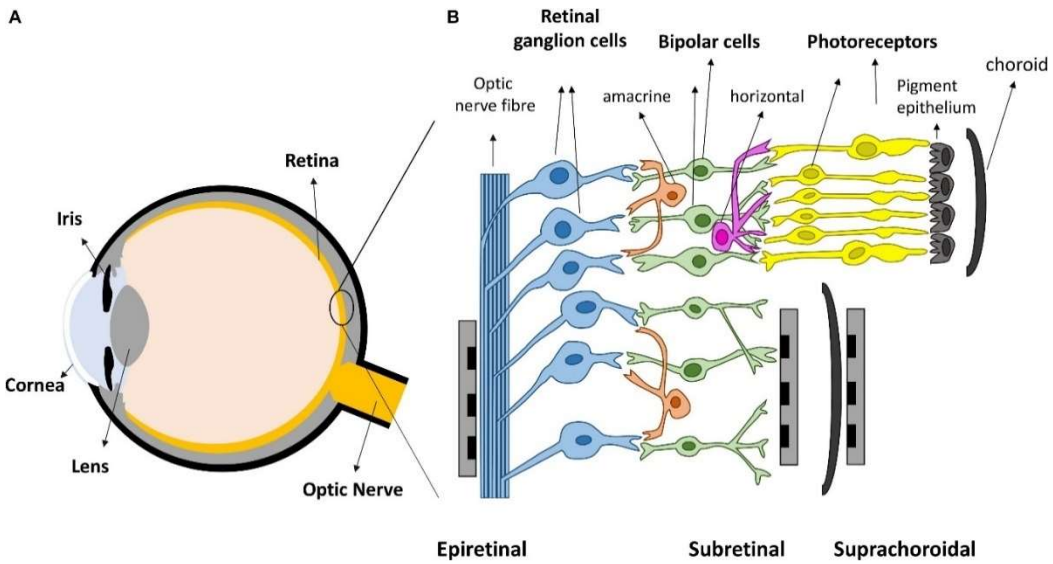

Figure 1. 7. Detailed illustration of an eye in curvature form.

Type of retinal prostheses according to the position of the electrode. The human retina is a radius 12 mm sphere [33]

The neural stimulator electrically activates the nerve cells by directly contacting the nerve cells of the retina remaining after the photoreceptor cells are damaged. Numerous wireless telemetries have been adopted to deliver processed image data and power to the implanted stimulator. A low-power and high-efficiency system are essential above all else because it must provide for an extended period of direct contact with thin and dense optic nerve cells.

Direct electrical stimulation on the cortex has been attempted in some research to evoke sensory information. Especially textile neural prostheses have been investigated in both peripheral and cortical stimulation, yet US FDA has not approved much. The rehabilitation mechanism uses external pressure sensors to acquire textile information.

Table II briefly states the IMD used worldwide for neuromodulation. The common characteristics are the key design factors of the stimulator used for IMDs. Details vary slightly depending on the target tissue and disease.

Table II State-of-arts in FDA-approved IMDs

Devices		Cochlear™ Nucleus®	Vercise™	Argus II [29]	Alpha IMS [34]
Target		Cochlear implant	DBS	epiretinal implant	subretinal implant
Stimulation Type		Biphasic current	Biphasic voltage	Biphasic current	Monophasic voltage (Induced biphasic current)
Power Source		Rechargeable battery with RF coil	battery-powered	RF coil ~1 mW	RF coil ~1 mW
Communication		BLE	Closed-loop	RF modulation	RF modulation
# of Channels		22 active	1-4	60	1500 (72 μm square)
Stimulus	Freq.	250-3,200 pps*	HFS >100, mostly 130 or 150 Hz LFS <100, mostly 60 or 80 Hz	3-60 Hz	5-7 Hz
	Pulse Width	<0.1 ms	60–450 μs	0.45 ms	1 ms
	Amp.	<1.75 mA	2-4 V	4-677 μA	2 V, (charge: 1-5 nC)

* pulse per second

1.2.2. Wireless Power Transfer of IMD

Various wireless communication technologies have been applied in implantable medical devices (IMDs). Since the late 1950s, batteries have long been the primary power source for IMDs. Using a battery as a power source avoids exposing internal tissues to the extracorporeal environment due to the wire, thus exempting it from a potentially infectious and hazardous environment. Nevertheless, there are some limitations in using the battery, which makes it unsatisfying to use it as a sustainable power source. First, batteries have a finite lifespan and must be replaced after the total energy stored has been exhausted. Since the IMD is usually inserted deep into the body, invasive surgery is required to replace the battery after it runs out. Therefore, patients usually avoid it because of the risks, pain, and lengthy recovery times involved. Also, depending on the location, keeping a commonly used lithium-ion secondary battery in the body is considered a potential risk. It is clearly seen that the total energy and lifetime of the battery decrease proportionally as the size of the implant decreases [35]. This battery dilemma remains a significant challenge in providing sufficient power for long periods.

Therefore, IMD requires a wireless power transfer system to provide a stable supply voltage in a relatively small size. As shown in Figure 1.8, various source was developed and verified their performance. Paring with their external device, researchers have modified the system architecture to adjust to their application.

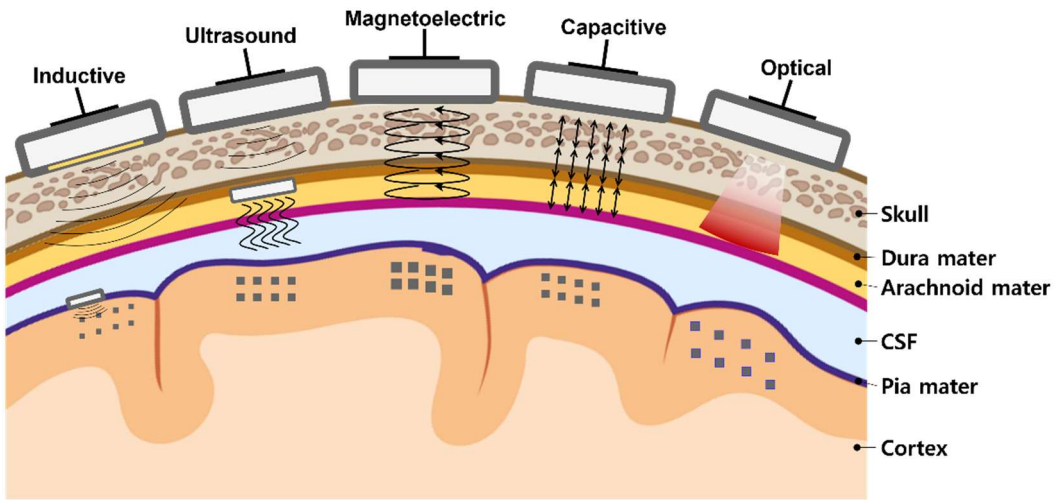

Figure 1. 8. Wireless telemetry with various methods

Considering the environment around the implant, wireless power and data transceiver has been investigated by adopting different source adequate for their application.

Several electromagnetic (EM) power transmissions are considered viable power sources for IMD implants. Inductive coupling, resonant magnetic coupling, capacitive coupling, and RF-based wireless power transmission are four primary methods developed. Each design has a different link design and suffers from various challenges.

Near-field resonant inductive coupling is one of the most advanced and widely used approaches for wireless energy transfer [36]. This technology is characterized in that the charger and the battery are charged only when they are in close contact, and there is little freedom in the arrangement of the mobile device. A transmitting coil (TX) placed close to the skin produces a time-varying magnetic field, which induces an electromotive force (EMF) in the receiving coil (RX) placed inside the body. A change in current in the primary coil causes a change in the magnetic field, and a phenomenon in which counter-electromotive force is generated in the secondary coil is used.

The resonant magnetic coupling is a technology for further extending the distance limit of the magnetic induction method. It is the same as the magnetic induction method in that the magnetic field generated in the primary coil induces the current in the secondary coil. However, the difference is that energy can be transmitted over a longer distance if the resonant frequencies of distant coils match. Thus, coils whose resonant frequencies do not match would not respond to field change.

In a similar context, capacitive coupling transmits electric power by creating a displacement current using an electric field generated between two electrodes. As shown in Figure 1.9, the AC electric field applied at the primary

electrode creates a displacement current in the capacitor generated by the two electrodes. The desired DC voltage is regenerated through the rectifier using the AC voltage from the displacement current at the second electrode [37].

The electromagnetic wave method uses an antenna with high directivity, and it is possible to secure a sufficient transmission distance by utilizing a far field. However, since it uses fundamentally radiating energy, it has a very low efficiency (transmission efficiency of 1% or less) and uses a high frequency.

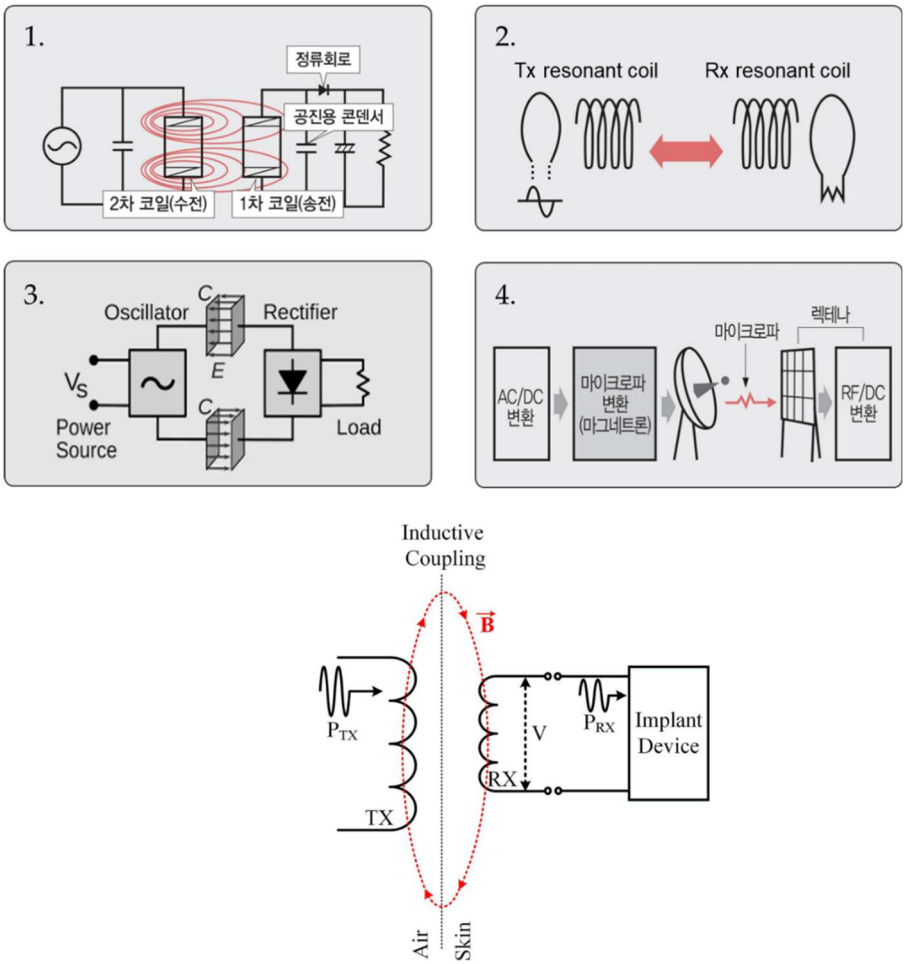

Figure 1. 9. Simplified diagram of WPT to the implant

The first block depicts near-field inductive coupling. The second is resonant magnetic coupling, while the third is capacitive coupling. The mid-field EM radiation on the fourth block uses a directional high-frequency EM field. The circuit model below the blocks shows the WPT interface of the implant device using inductive coupling [36]

Near-field inductive coupling is more widely employed in medical implants due to its high-power transfer efficiency (PTE), the power delivered to load (PDL), and low energy absorption by living tissue using low frequencies (< 0.5 GHz). It works according to the principle of EM induction. A transmit coil (TX) located close to the skin generates a time-varying magnetic field that induces an electromotive force (EMF) in a receive coil (RX) located inside the body, as shown in Figure 1.9. The following equation calculates the PTE of such an inductive link:

$$PTE = \frac{k^2 Q_1 Q_2}{1 + k^2 Q_1 Q_2}\left(\frac{R_{P,2}}{R_{L,ac} + R_{P,2}}\right)$$

where k is the coupling coefficient, Q_1 and Q_2 are quality factors of the transmitter and receiver coils, R_1 and R_2 are the equivalent resistance modeling the losses of the primary and secondary coil, and $R_{L,ac}$ is the load resistance [38].

When an alternating current passes through the Tx coil, the moving charge creates a magnetic field that fluctuates in strength because the amplitude of the current fluctuates. It produces a current by Faraday's law of induction on the Rx coil. Angular misalignment and tissue absorption cause low power transmission efficiency. Giving power under the SAR limitation [39], [40].

1.2.3. Wireless data transmission

Near-field communication is short-range wireless connectivity that utilizes magnetic field induction to enable communication between the external device and the implant with a lower data transfer rate. Inductors are coupled to each other to exchange data through mutual inductance. In data transmission, a voltage proportional to the current change in the transmitting end is applied to the receiving end. The amount of voltage delivered depends on the change in transmit current and mutual inductance in the case of an ideal inductively coupled channel.

Figure 1.10 is the three representative data transmissions through carrier frequency modulation. Each method loads data by intentionally modulating different elements of the RF signal, such as amplitude, frequency, and phase.

Backscatter modulation is load modulation, as shown in Figure 1.11. The mechanism of backscatter communication is simple. Modulating the load connected to the coupled coil creates the decoupling of two coils. The transmission coil detects the electromagnetic wave's distortion and decodes it into serial data.

One radio is a custom wideband Frequency Modulation (FM) architecture for low power and high data rate only used for neural recording that can broadcast up to 128 channels in real-time.

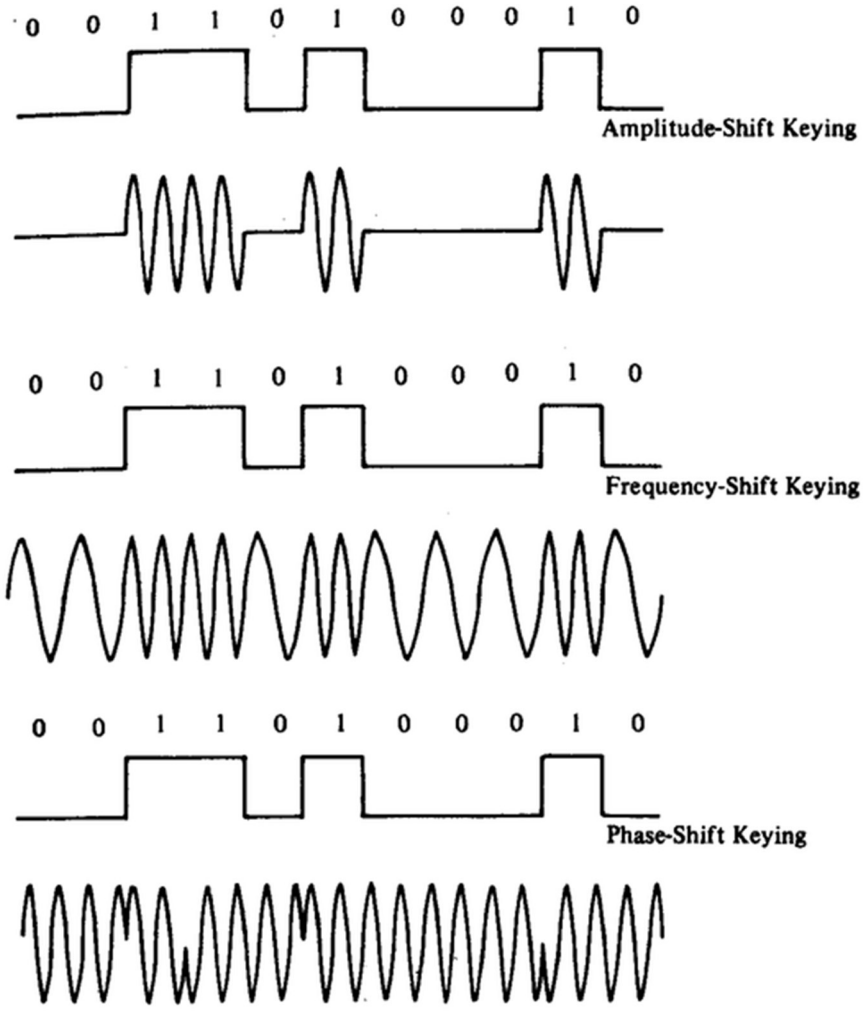

Figure 1. 10. RF modulation technology for data transmission

ASK, FSK, PSK modulation with the single carrier frequency.

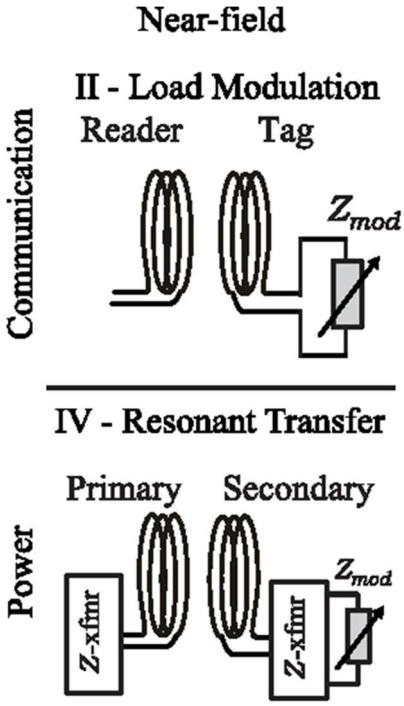

Figure 1. 11. Backscatter modulation in near-field data and power transmission

Losses associated with resonating capacitors and the mini-loop coils (together making the impedance transformer) can be taken into account by looking at the S_{21} of the link. This figure is modified from Besnoff et al. in 2016 from IEEE Transactions on Microwave Theory and Techniques [41]

On the other hand, radio transmission, which Bluetooth and Wi-Fi use, works over long distances at higher speeds and creates connections with multiple devices simultaneously. UWB transmitters such as Wi-Fi could transmit data of 128 channels or more to the outside at a high sampling rate and enable bi-directional or multiple communication. However, to be used as a device for implantation in the body, there are disadvantages in that it consumes relatively large amounts of power, and the system size is bulk. Conversely, mid-range communication modules such as Bluetooth or ZigBee have the advantage of being able to lower power to a level similar to that of coil communication. However, there is an explicit limitation to the data rate, and it needs a separate module for bidirectional communication.

In a wireless communication system, the link margin (LKM) means that the system could tolerate an additional power (dB) of attenuation between the transmitter and the receiver, which would still barely work. For instance, the Bluetooth modules compared in Table III have shown a link margin of 92.

Table III Commercially available bidirectional communication devices

Ref	Protocol	Data rate	Output power
[42]	Bluetooth	2 Mbps	3 dBm
[43]	Bluetooth	2 Mbps	3 dBm
TI CC2520	ZigBee	250 Kbps	0 dBm
[44]	Wi-Fi	16 Mbps	23 dBm
[45]	Wi-Fi	1.6 Mbps	12 dBm
[46]	UWB transmitter	128 Mbps	27.4 dBm

1.3. Dissertation Organization

This dissertation addresses design methods and evaluation of the application-based programmable microstimulator.

In chapter 2 of Stimulator ASIC Optimization for Artificial Retina, the optimization procedure of the stimulator is introduced. After the introduction of the overall system in chapter 2.1, the design method of circuits, including the high impedance output stage, is proposed in chapter 2.2. The benchtop device characterization and ex-vivo experiment results are discussed in detail in chapter 2.3. The following chapter 2.4., summarizes the evaluation results.

Chapter 3: Multichannel Stimulator for Bidirectional Neural Interface is arranged in a similar order as chapter 2, showing the considerations for BMI in 3.1, circuit descriptions in 3.2, benchtop and animal experiment set up in 3.3, device characterization and experiment results in 3.4, and the summary in 3.5.

Chapter 4 discusses the design of distributed microstimulator with a proposed ID-generation circuit, followed by a discussion on how this device can be further improved in terms of extensibility and dimensional miniaturization. The chapter also deals with encoding methods regarding photodiode-based ID generation.

The dissertation is finished with a concluding paragraph for summary and future works in chapter 5.

Chapter 2. Stimulator ASIC Optimization for Artificial Retina

2.1. Introduction

Artificial retina, a well-known device to replace the damaged visual processing neural network, has been developed for decades after the grand success of the cochlear implant. Despite a near-total loss of photoreceptors (PR), such as the final stage of Retinitis Pigmentosa (RP) and age-related macular degeneration (ARMD), inner nuclear and retinal ganglion cell (RGC) layers are partially preserved. Restoring vision by electrical stimulation of the surviving neurons may be viable as a vision recovery in retinal degenerative diseases. Some retinal prostheses have successfully reached the clinical trial stage [29], [31], [47], [48]. However, these devices can only partially restore vision and are insufficient to allow the patient to perform daily activities independently. Prosthetic vision requires acuity, contrast, and spatiotemporal resolution. The lack of these requirements is due to engineering and physiological issues such as the low spatial resolution of the hardware or lack of physiological understanding of the retinal network.

For the stimulation ASIC to overcome these problems and further improve the visual resolution of retinal prostheses, it is more important to apply them based on understanding retinal ganglion cells and visual perception. Understanding how the visual pathway and the stimulation work on neural

networks help the stimulator to give proper stimulus to the brain. Douglas, a retinal implant recipient, once said, "You need to understand that prosthetic vision is fundamentally different than a natural vision."

The retina comprises the nerve, glial, and color-sensing cells, the cones. Figure 2.1 shows visual pathways in the retina. Photoreceptor cells at the bottom of the retina convert light signals into bioelectrical signals that the nervous system can interpret, and these signals are transmitted to retinal ganglion cells through bipolar cells and horizontal cells. Optic nerve fibers originating from ganglion cells gather at the optic nerve head to form the optic nerve.

Mediating retinal ganglion cell spike rates using high-frequency electrical stimulation. Several design issues, such as selectivity and low power consumption, are due to the dense tissue of RGC, as shown in Figure 2.2. RGCs are classified into two different cell types: ON cell and OFF cell. The two cells show distinct responses to light stimuli in the visual pathway [50]. However, the electrical stimulation on RGC evokes the same action potential simultaneously. The researcher has found that a wide frequency range of current stimulus could individually activate each RGC type (ON-OFF cells) [51].

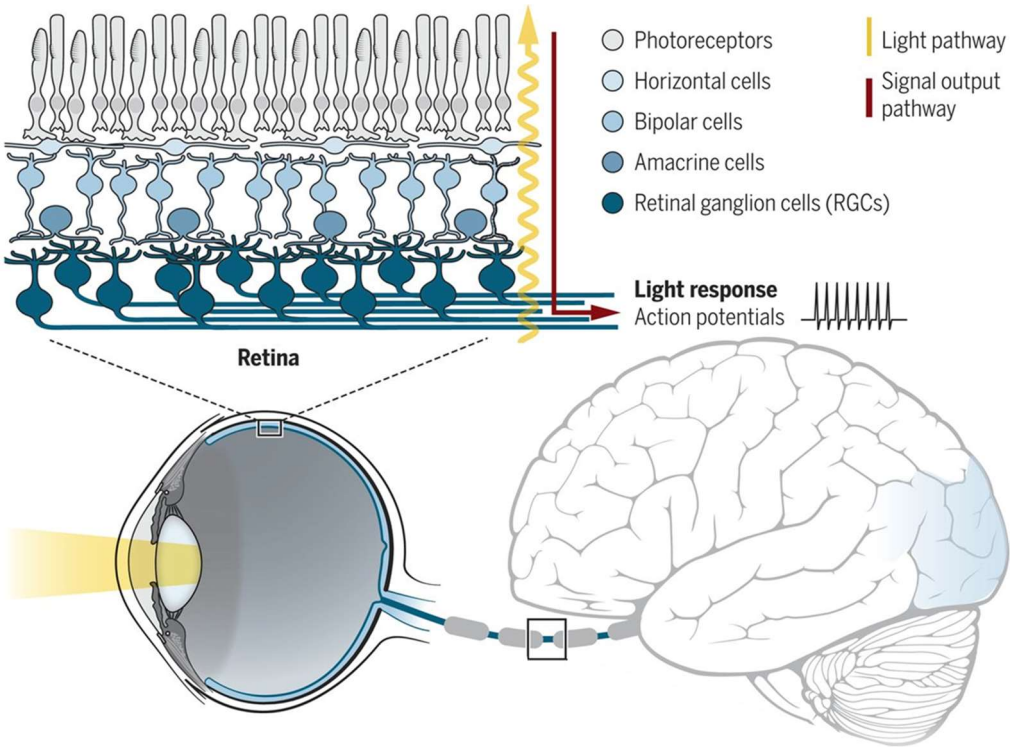

Figure 2. 1. Pathway of the visual perception

The RGC is protected by the sclera, a thick, durable tissue that lines the back of the eye [49]. Even if the photoreceptor converts the light signal into an electrical signal and transmits it to the RGC, the brain cannot perceive visual information unless the RGC combines the information and transmits it to the optic nerve. Therefore, studying how RGC processes nerve signals into visual information is essential.

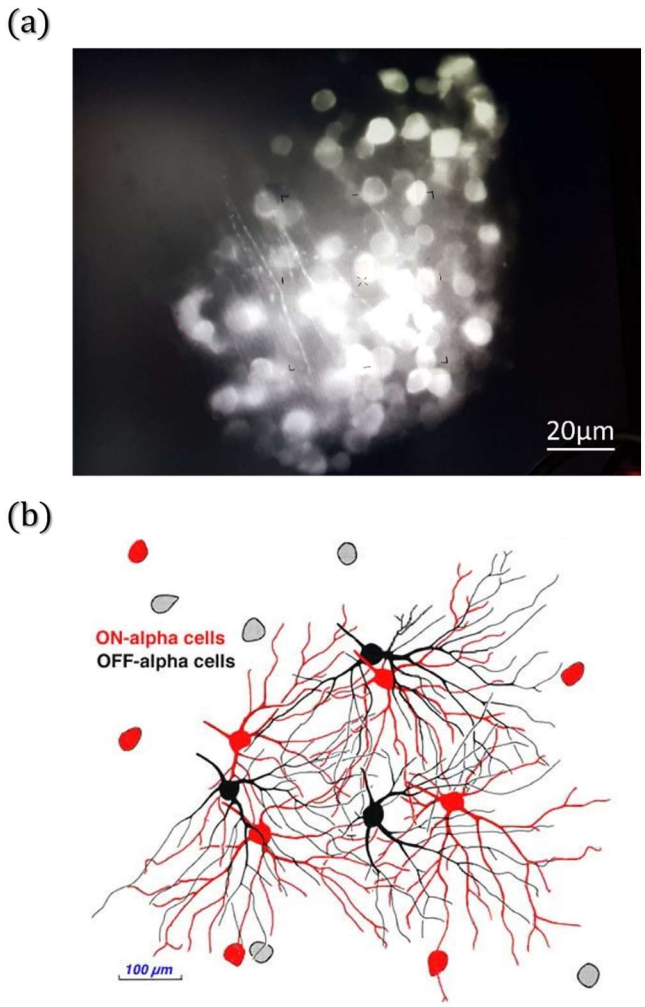

Figure 2. 2. Population and density of two different retinal ganglion cells (a) microphotograph of retinal ganglion cells. (b) ON-OFF cell [52]

Meanwhile, the electrode and cell distance must be shorter than between the adjacent electrodes. As shown in Figure 2.3, the retinal ganglion cells are densely packed, and since the stimulation environment targets the tissue surrounded by electrolytes, the current spreads to the stimulation point and unwanted areas. Smaller electrode sizes to selectively reach a single RGC would enhance the electrode impedance, which requires higher compliance voltage and power from IC. It is a problem that must be overcome in sensory neural prostheses that require high spatiotemporal resolution. There was preliminary research to handle the issues by modifying the structural form or materials of the electrode [53], [54]. A three-dimensional electrode allows the electrode to approach close to the target cells. Also, it enlarges the surface area, which minimizes interface impedance. However, an increase in impedance is inevitable in long-term implants. As previously mentioned, electrode erosion or the scar tissue's attachment is usually the leading cause.

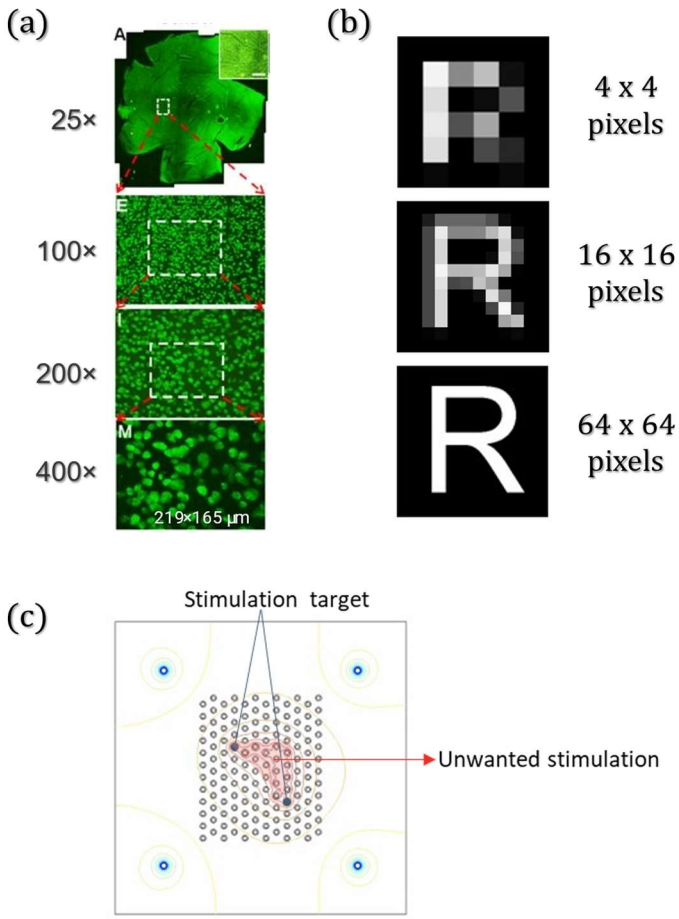

Figure 2. 3. Dense retinal ganglion cells are observed through the microscope camera. (a) the population of retinal ganglion cells observed with different resolutions [55] (b) spatial resolution requirement in pixels (c) population retinal ganglion cells and stimulation charge propagation

Also, there are limitations in current injection for sufficient stimulation of target cells, considering electrolytes between the tissue and the electrode. Understanding the threshold charge to evoke action potentials and delivering the minimal charge to the interface are optimal strategies for neural stimulation with lower power consumption. Furthermore, limitations on power consumption exist to restrict heat dissipation from the system and RF-induced heating. In addition, since the system is inserted into the body, it can cause thermal tissue damage due to RF communication and stimulation, so a low-power system is required.

We propose a programmable microstimulator with fully integrated wireless power and data telemetry. The sub-mm-sized current stimulator features an extensible architecture with optimized stimulus for RGCs. The response and the stimulation site analysis have been conducted with analytic tools such as deep learning.

2.2. Circuit Description

The system circuit diagram consists of 8 biphasic pulse generators with current DAC, controlled by digital logic. Figure 2.4. illustrates a block diagram of the designed IC and test board. Xilinx FPGA module transmits serial binary bit command, clock, and reset signal to digital logic. The power circuit with 13.56 MHz carrier frequency uses a bridge rectifier with 4 diodes and a low-dropout (LDO) regulator for a 3.3 V supply.

A bandgap voltage reference is a temperature-independent circuit that produces a fixed voltage regardless of power supply variations, temperature changes, or circuit loading from a device. In the IC, the bandgap voltage reference circuit made of a resistor and CMOS transistors generates a fixed voltage of 1.22 V. From that reference voltage, the current digital-analog converter (iDAC) generates desired current in 15 stages. Each output pulse generator is in a bipolar structure, which means there are 16 electrodes.

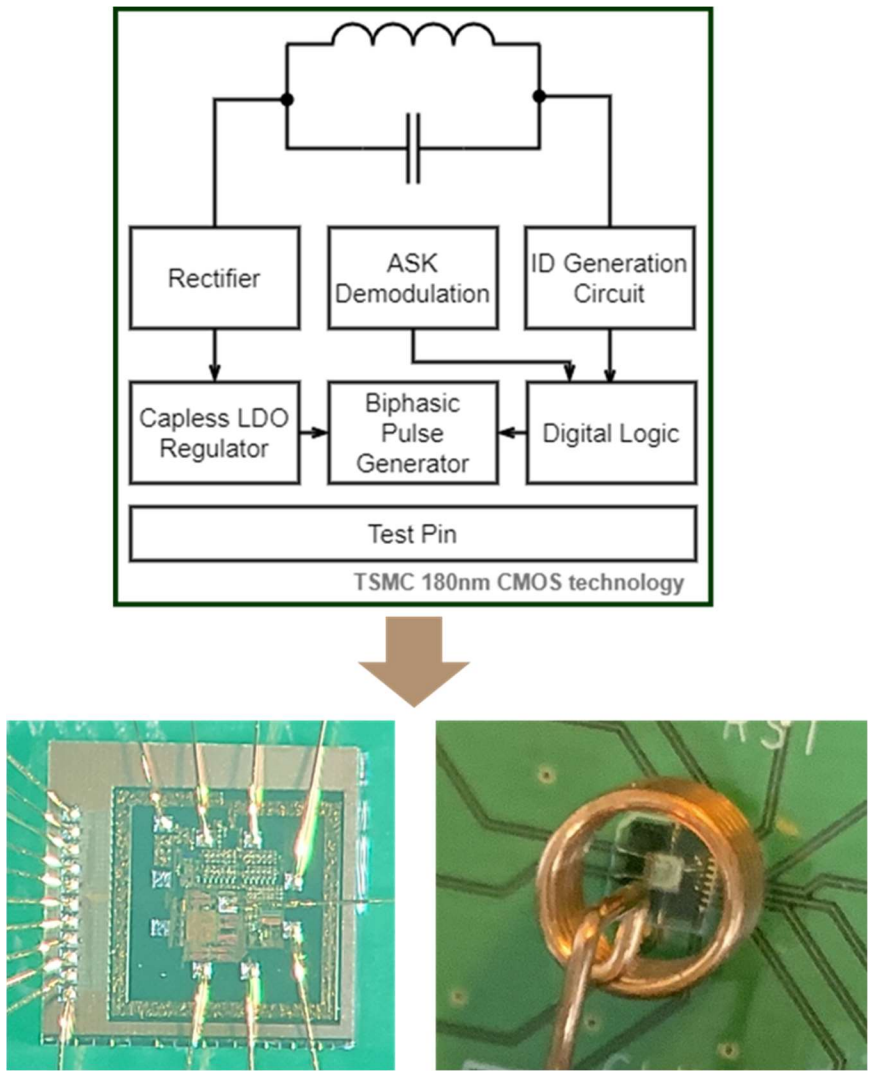

Figure 2. 4. Block diagram of designed stimulator circuit. Microphotograph of the fabricated IC and test bench setup with external coil

IC was wire bonded on the PCB, and the experiment was conducted by placing the transmission coil adjacent to each other (right). It exists as a single system with a 1 mm^2 area. The test pins are cut off after verification is complete.

2.2.1. Current Controlled Current Source

The iDAC as a current source is attractive for the lower space used by the MOSFET array and the ability to perform some calibration tricks. Most devices use the current steering DACs where the output current is multiplied or mirrored to the output stage. A current steering DAC substitutes the resistor of the resistive DAC architecture with a MOSFET and uses some form of current element to produce the result. Current steering DAC, as shown in Figure 2.5, is an ideal current source for their straightforward architecture and sophisticated current amount control.

Binary-weighted current steering DAC could control the amount of current flow with simple control commands than ordinary current DACs. Also, it produces an output current almost equivalent to the digital (binary) input by using binary-weighted MOSFETs in the current mirrored circuit.

Sharing the DAC of the current source reduces the design area and the current mismatch of each channel. The DAC, which controls the stimulation pulse amplitude, is biased by the voltage reference circuit. The number of bits that determine pulse amplitude sets the resolution of DAC. The linearity of the DAC is simulated with parallel input of a 4-bit counter.

Moreover, we used a 1 MHz clock to ensure the operation. After looking at the result of operating 10 times faster, we analyzed the operating performance at the original speed.

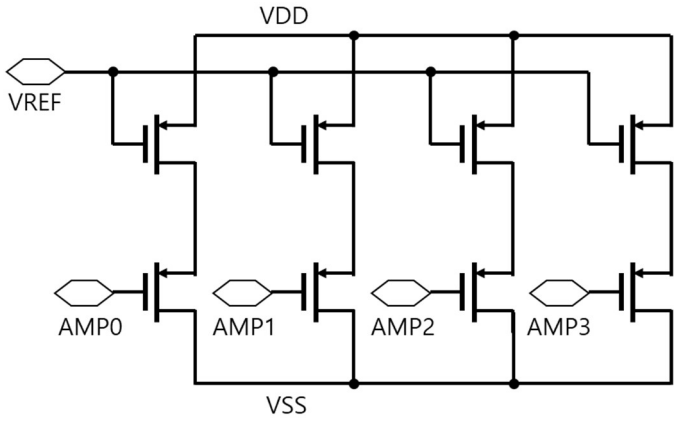

(a)

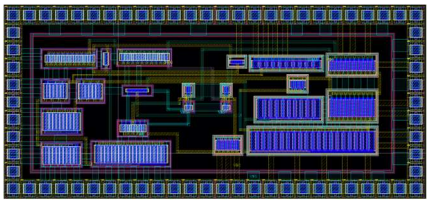

(b)

Figure 2. 5. Binary weighted current DAC (a) schematic of 4-bit DAC (b) current output stage layout

The number of bits that determine pulse amplitude sets the resolution of the DAC. When the digital input of AMP<4:0> increases, the current rises from 15 µA (LSB) to 225 µA. The layout of the current output stage utilized 140 µm x 40 µm area. Each bit contains information about the stimulation parameter. With a single fixed clock, 1800 different pulse shape is available. When the clock change, the range of the parameter also changes

2.2.2. High Impedance Output Stage for High-Density Stimulation

Although recent studies search for ways to send vivid visual information with a limited number of electrodes or pixels, increasing the spatial resolution of the artificial retina is necessary. Compliance voltage is the maximum voltage of the output stage that the current source could have for the desiring current. Compliance voltage values are user-settable, allowing complete control over the sourcing and measurement process. Current stimulation circuits calculate and simulate the compliance voltage of the output stage. High compliance voltage means the system could endure a larger impedance with the same stimulation current. Therefore, modifying the circuit source to sustain the variation load is preferred. Giving compliance voltage over 5-12 V by stacking MOSFET was shown to be made easily [56]–[58].

As shown in Figure 2.6, a biphasic pulse generator takes two forms: The current source-sink structure [59], [60] and the H-bridge structure [61]–[63]. Current source-sink structures are usually monopolar structures with biased electrodes. The bias voltage is generally half VDD or GND, depending on the floating voltage. Because of the bias, the output swing of the circuit gets up to half VDD. The advantage of using this architecture is that it could save design space by sharing the current source and having an output port on one side. On the other hand, H-bridge structures are favored for their full output swing and easy control of current flow.

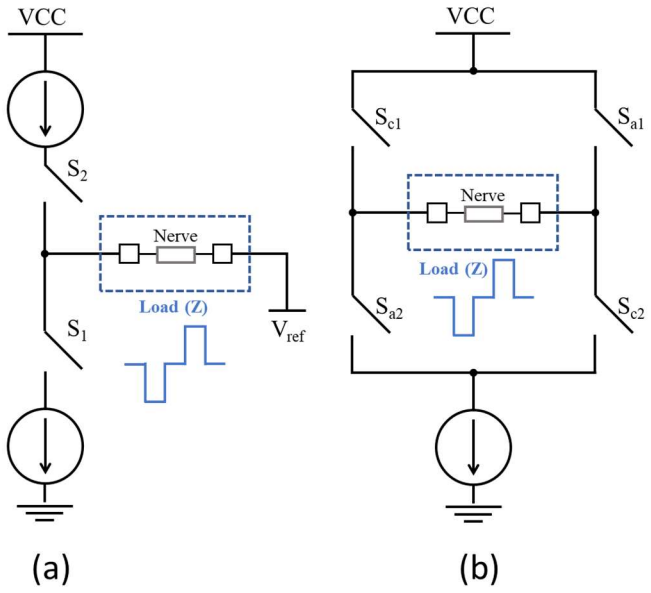

Figure 2. 6. Conventional biphasic pulse generator. (a) source-sink model (b) H-bridge model

Generally, H-bridge architecture is known to deliver biphasic pulse stably and suffer less from shape distortion and charge imbalance.

We tried to mix the two models to increase the output swing while having a small design area. The regulated cascode current mirror (RCCM) is the most preferred solution, which allows high output impedance while getting output swings similar to the simple current mirror [64]. RCCM in Figure 2.7 consist of PMOS (MP6, MP7, and MP8) and NMOS (MN1, MN2, and MN3), stably transferring the current received from the DAC to the electrode. The structure offers elaborate current control mirrored from MP11 and creates a biphasic pulse form by switching MP9 and MN4 on and off. MP5 and MN10 act as inverting amplifiers, lowering the circuit's output compliance voltage.

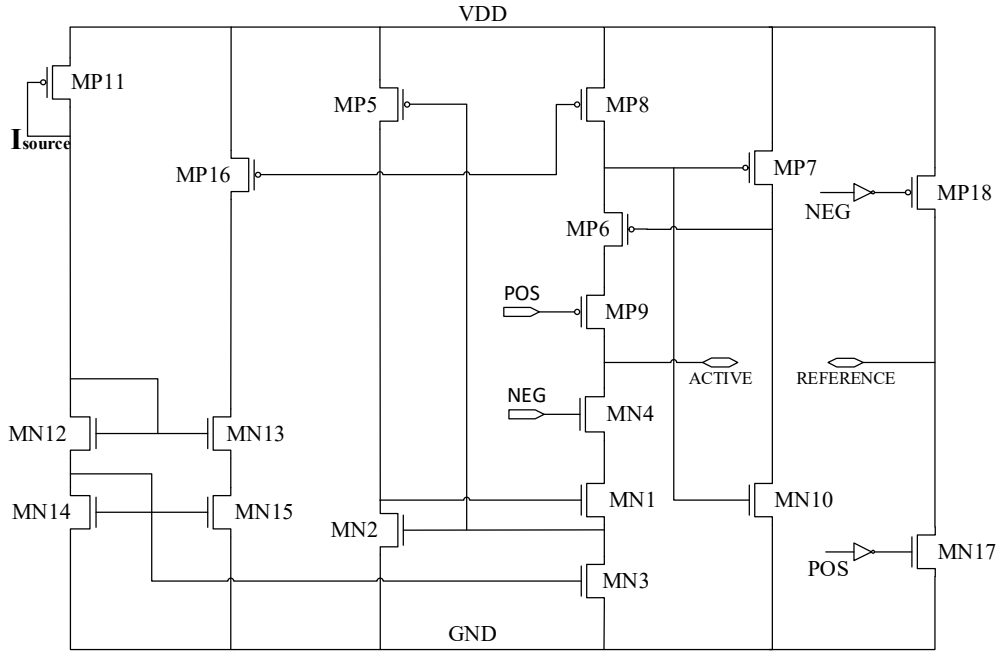

Figure 2. 7. Circuit model of bipolar electrode-tissue interface and modified biphasic pulse generator

2.2.3. Stimulation parameter and control

Different stimulation pulses could selectively activate each neuron for a retinal prosthesis as various retinal cells are integrated. Pulse width, amplitude, frequency, period, and shape are the stimulus parameters that determine the amount of charge and exposed time. Table IV shows the details of the stimulation parameter for square shaped electrical pulse stimulator. Considering the environment around the electrode exposed to the electrolyte, the frequency components of the stimulation are filtered by the capacitance and resistance present at the electrode-tissue interface. Therefore, estimating the actual charge delivered to the target is needed after deciding the pulse amplitude, which controls the area range of the propagation. For instance, in a square-shaped pulse, the edges are rounded and distorted, decreasing the delivered charge by an average of 10%.

Table IV Stimulation pulse parameters of square pulse stimulator

Parameters	Value
Type	CC/CV[1]
Shape	Monophasic / Biphasic
Amplitude	0 – 300 μA
Pulse width	50 – 2 ms
Pulse rate	5 – 200 Hz, 1 kHz
Phase	Cathodic-, Anodic-
Interphase delay	0, 20, 40, 60, 80, 100%

[1] Constant Current (CC) and Constant Voltage (CV)

The operation mechanism of the stimulator is configured with a state

machine and counter. The serial command to the digital controller contains the stimulus shape information, which forms a lookup table. All stimulation parameters are controllable in our design by employing a universal clock. As the universal clock from the clock and data recovery (CDR) circuit become a reference to LSB in each parameter, each variable comes into existence in a specific combination. Therefore, adjusting each variable's range increased the number of sets generated.

The stimulator has two modes for the bidirectional neural interface: ON-OFF and real-time. In ON-OFF mode, after receiving the command and completing the manipulation of the stimulation variables, the set stimulation pulse is sent out as soon as the start signal comes. This method is suitable because it is immediate and can reduce the power consumption of the digital stage. Also, it is helpful when the stimulation parameters are optimized because it could give feedback stimulation while changing only the channel. The real-time mode processes the serial command and switches the parameters instantly. This method has an advantage in that the stimulation channel and the pulse shape are changed and sent out every moment, unlike the previous method, which requires delivering the same stimulation pulse fixed at the minimum threshold value. Although the power consumption is high, it provides stimulation feedback similar to a relatively actual nerve signal.

2.3. Results

2.3.1. Benchtop results

The circuit is designed in TSMC 180 nm mixed RFCMOS technology using 1.8 V/3.3 V standard cells. A prototype of the 8-channel stimulator was incorporated into a custom PCB for design validation. Figure 2.8. (a) show the microphotograph of the fabricated prototype. Including the pad ring around the ASIC occupied under 1 mm^2. In Figure 2.8. (b), the graph shows the measurement of the stimulation output in response to the serial command to the IC. The biphasic current pulse burst was measured while the 'ON' signal was high. Otherwise, no biphasic current pulse was measured. The most striking feature of the result is that a charge-balanced biphasic current pulse was output without being affected by load fluctuations. It could withstand changes in electrode impedance up to 10 kΩ on each side. As illustrated in Figure 2.8. (c), the total charge of the positive and negative waveforms had an error of only a few tens of pA. It can be seen from this figure that the charge imbalance decreased in the PBS solution than with the load resistor. Figure 2.8. (d). demonstrates the pulse frequency modulation result from digital logic analyzing the output pulse of the stimulator.

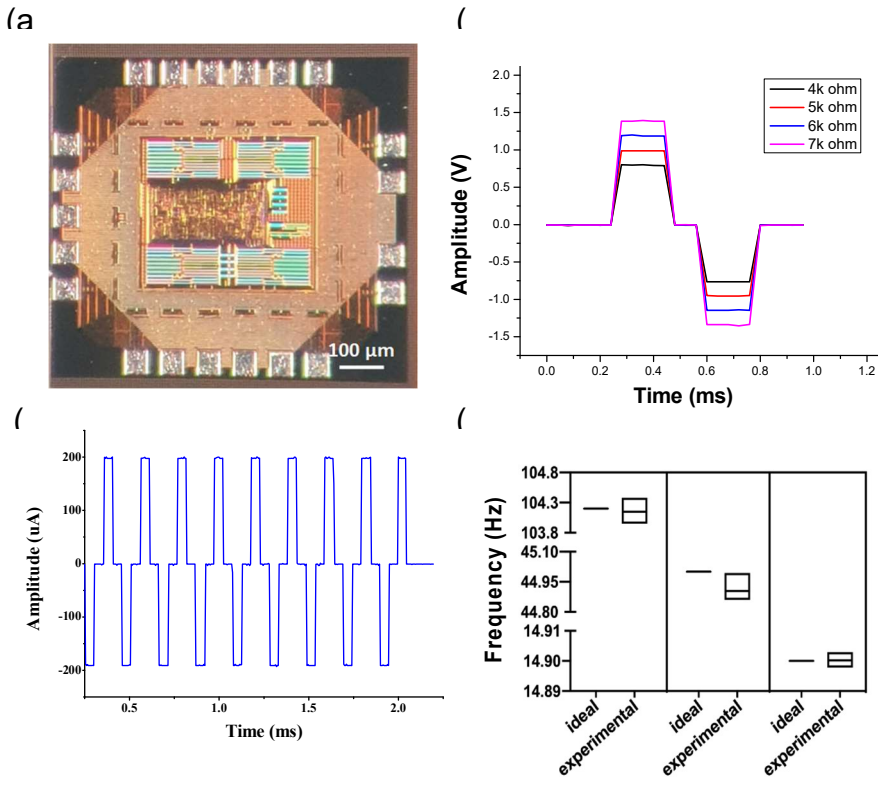

Figure 2. 8. (a) Microphotograph of the fabricated IC (prototype) (b) constant current pulse with load impedance variation (c) measured biphasic current pulse in PBS solution (d) pulse parameter modulation result and error range

The prototype possessed the 8-channel biphasic current stimulator and was used in patch clamp experiments with WT mouse retina.

2.3.2. Ex vivo experiments with mouse retina.

The preparation of retinal tissue was as follows, as shown in Figure 2.9. C57BL/6NHsd 12-week-old rat eye retina tissues were obtained and fixed on filter paper. Immerse the prepared retina in a bath where Ringer's medium flows and remove it by pushing the inner limiting membrane covering the ganglion cells under the microscope with a glass pipette. Whole-cell patch measurement is attempted on exposed ganglion cells, and at this time, intracellular current stimulation or extracellular current and light stimulation is applied. When stimulating the extracellular tissue, a rectangular biphasic pulse was given at a point several tens of microns away from the ganglion cell to be measured with the Pt/Ir concentric microelectrode.

We used wild-type (WT) mouse retina to extract the stimulation parameter of retinal ganglion cells with a programmable biphasic stimulator [64]. Whole-cell current patch clamping recorded the target cell's spike activity. The distance between the stimulation electrode and patch clamp recording electrode is depicted in Figure 2.9. The 3-dimensional distance from the target cell did not exceed 60 μm. Figure 2.10 shows the location of each electrode and the appearance of the observation microscope.

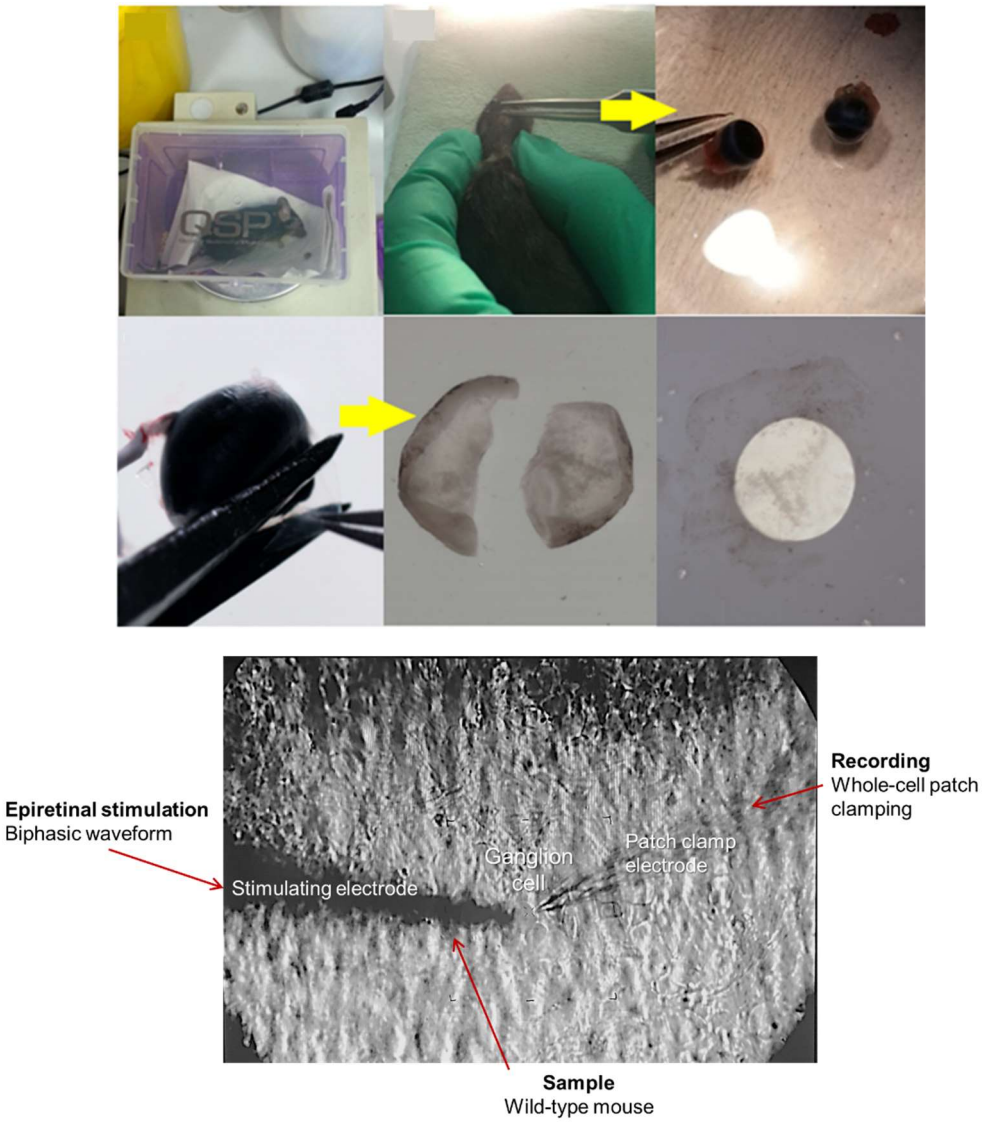

Figure 2. 9. *Ex vivo* experimental setup and tissue preparation.

Both eyeballs were excised. The retinal tissue was torn out and used, and the tissue was widely spread and fixed using paper support so that the tissue was not shaken.

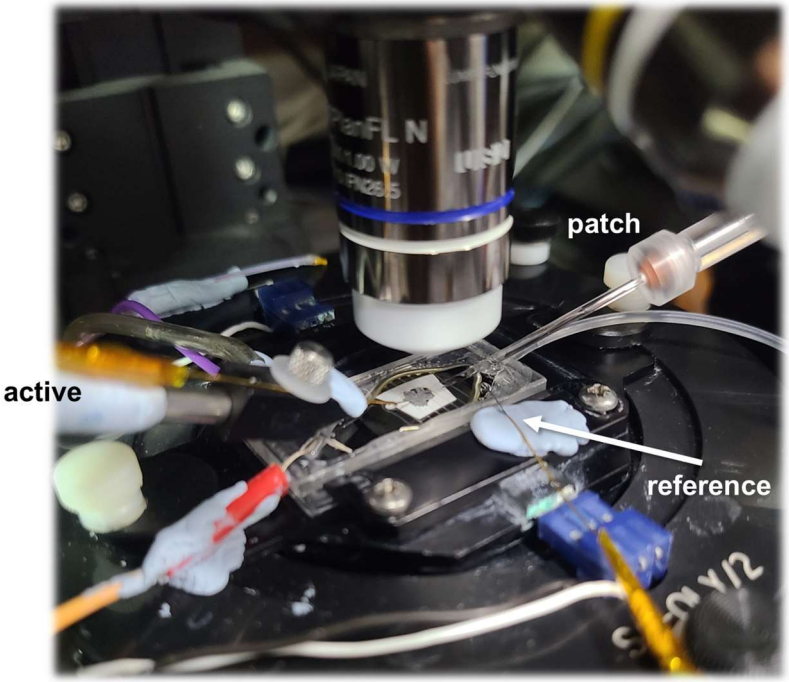

Figure 2. 10. Experimental setup. The stimulator test board is placed near the active electrode. The patch clamp recording electrode is placed on the right side of the microscope

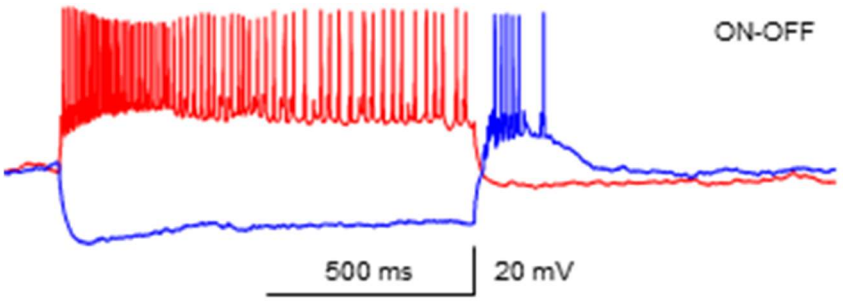

Figure 2. 11. patch clamp recorded the response of ON-OFF cell with light stimuli

The stimulation response from light input was first analyzed to regenerate a similar response with electrical stimuli. With the experimental setup, as shown in Figure 2.11, the retina tissue is placed under the perforated paper supports. As previously mentioned, the ON-OFF cells presented a different response to the same light stimulation. Therefore, we used the prototype to mimic the response by modulating the pulse parameters.

As seen from Figure 2.12 graph, the spike firing rate of a single stimulation pulse depends on the pulse width and percent of the interphase delay relative to the first phase. The correlation between spike activity and current amplitude has a notable feature in Figure 2.13. The spike frequency varies in the form of concentric circles with a 5 Hz and 120 μA two-phase pulse in the center. Saturated areas could not be recorded due to the recording amplifier, but assuming the site is less active, it would appear light blue. The average data indicated that the optimal distance is under 60 μm. It would keep the tissue untouched while delivering the stimulation charge with a fair amount of loss.

Cathodic first biphasic pulse has shown much more spike counts compared to anodic. The interphase delay, which was 50-60% of the pulse width, has shown the most spike count in every trial. When high-frequency stimulation pulses were applied, OFF cells responded at lower stimulation currents around 80 μA.

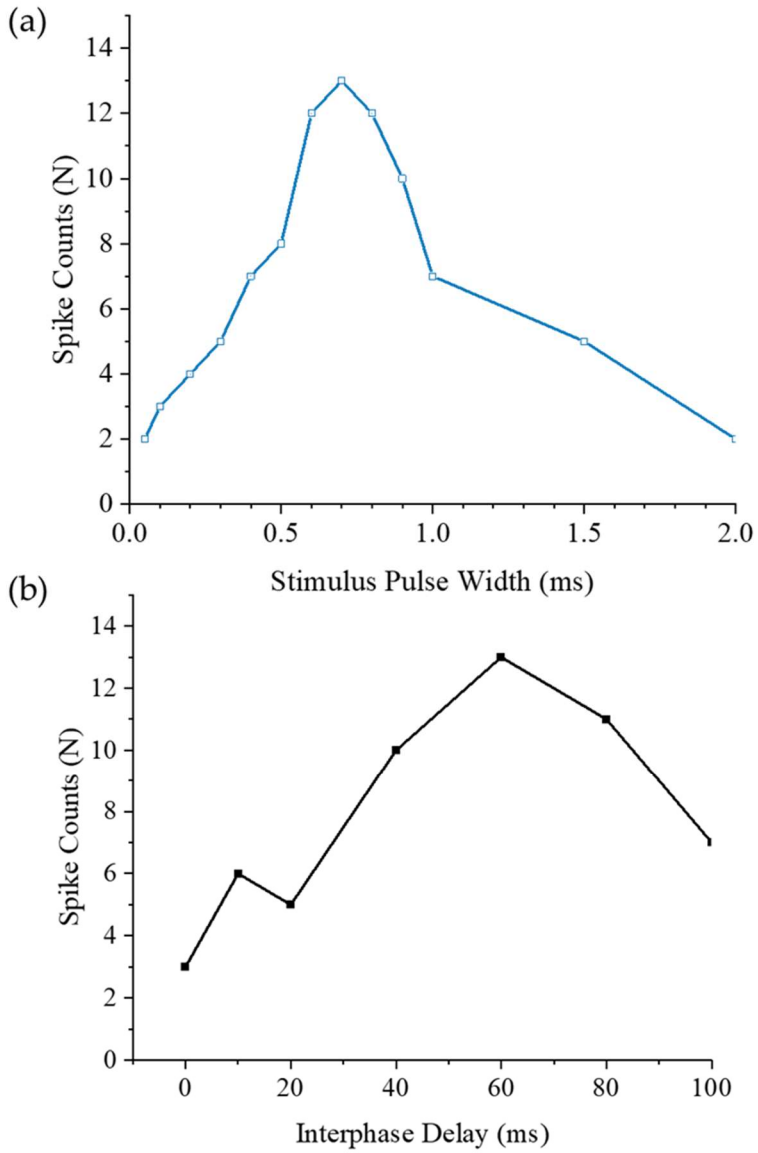

Figure 2. 12. Spike firing rate. Corresponding to the (a) pulse width and (b) interphase delay

The pulse width of the stimulus apparently and consistently has shown that over 1ms only accumulated charge but did not elicit a meaningful stimulus-response.

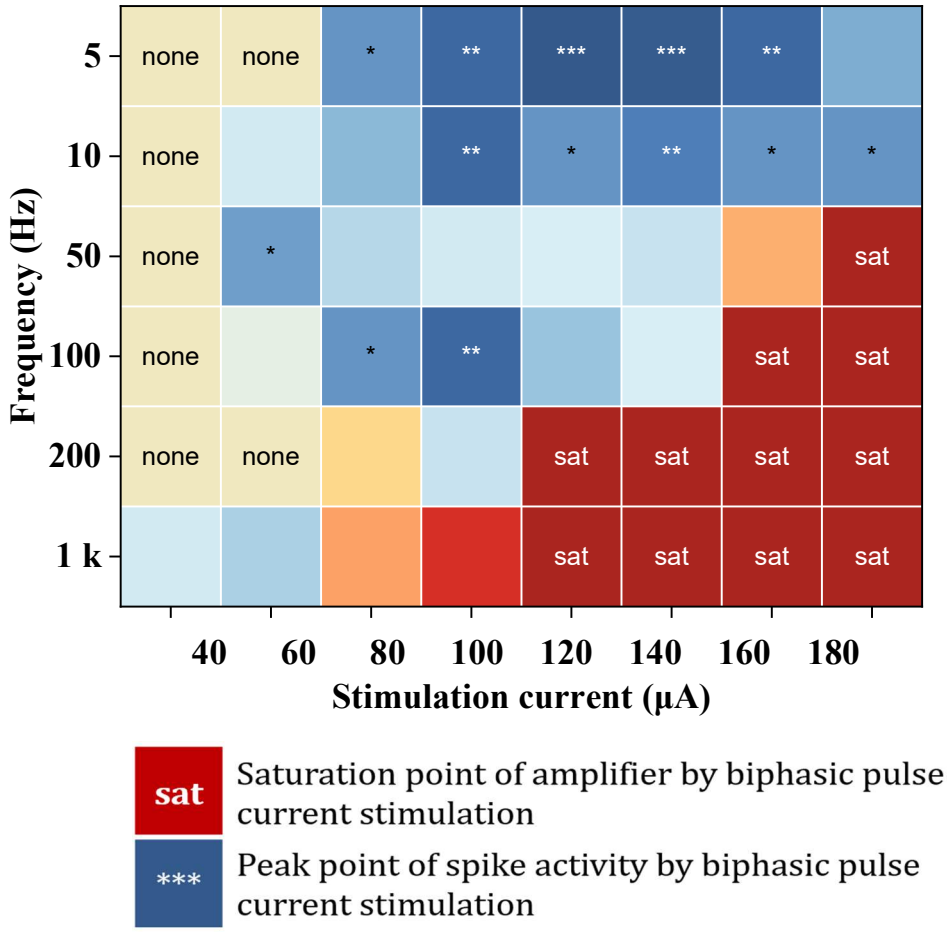

Figure 2. 13. Correlation between stimulation pulse amplitude and frequency

The red color indicates that the stimulus-response decreases. In particular, the saturation area shows both cases where it is difficult to observe the response because the stimulation pulse is too dominant and cases where the recorder amplifier is saturated. The change in the frequency of spike occurrence in the form of a concentric circle shows that the variable's value is optimized for extracellular stimulation at an electrode 60 µm away.

Electrical stimulation elicits a neural response by opening the voltage-sensitive ion channels and bypassing the chemically gated channels in the stimulated cell. To investigate the threshold of electrically induced responses of RGCs in rd1 mice, we tested 160 pulse sets consisting of 5 frequencies, 4 pulse widths, 4 amplitudes, and 2 phases. Results indicate similar responses to the same range of stimulation parameters. The frequency range and pulse width remained the same, but the amplitude had to be higher to evoke a stimulus-response. Also, even if the amount of charge applied at one time is the same, the higher the amplitude, the higher the frequency of action potentials and the more constant. The distance between the electrode and the cell was maintained at 60 μm in the XY axis to compare the amount of charge accurately reached. One more clearly visible part in the shape of the stimulation pulse was that the number of action potentials was higher when the cathodic pulse was applied first, which was more prominent in the rd1 mouse. The graph in Figure 2.14 is the most commonly observed result among stimulus responses. The burst of action potential continued when one stimulus pulse was applied, and the number of action potentials generated decreased as time passed from one stimulus pulse to the next. After the first stimulus-induced action potential was observed, almost no action potential was seen when it approached 600 ms after the stimulus started. Also, a state of no response for 1 to 1.5 seconds was repeatedly observed.

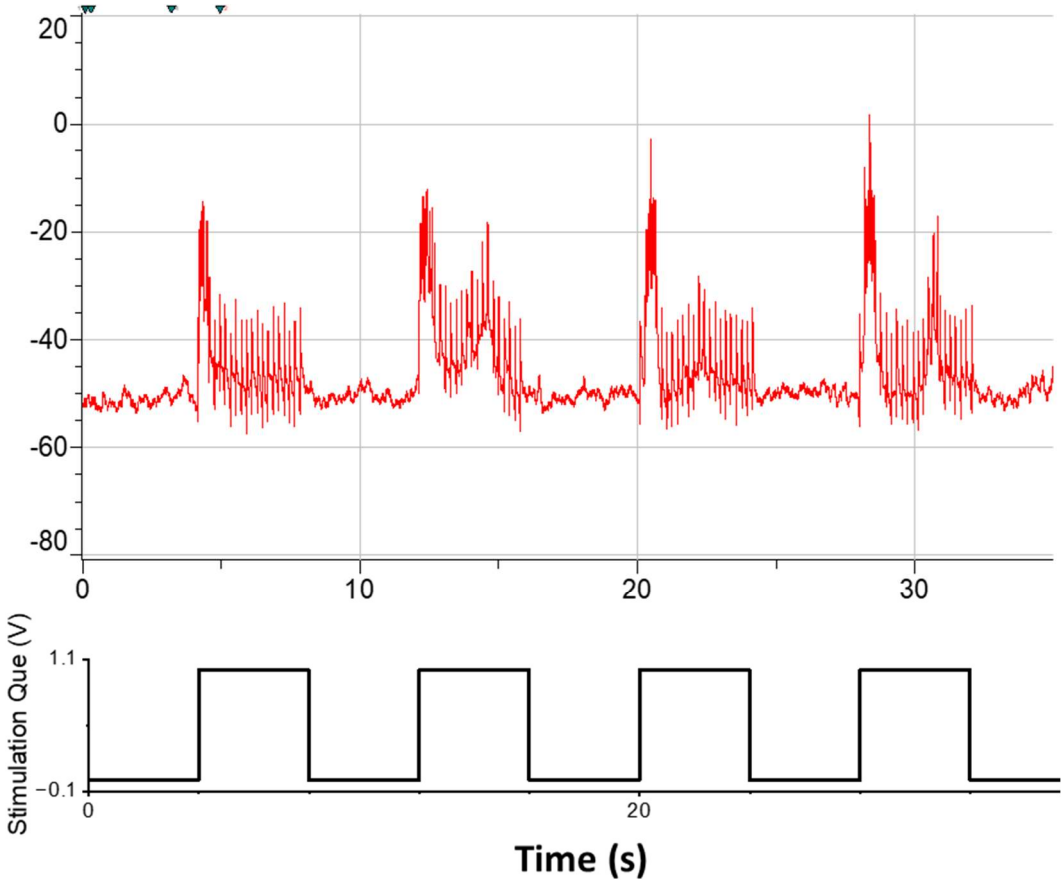

Figure 2. 14. Retinal stimulation result of rd1 mouse retina

The rd1 mouse retina was stimulated with an optimized microstimulator. The stimulation parameter that induced action potential was identical to the method used for WT mouse retina stimulation, except the amplitude was slightly increased.

2.4. Summary

After the retinal degeneration caused by retinitis pigmentosa or age-related macular degeneration, the retina loses the ability to sense light signals at photoreceptors. Although partial layers of the retina, usually retinal ganglion cells remain. We are trying to restore visual perception through electrical stimulation.

Physical and methodological difficulties lag high-density stimulation. Since the eyeball is spherical, as shown here, it is necessary to create a system that considers curvature. Statistically, with the same material, the open surface and structure of the electrode correlate with impedance. Also, the impediment that causes higher resistance is at the electrode and electrolyte interface. The number of electrodes per area increases resolution, and various visual information, such as contrast, should be delivered [65], [66]. First, looking at previous research records and FDA-approved devices, the shape can be recognized if at least 1000 channels are guaranteed. There are attempts to increase the spatiotemporal resolution, but according to research results, different optic nerve cells must consistently transmit various nerve signals to perceive vivid visual information in our heads stably. Various programmable stimulators were proposed based on the theory that the signal diversity of complex neural networks should be simulated rather than simply forming neural signals.

Here, we designed a multichannel microstimulator as a prototype to investigate selective stimulation with low power consumption. Experiments

were conducted using WT rat retinas, and a minimum threshold was found to enable selective stimulation. There was a common variable range, but in the case of ON-OFF cells, there was a difference in response in the phase difference and stimulation frequency. When high-frequency stimulation pulses were applied, OFF cells responded at lower stimulation currents around 80 μA. Next, this device experimented on the retina of the rd1 rat again. One thing we are researching further is that when the stimulation pulse is applied for more than 600 ms, the AP no longer comes out, and it can be seen that it bursts again after at least 2 seconds.

Chapter 3. Multichannel Stimulator for Bidirectional Neural Interface

3.1. Introduction

The bidirectional neural interface system for the brain-machine interface is a well-known neurotechnology in medical and research areas. Since Professor Jacques Vidal of the University of California at Los Angeles coined the term 'Brain-Computer Interface (BCI)' in 1973, broad research about implantable system design, neural data analysis, and stimulation feedback has thrived. BCI, also known as a brain-machine interface (BMI), was initially developed to help patients with severe motor disabilities who could not communicate. A significant number of publications related to new benefits for potential users of BMIs are made annually. For instance, studies reported helping stroke patients regain movement [67], [68] or helping neurosurgeons map the brain more accurately to perform surgery more quickly and safely [69], [70]. The miniaturization of the brain interface device and the diversification of networking technology are due to the remarkable development of semiconductor processing technology and wireless communication technology [71]. In particular, the fully implantable brain interface device, which can be inserted entirely into the body, eliminates the threat of infection and discomfort from an aesthetic point of view, enabling multidisciplinary research and

therapeutic use.

The most challenging part of utilizing a bidirectional brain-machine interface is to analyze the detected neural signal and give accurate stimulation output in real-time. Load to the real-time processor varies with their target neural signal band. As seen in Figure 3.1, the different spatial resolutions of neural signals are recorded according to the placement of electrodes. According to the signal band, the amount of data and sampling rate needed for signal reconstruction alters. Compared to electroencephalography (EEG), which has a range of 250-1000 Hz for sampling frequency, electrocorticography (ECoG) has a sampling frequency ranging from 1000-2000 Hz for neurological data collection. A sampling rate of 1000 Hz or higher can be an excellent option to offer an adequate resolution in the time domain to study and monitor neural activity.

Many brain-machine interface technologies are based on noninvasive methods. The normalized complex brain wave potential lowers the resolution of the signal, is very susceptible to noise, and the accuracy of local brain activity analysis is reduced due to the brain wave's diffraction, spread, and attenuation. However, the spatial resolution and quality of signals when using ECoG are better, despite using an invasive method. Since signals are measured through electrodes on the brain's surface, it is helpful because it can obtain signals without damaging the brain. In addition, an invasive method has the highest accuracy for transmitting intended stimulation to the target cortex area regarding feedback. Micro-Electrocorticography (μECoG) is a minimally invasive intra-cortex neurological signal monitoring technique that records

electrical potentials and gives stimulation employing microelectrode arrays placed on the surface of the cerebral cortex under the scalp.

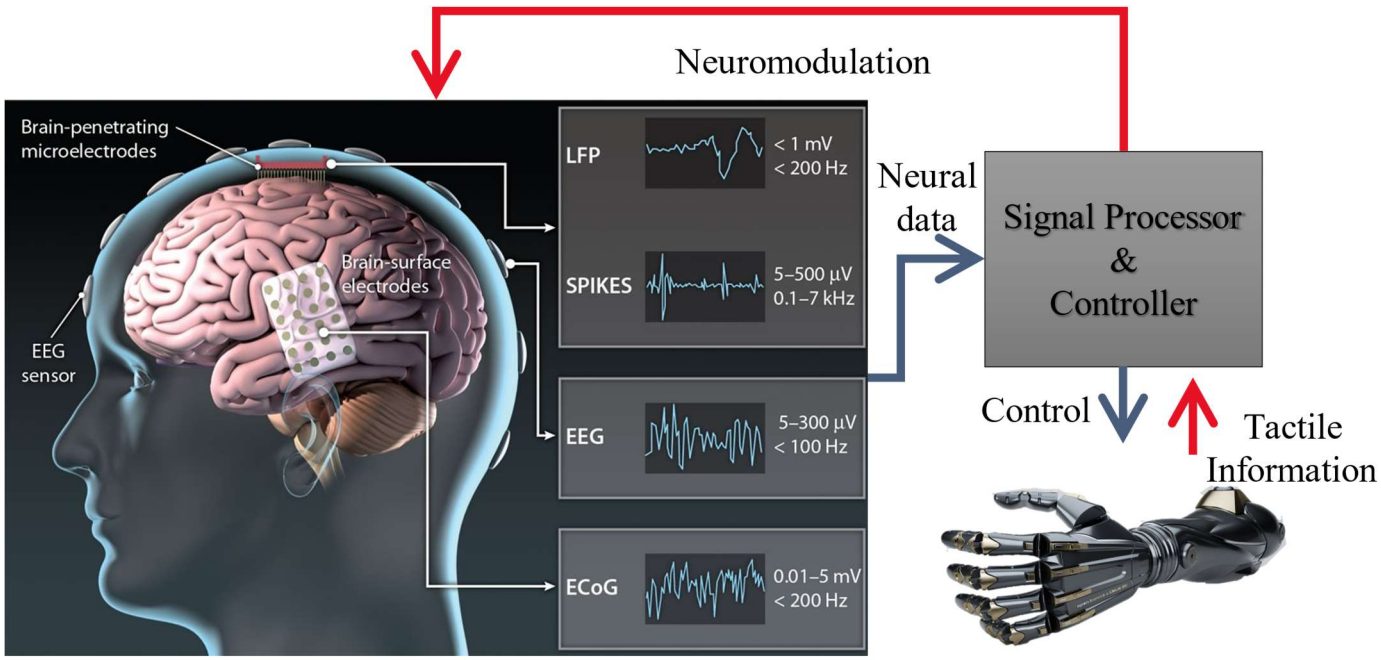

Figure 3. 1. Overall concept of BMI and type of brain signal according to the placement of the electrode [72]

As a part of BMIs, neural recording units capture brain signals, amplify, digitize them, and transmit them outside the body through a wireless transmitter [73]. In addition, attempts to artificially interfere with neural networks from the outside by applying stimuli have been reported, going further from studies that record and analyze existing neural signals to control external devices. Among various stimulation strategies, such as transcranial magnetic stimulation [74], [75] or optogenetics [76]–[78], neural modulation through current stimulation is an effective means to give a wanted signal as an input to a neural network [79]–[81]. In the case of going beyond the animal experiment stage and going to human clinical trials, electromagnetic methods are often used for both recording and stimulation.

The purpose and effect of neuromodulation on BMI have been reported in recent decades. Some focused on functional electrical stimulation to rehabilitate damaged or lost brain function [82]–[85]. On the other hand, some studies reported that BMI that evokes tactile sensations improves robotic arm control using electrical stimulation as a feedback form of BMI [86]–[89]. The research team at Pittsburg university reported a bidirectional brain-computer interface generating tactile percepts for people with tetraplegia. The system records neural activity from the motor cortex and generates tactile sensations through intracortical microstimulation of the somatosensory cortex [90].

Given the neural signal recording as part of the BMI system, sensory feedback through neuronal stimulation enhances the overall efficiency and control accuracy. Based on the facts, appropriate stimulation of the postcentral

gyrus, found in the parietal lobe, can make tactile senses artificial [91]. The tactile data, such as pressure and tension, would let the user control the machine more precisely. Several BMI systems with stimulation feedback are developed for the wireless implant and tested its functionality [71]–[73].

Furthermore, the wireless input and output data transmission system, data transmitting in and out of the human brain, is essential for building the connection between the human brain and others. Since it is big data, real-time signal acquisition and signal processing and giving feedback to the brain again need a reliable and robust data stream. A micro-sized device implanted on the brain surface collects each of their signals and transmits them to the receiver outside the human body. Given the environment of the human body, radiation and heat are critical concerns.

However, the current implantable BMI system has an unacceptable noise level and requires much power consumption to be implanted. The need for appropriate approaches to design a BMI circuit system gradually increased. Ultralow power consumption is pursued so that the results of this study would be used for preclinical and clinical applications with a wireless power transfer system.

3.2. Circuit Description

In this chapter, a fully implantable multichannel BMI system has been presented. 128-channel recording module and 32-channel stimulation module are integrated into a single chip with 180 nm RF general process occupying around 22 mm^2 areas. As the proposed design has both digital and analog circuits, the design flow follows the procedure of mixed circuit design. Our design flow is featured in Figure 3.2 according to each design step. Five tools are used in total, though the HFSS antenna simulation tool is not mentioned. The core parts of the recording and stimulating module are simulated in cadence virtuoso spectre. It is then integrated with digital logic, designed in Synopsys tools. First, Verilog scripts are simulated with ModelSim from Mentor. For high-speed clock modules connected to RF circuits are revised with VCS. Synthesis with the design compiler is repeated several times with its constraints. After the formality check, IC-compiler Ⅱ places and routes to draw the layout of the digital circuit. Pads are unnecessary for the current design, such that the GDS file from IC-Compiler Ⅱ only makes input pins. Import the GDS file to the virtuoso spectre and Verilog code file for AMS simulation and post-simulation with analog circuit design. AMS simulation and pre-simulation are compared and revised for mixed integrated layout simulation. Using HFSS and a network analyzer, impedance matching between the antenna and rectifier is applied.

Analog circuit design aims to separate the interference and environmental noise from the connected power supply while maintaining low power. The

ground line isolation is conducted with a power cut similar to ferrite beads. Four regulators supplied power to digital and analog circuits in 1.2 V and 3.3 V for isolation and stable performance, respectively. As the recording unit operated at 1.2 V and the stimulator operated at 3.3 V, separation was easily achieved.

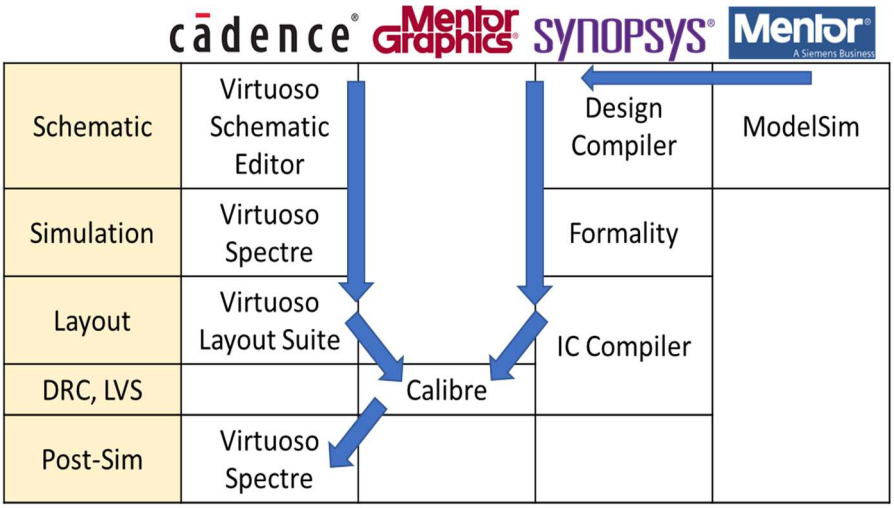

Figure 3. 2. Design flow of ASIC simulation and backend process

Figure 3.3 illustrate the post-implant placement of the proposed system. Since the system connected to the implanted electrode is thin, the skull is slightly dug out, and the system is placed. The power reception and data transfer antenna is to be placed above the skull and the skin tissue for efficiency. The Block diagram of the system in Figure 3.4 describes IC and passive components integrated into PCB. The system consists of an IC with the main functions of recording and stimulation integrated and an external transceiver communicating with the signal processor on the computer. The core IC has several parts, which are 128-channel recording modules, 32 channel stimulation module, a power management module, and a bidirectional communication module using backscatter communication and DPSK modulation with 16 MHz carrier frequency.

The recording modules capture brain signals and amplify and digitize them to transfer outside the body with a transmitter. This unit's primary concern is minimizing power consumption and the silicon area, maintaining overall performance. For the module to achieve high SNR at the output of the neural amplifier with noise reduction technology, we designed a low-noise amplifier with an appropriate gain considering artifacts and quantized it using a time division technique. Also, they are digitized with an analog-to-digital converter (ADC) to transmit neural signals outside the body.

The programmable controller in the stimulation modules decodes the serial input data and modulates the stimulation pulse parameters. The state machine and counter decide the degree of freedom in modulation in the digital logic. The control command from the digital logic turns on-off the analog

switches in biphasic pulse generators. DAC-sharing architecture saved area and power. Current mismatch through the current mirror is addressed with a common source (CS) feedback circuit at the output stage.

The real-time brain-machine interface is designed to convert binary data into original neural signals and find meaningful data from each channel. External board with duplexer filters out unnecessary signals received from the antenna, and digitizes it. The MATLAB-based signal processor analyzes the neural data and gives stimulation commands corresponding to the queue.

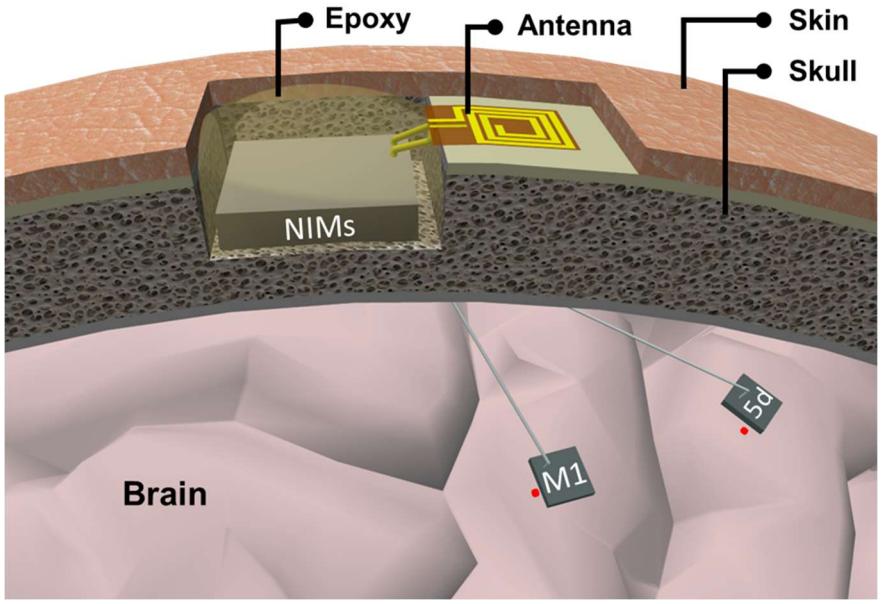

Figure 3. 3. Illustration of system placement and the electrode

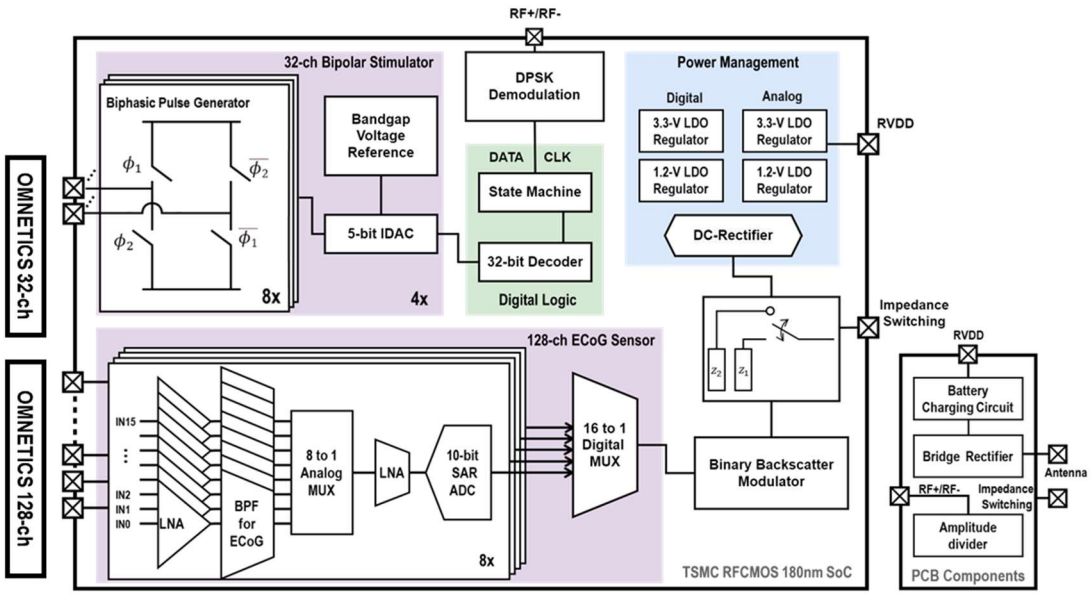

Figure 3. 4. Block diagram of the overall neural interface system

3.2.1. Current DAC and Biphasic Pulse Generator

The biphasic current pulse is preferred for preventing excess charge accumulation over time, which causes tissue destruction and electrolysis with electrode dissolution. Moreover, as the stimulation architecture affects the reaction of the tissue and stimulation efficiency, a bipolar structure is chosen to produce more focused and selective stimulation.

Since the size of the whole system is a considerably big issue, 5-bit iDAC is designed to control the amplitude of the output current pulse. As we tried to control the parameter manually with the input data from outside, the LSB of pulse width and period is based on the system clock, which is 1 MHz, counting until the assigned value. With an LSB of 10 μA, MSB is 310 μA which is thought to be optimal for stimulating the target cells.

Figure 3.5 is the schematic of the stimulator analog backend. The startup and voltage reference circuits generate reference current after the supply voltage gets 1.67 V. From the simulation, piece-wise linear (PWL) voltage input (0-3.3 V) to the VDD has verified the PSRR of the system. The bandgap voltage reference circuit works as a calibration circuit for the voltage reference circuit.

As a stimulation module, the system gives a large output current to the electrode-tissue interface, which is usually high impedance. A high output swing is needed to sustain high compliance voltage while maintaining high output impedance. A modified low voltage regulated cascade structure is used at the output current mirror of the biphasic current source. As an advantage, low output compliance voltage offers high output impedance and consumes around 40 μW of power.

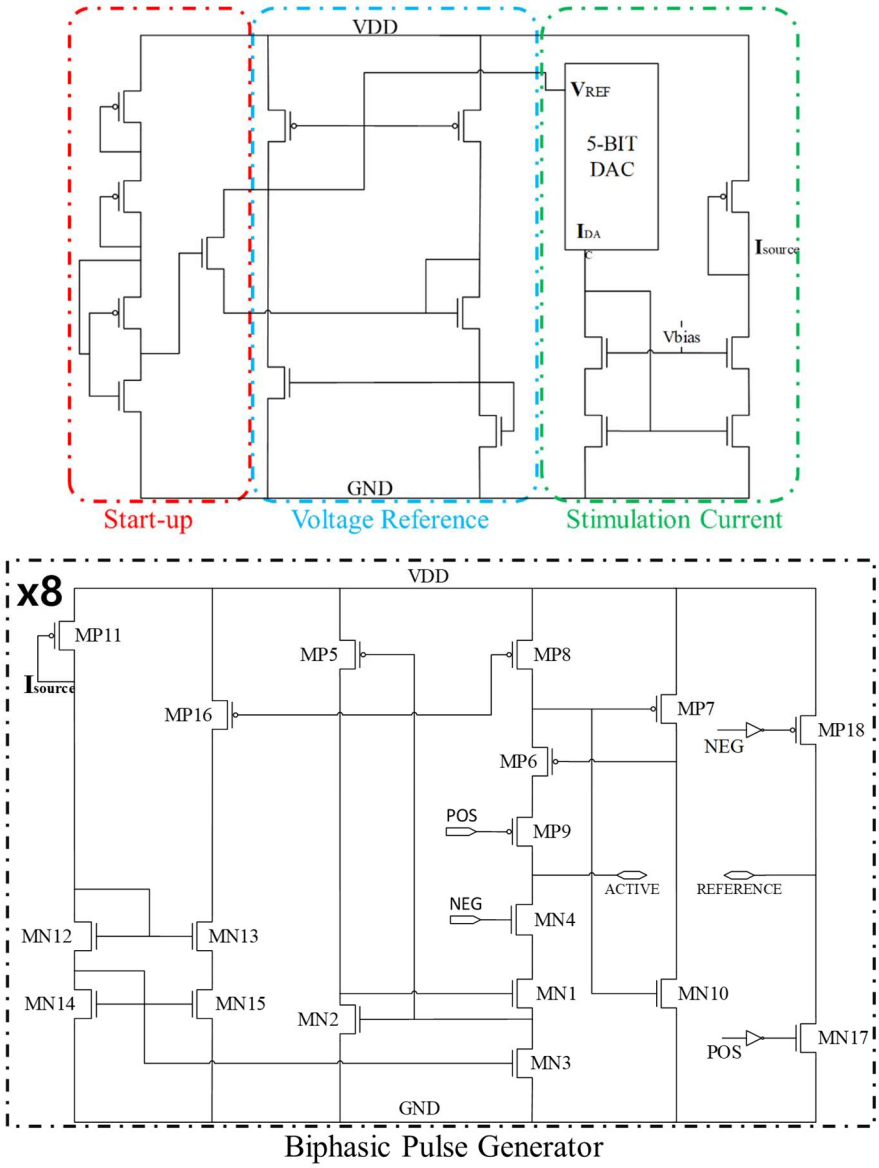

Figure 3. 5. Circuit diagram of stimulator analog frontend

3.2.2. Digital Logic

Digital logic is the core part of a programmable stimulator. Low power consumption and scaling down the system are mainly done by optimizing the digital circuit. The structure of the Verilog code mostly determines the power consumption and area. Through several simulations, we conclude that the case statement uses less power and design area than switch and if/else if statements. The layout of the digital circuit occupying an area of 0.16 mm^2

Stimulation impulses are designed based on divided bits and counters. Serial bits with the synchronized clock signal and reset are the essential three components of Digital logic. The state machine and multi-bit counter are the fundamental algorithms that decode the stimulation command. Figure 3.6 (a) shows the binary bit information of the serial input, and (b) is the timetable of the digital logic.

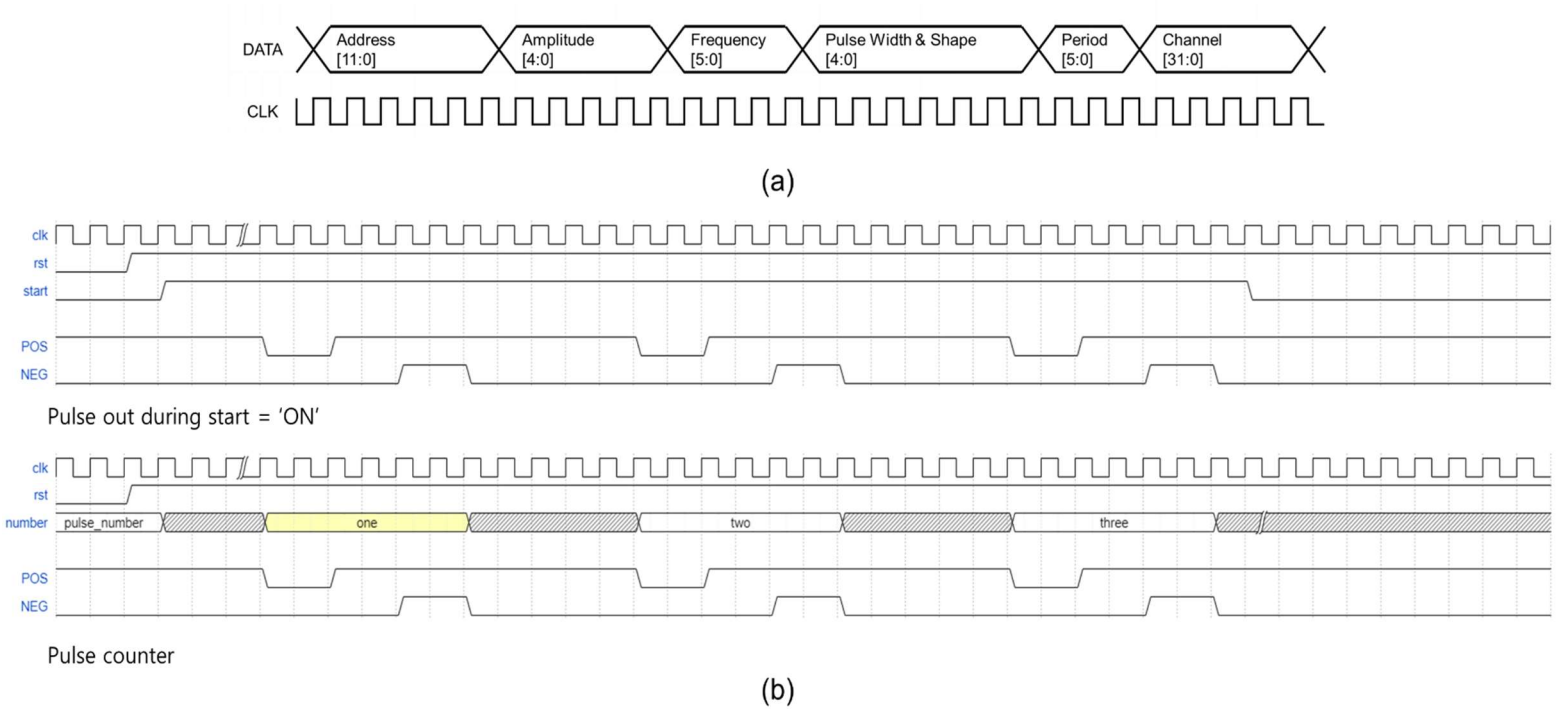

Figure 3. 6. Digital logic command information (a) Serial data bit information that is synchronized with the clock signal (b) Timetable of pulse generation and counting

3.2.3. Bidirectional Communication

In bidirectional communication, reducing the interference between two communication methods is a critical concern influencing data transmission efficiency. The transceiver's design condition, especially with single coil communication, affects whether it chooses to use the different modulations among amplitude, phase, and frequency. The key design considerations are power, area limit, or carrier frequency range. Low power consumption and a small design area are strictly maintained because the system is designed for an implant. Given the above conditions, we chose phase shift keying (PSK) demodulation, which uses noncoherent detection to avoid using PLLs. Furthermore, the proposed scheme can demodulate the data signal with power interference without additional circuits.

Noncoherent detectors are widely used in RF applications despite their higher bit error rates since they can be implanted much more simpler than coherent ones with lower power consumption. Noncoherent detection uses subsampling for data demodulation [92]. There are two ways to implement subsampling. One is to digitize the carrier signal before sampling, which is sensitive to jitter when sampling occurs on the transition edge of the digitized carrier signal [93]. Another approach is to sample the analog signal and process it in the digital domain to avoid rapid amplitude changes in the sampled signal. When sampling at the zero crossing of the signal carrier, the sampling jitter presents much less error than its digital counterpart. However, the latter approach requires analog-to-digital converters (ADCs) that consume more power for implantable devices with high data rates. Our approach solves the

problem by designing a 1-bit ADC in low supply voltage, sampling the analog signal, and processing it in the digital domain.

The noncoherent differential phase shift keying (DPSK) demodulation scheme is converted to circuit design mainly using digitization and binary bit operations. All the circuits for data demodulation are designed with a fully differential topology for charge injection cancellation and power supply rejection. This method uses the phase of the RF signal, which has the advantage of a low bit error rate in a poor communication environment. A constant amplitude carrier signal provides stable power transfer at high efficiency. Also, the constant carrier frequency allows for the use of fixed-size antennas, which can be designed for optimal data and power coupling. The circuit operates under a 1.2 V supply voltage, and total power consumption is 46 μW

As shown in Figure 3.7, DPSK (Differential Phase Shift Keying) in binary bit is used for data demodulation. The demodulation circuit comprises a differential clipper, 1-bit ADC, comparator, half-duration delay circuit, and gate operators. The serial data is decoded by comparing the former 1-bit with the current 1-bit data through the XOR gate. When the current data is different from the former, the value is "1"; on the other, the value is "0".

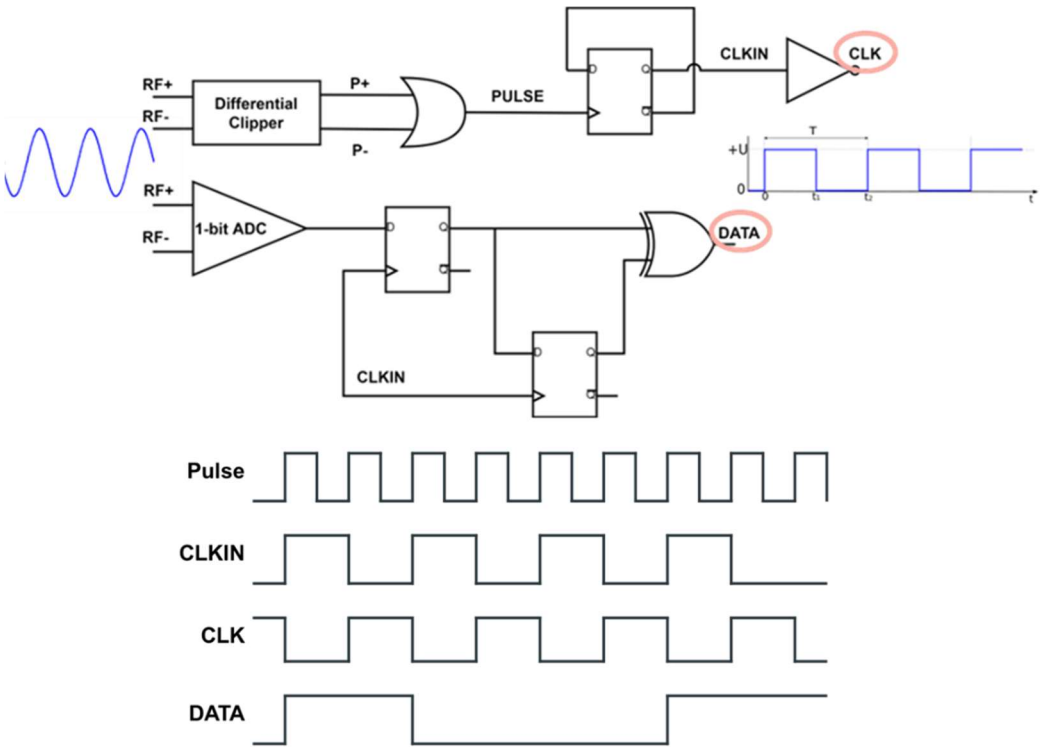

Figure 3. 7. Clock & Data Recovery of downlink communication. Data demodulation circuit and its timetable

Differential clipper and 1-bit ADC digitize the sinusoidal signal to binary serial bit. Figure 3.8 and Figure 3.9 shows the signal processing of the clock and data recovery circuit. When there is no phase distortion, clock signals are reconstructed while the data remains zero. As shown in Figure 3.9, the phase distortion is detected to 1-bit ADC.

The digital blocks were combined using only standard cells, excluding IO cells, the GDS file was extracted and ported to Cadence Virtuoso, and the layout was completed by connecting to analog I/O pins. Connecting analog I/O pins is designed to prevent signal distortion by inserting an appropriately sized buffer according to the load value extracted from PEX.

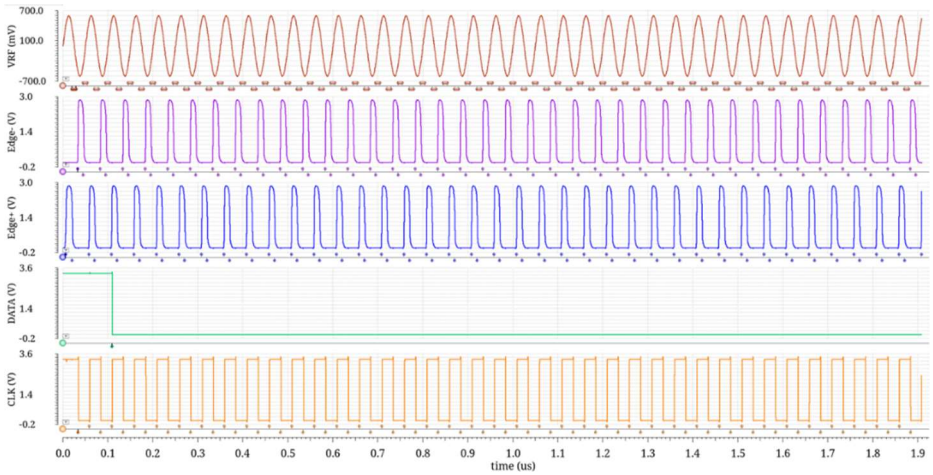

Figure 3. 8. Signal process of clock recovery circuit

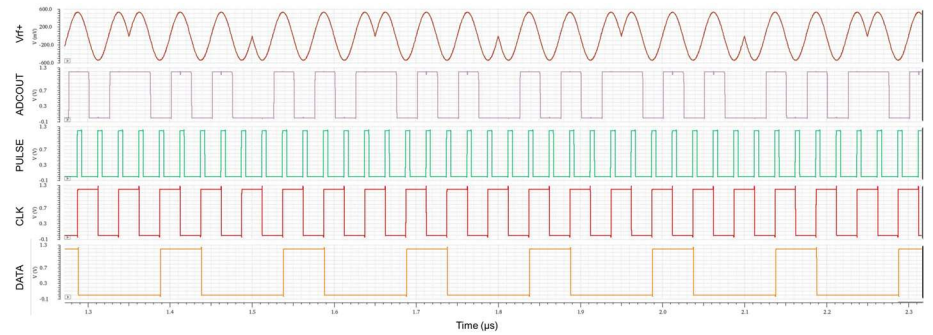

Figure 3. 9. Signal process of DPSK demodulation circuit

Unlike conventional data transceivers, backscatter communication uses an RF source from a Tx coil to convey data, meaning there are no additional amplifiers or RF generators for the transmitter. It allows the system to operate in low power and compact size. From the ISM band frequency, a suitable frequency for wireless data transmission is decided considering the size of the system and penetration depth of field interacting between inner and outer devices. 13.56 MHz frequency seems appropriate for their antenna size and 4 cm depth. However, as the clock signal is recovered from the carrier frequency, we chose 16 MHz for accessibility.

Figure 3.10. depicts the wireless data and power transceiver of our system. The external demodulator filters out the neural data from the carrier frequency with the duplexer. According to the serial data from the recording front end, the modulator turns on-off the NMOS, which eventually changes the load of the coupled coil. Meanwhile, the same coil stimulation control command is sent through phase shift keying modulation. Time-varying loads made of NMOS are placed right in front of the rectifier.

The digital control unit is designed with a block that sequentially transmits 128-channel quantized neural signals to the wireless data transmitter, a block that controls the on-off of the analog multiplexer, and a block that generates a phase synchronization code to notify this. A phase-locked code is placed in front of the 127 quantized signals and is generated at every starting point. The timing diagram of the designed digital controller is shown in Figure 3.11. In the system, 16 amplifiers and 1 SAR ADC make up one module, and 8 modules combine to implement 128 channels. SEL[7:0] is a signal for selecting one of

8 modules, and VC[15:0] is activated when digitized data of one channel is extracted from a module composed of 16 neural recording channels. For example, our animal experiment used 732 HzS/s for ADC with a modulating frequency of 1.5 MHz. External duplexer filters out carrier frequency and targets the modulating frequency. The backscatter modulation follows the serial data from the digital control unit. The power consumption of the digital section at this clock is about 200 μW.

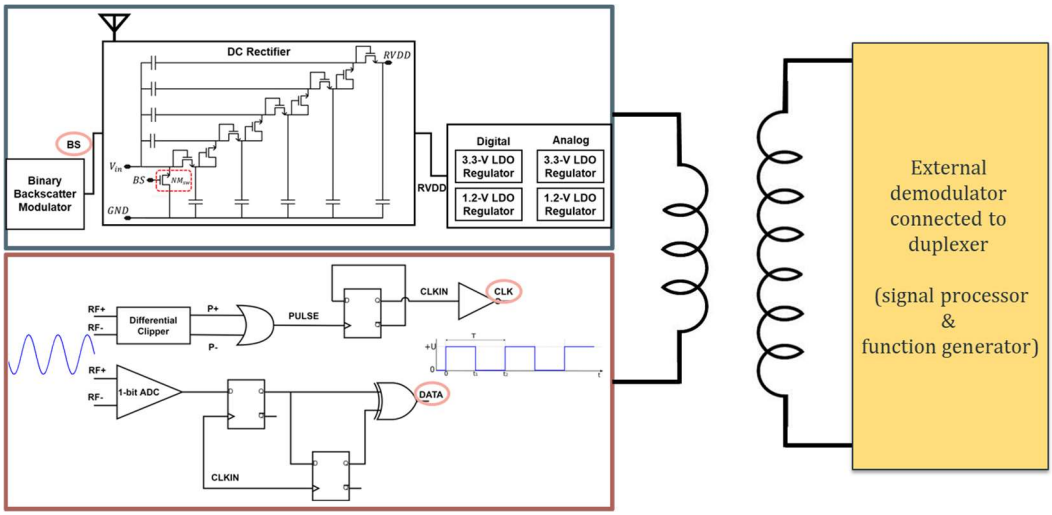

Figure 3. 10. Circuit diagram of bidirectional communication

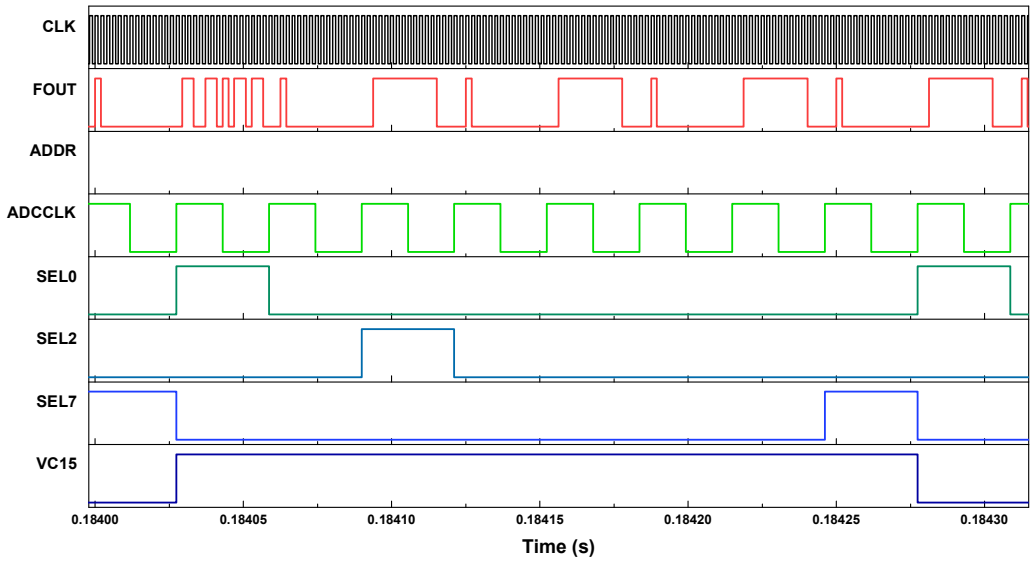

Figure 3. 11. Timetable of digital logic between the ADC and backscatter modulator

3.2.4. RF Energy Harvesting

The basic principle of energy harvesting circuits is short-range communication (NFC to 13.56 MHz) based on electromagnetic induction. This wireless system requires a transmitter with a loop antenna that is adequately aligned to the receiver circuit implanted in the brain to transfer power efficiently. Applying the NFC approach to wireless power enables a cheap and relatively simple method for wireless implantable neural systems. Additionally, this wireless powering methodology utilizes the low-frequency near-field and has lower specific absorption in laboratory animals compared to far-field systems and lower losses than higher-frequency bands. Although implanted devices can be small, large coil sizes (more than 10 mm in diameter) limit the implantation of multiple devices. Energy generation in our design uses a 16 MHz carrier frequency.

We customized two near-field resonance coils to optimize the efficiency of electromagnetic transfer between the Tx and Rx coils from simulation to fabrication. HFSS simulation proceeds using a human body layered model composed of skin, fat, bone, and muscle. In Figure 3.12. the 3D simulation with HFSS shows electromagnetic field propagation between the two coils. The antenna coupled in that carrier frequency uses a matching capacitor showing S(1,1) feature as in Figure 3.13. By using the smith chart, onboard components are used to match the output input impedance of the antenna to 45 Ω. Also, the customized coil with a matching circuit is verified by comparing the simulation and measured results.

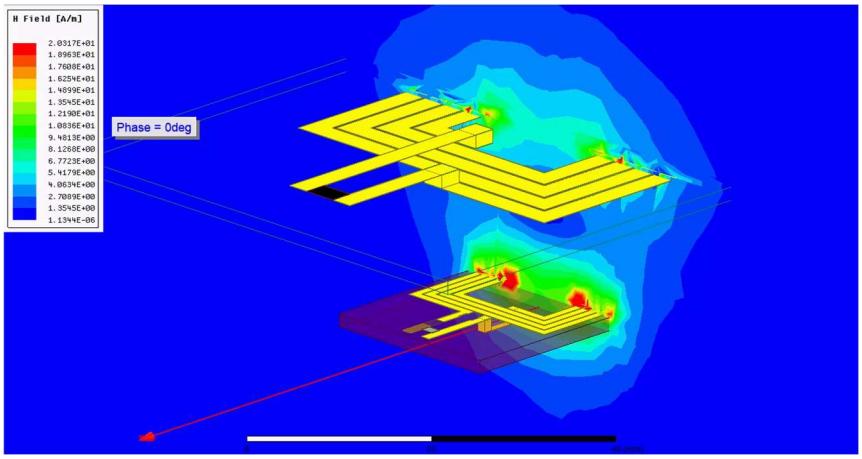

Figure 3. 12. HFSS simulation result of 16MHz matched coil designed in F-PCB

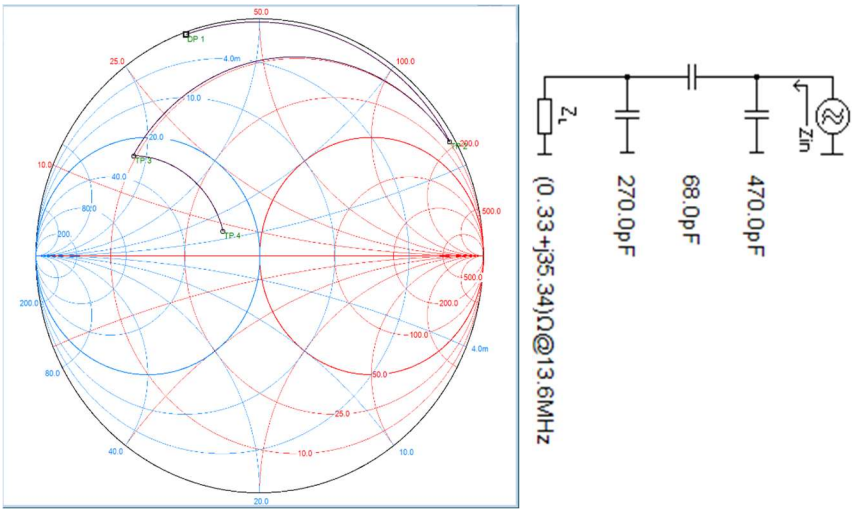

Figure 3. 13. Impedance matching of coil antenna. Smith chart and equivalent circuit for matching the impedance to 45 Ω

Figure 3.14 shows a zero-threshold rectifier with a voltage multiplying stage. For the LDO (Low Drop Out) regulator to generate stable 3.3 V output, the rectifier uses 4 stage architecture. It employed a native NMOS transistor for the lower threshold voltage. Implementing only NMOS makes it easy to integrate bulks at the ground. The modified DC rectifier is designed based on the Dickson charge pump rectifier. In the single-stage, (Cp-pF) blocking capacitor stores leaking current which turns on the following transistor in the next stage. For example, a passive rectifier uses a diode connection transistor as a switch, allowing current to flow in one direction during one cycle. It requires the input AC signal above the diode threshold to turn on this switch, the V_{th} of this transistor.

In this case, a dead zone occurs when the rectifier does not flow current when the input signal is less than Vth. Knowing that V_{th} is a small amplitude signal processing in which the collected energy of the insert is attenuated by penetration loss and does not scale well with the reduction technique can be a real problem facing the power supply design for NFC tags. It is recommended to improve induction link power efficiency and minimize induction output voltage for insertion into most induction power systems. The 5 stages of the Dickson voltage rectifier are determined based on the stage calculation for target output voltage as in [94]. As the LDO regulator needs at least 3.7 V to start and produce a constant 3.3 V output, we calculated the number of the stage with 500 mV_{pp} sinusoidal input.

If the designed rectifier receives sufficient power, two LDO regulators will be turned on. One LDO supplies a stable supply voltage to the stimulation

system, and the other supplies for neural recording module. If we think some parts need noise-chopping techniques, we design another LDO block separately. The regulator consists of a conventional PASS transistor, an error amplifier, a startup circuit, and a reference voltage generator. The overall target gain is over 80dB, and the phase margin is 60°. Recently, capacitor-less regulators have been reported frequently. In our design, as shown in Figure 3.15, we use an off-chip component of a 1 μF capacitor to solve the phase margin problem.

Rectifier provides a 3.7 V output voltage to the 500 mAh battery through the coil antenna. A rechargeable battery was added optionally during animal experiments. Figure 3.16 is the battery charging characteristic through a wireless energy harvesting circuit.

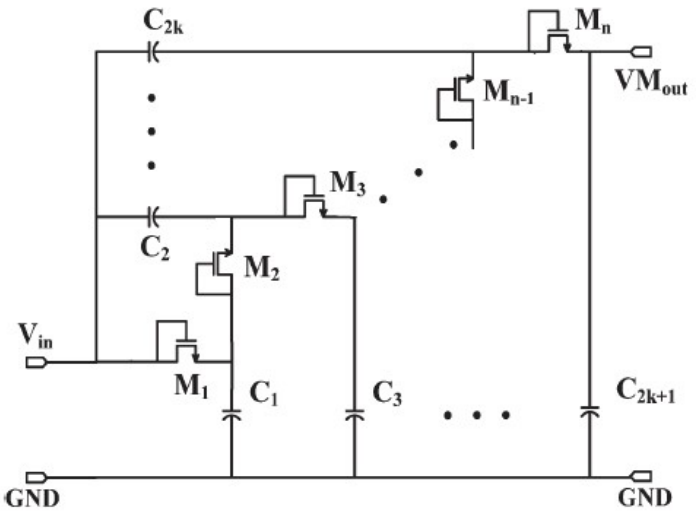

Figure 3. 14. Circuit diagram of N-staged Dickson rectifier

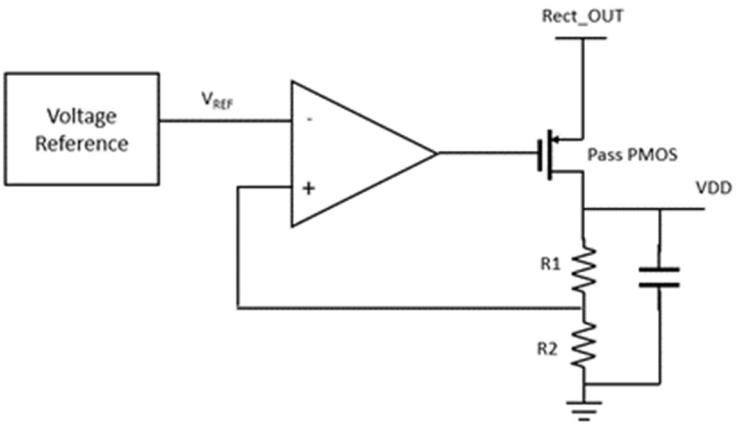

Figure 3. 15. Circuit diagram of low-dropout (LDO) regulator

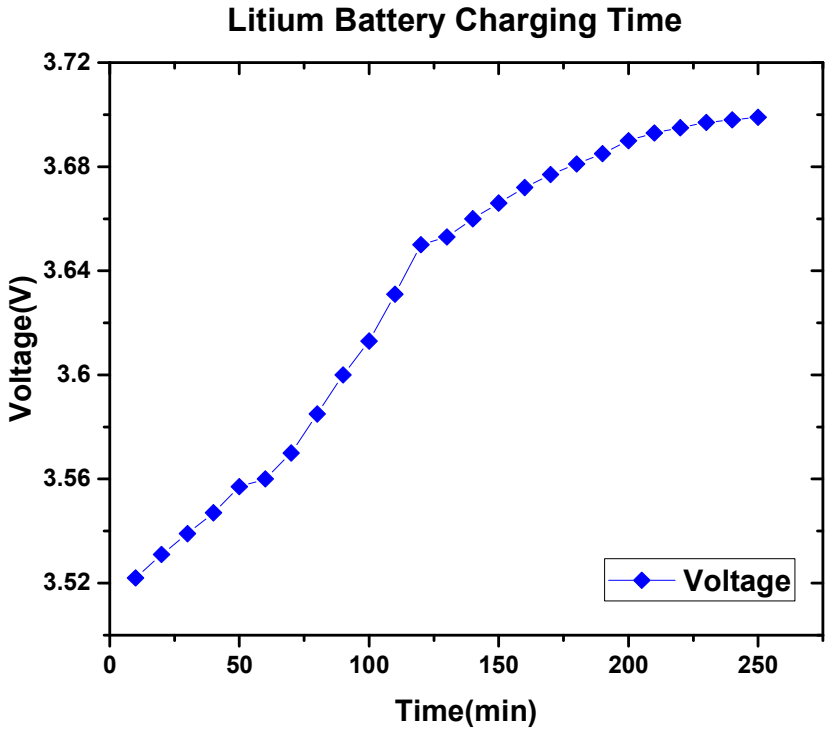

Figure 3. 16. Rechargeable battery charging characteristic

3.7 V source from the rectifier output charged the battery. The charge protection circuit integrated into the battery ensured safe and fast charging even from the coil antenna.

3.3. Experimental Methods

3.3.1. Benchtop Experiments

The photos in Figure 3.17 show two system prototypes with different communication methods. Both prototypes' multi-channel recording and stimulation circuits used the same core circuit and were analyzed and evaluated in air and PBS solution. A separate radio data communication version was tested to compare overall power consumption and data transfer performance.

In comparison, in the bidirectional communication method, the first design received stimulation commands using Bluetooth, and the other received all data using one coil. The wireless data transmission using the BLE module used a different data format known as UART with the 1843200 bit/s baud rate. This condition allowed a sampling rate of 732 Hz. Only 96 channels (64 recordings & 32 stimulation) were available with the limited data rate.

On the other hand, the second prototype assembled the antenna and other passive components on a 9 cm^2-sized PCB. There is a clock & data recovery, and demodulation circuit for data communication. A function generator and spectrum analyzer were used to generate and analyze the RF signal. Also, the system's power consumption was measured using a power meter.

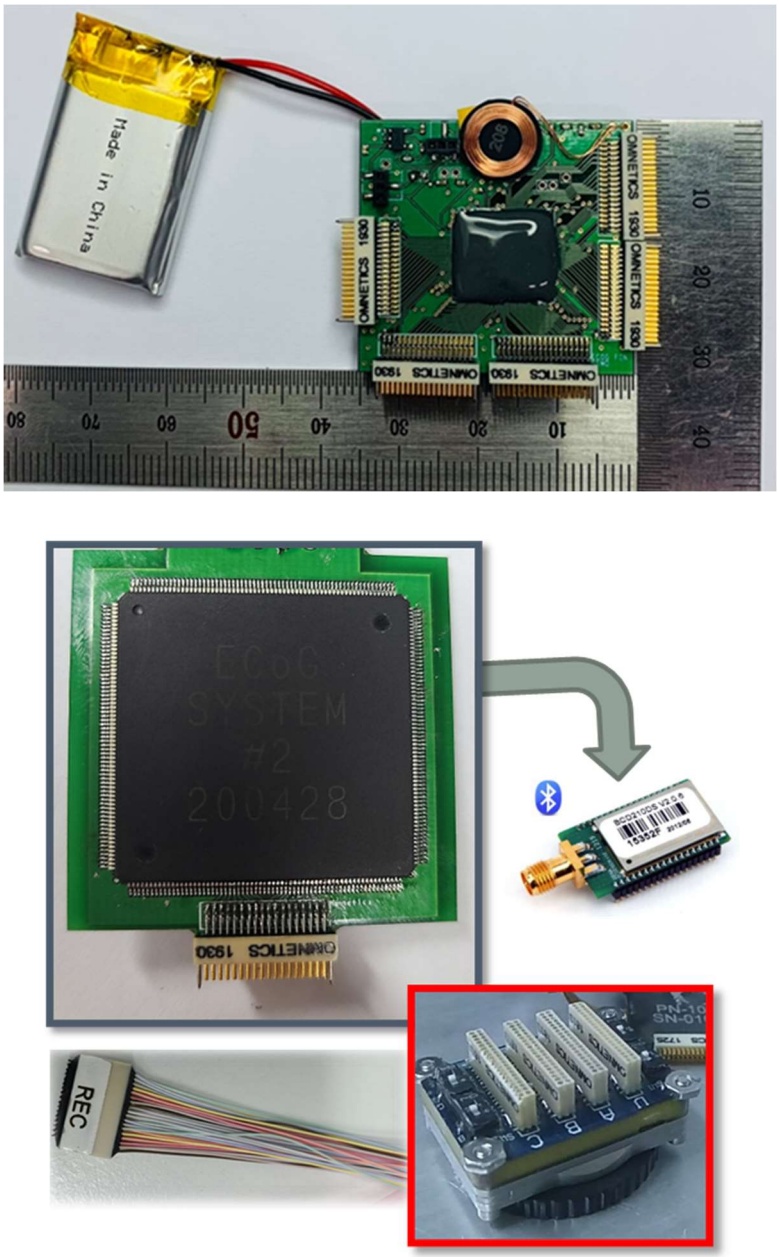

Figure 3. 17. Evaluation boards for core ASIC (top), LQFP packaged IC integrated on board with BLE module (bottom)

Several test steps were performed to evaluate the IC thoroughly. Stimulator validation focuses on the characterization of charge imbalance, pulse shape consistency and accuracy, and power consumption. The data transmission performance is first tested independently, then simultaneously. Power transmission efficiency and data error rate are compared with simulation data and measured data. Phantoms mimicking body layers are designed for validation as the device is implanted in the body.

The phantom was created to test the in vivo environment in which the device is inserted. Gypsum plaster was the chief ingredient for the skull phantom fabricated using distilled water in a rectangular film box. The skin, fat, and CSF phantoms were fabricated with agar, glycerin, polyethylene powder (PEP), and sodium chloride. Here, distilled water can be said to be the standard for all solid phantom relative dielectric constants. NaCl controls the conductivity, and glycerin and polyethylene powder handle the relative dielectric constant. Agar is used for maintaining the shape and has a low influence on the permittivity. They were cooked and prepared in a laboratory at room temperature [95].

Experimental setups of both air and phantom are designed as shown in Figure 3.18 and Figure 3.19. The ruler and antenna stander help accurately control the distance in wireless telemetry validation.

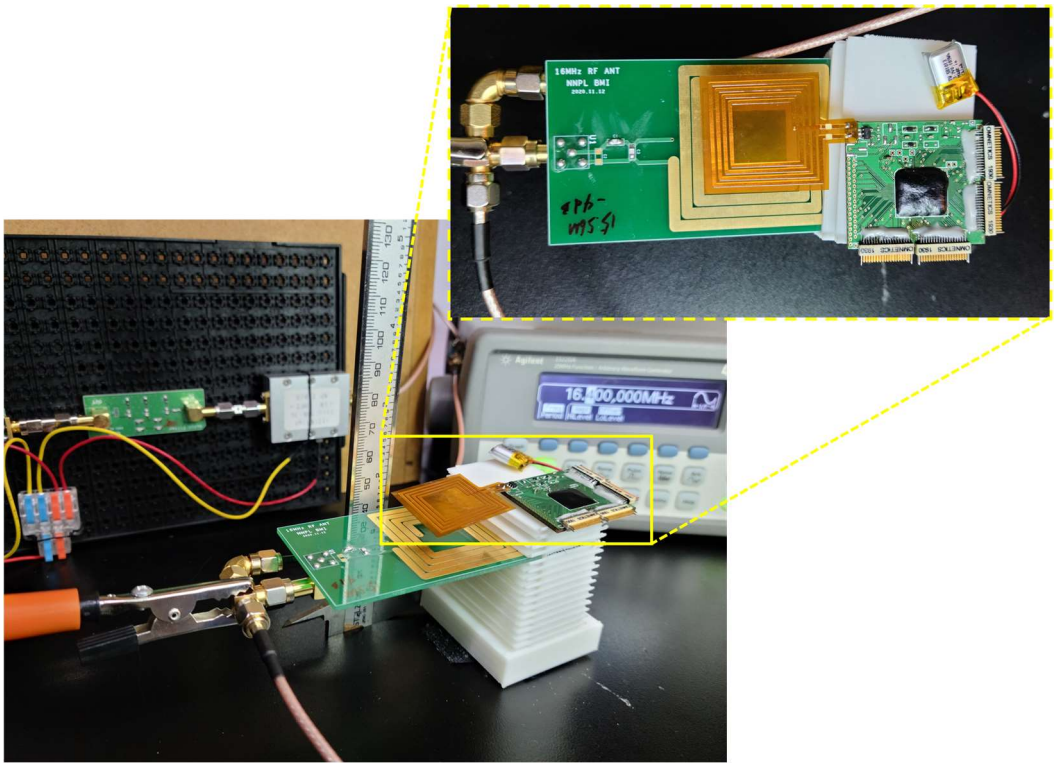

Figure 3. 18. Experiment setup of bidirectional communication in air

1-4 cm distance between the antenna was analyzed by comparing PTE. Also, we swept the source frequency remaining the same power to find the matching frequency.

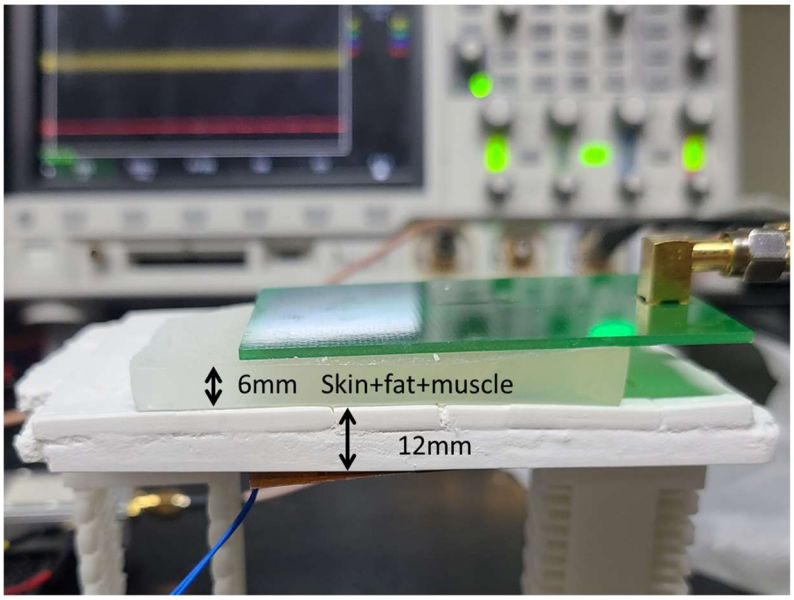

Figure 3. 19. Bidirectional communication test with tissue and skull phantom between

Unlike the results from the air, power transmission with a phantom sandwiched between showed a sharp decrease in power, but the error rate remained the same

3.3.2. Animal Experiments

Non-human primates are the final stage of animal experiments and are considered the prelude to human clinical trials. Our system aims at a brain-machine interface for realizing the movement of the upper extremity of the right arm by recording ECoG. To this end, the M1 signal is recorded, and a stimulus signal is given from the somatosensory cortex to implement accurate upper extremity movement like a machine. Some research has shown that ECoG signals from the motor cortex in the 70–160 Hz range strongly encode actual and imagined motor activity [96]–[99]. Also, the signal band under 40 Hz, particularly the beta band (18-30 Hz), is known to be correlated with sensory-motor integration [100]. The device's performance was evaluated with the help of researchers from Sungkyunkwan University.

We implanted two 96-channel intracortical microelectrodes (Utah array, Blackrock Microsystems) into the left hemisphere primary motor cortex (M1) and parietal cortex (5d), respectively. One male rhesus monkey (Macaca mulatta), an 8-year-old, was used in the experiment (6.7 kg). All procedures were performed under the guidelines for the welfare of experimental animals approved by the Institutional Animal Care and Use Committee in the Daegu Gyeongbuk Medical Innovation Foundation (DGMIF17021003-01).

When an external device for collecting cranial nerve signals and electrical stimulation from an implanted multichannel electrode array is connected to a primate, the primate is at risk of shaking its head and damaging the connection device. Also, as our power and data transmission relies on a near-field communication antenna, the abrupt movement could cause data loss. Therefore,

the head fixer is used during the experiments. The experimental setup shown in Figure 3.20 has been constructed to measure up to 192 channels using the black rock electrodes (A79025, Omnetics Connector Corporation) and head stage. The detailed features of electrode mapping are accessible in Appendix Ⅰ.

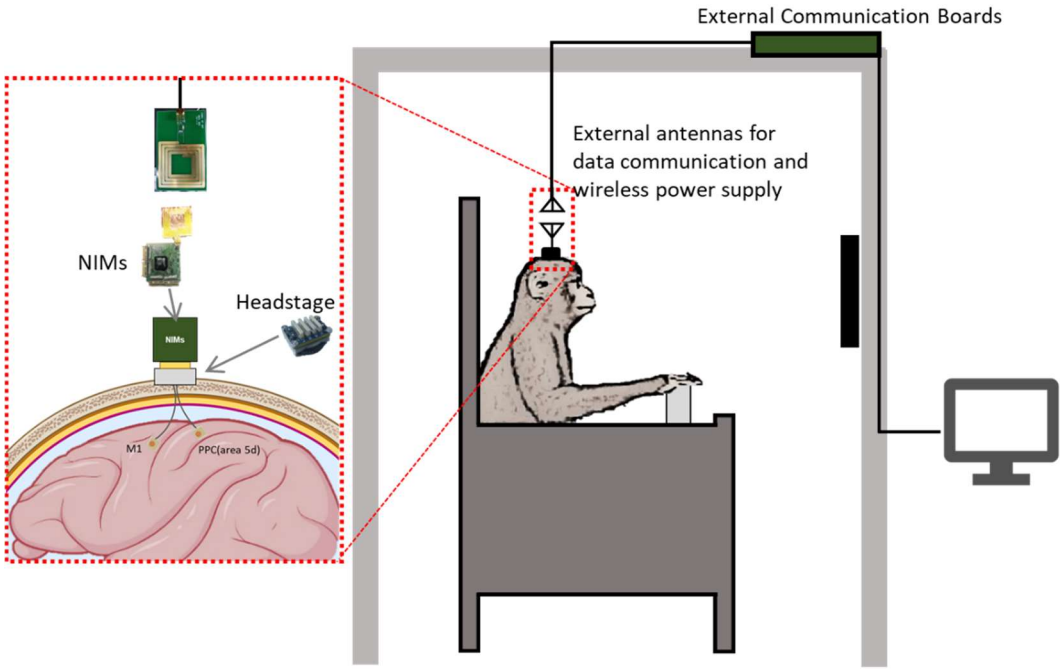

Figure 3. 20. Experimental setup of monkey head-mounted system

3.4. Results

The bidirectional neural interface needs recording of the neural activity while delivering sensory feedback through electric stimulation. The 128-channel analog frontend into the same SoC of the multichannel stimulator is suggested for compact neural interface implant. Figure 3.21 is the microphotograph of the designed IC.

Given the bench test results of our previous single-channel recording module, several parts are added and revised. Significantly, the number of channels of each recording and stimulation module increased, and both data were transmitted wirelessly in different carrier frequencies. Also, the wireless data modulation scheme for receiving and transmitting parts is to avoid signal interference.

We have designed a neural signal-measuring low-noise amplifier for several years and verified that it has a 3 μV input-referred noise while consuming 1 μW of power. The neural recording amplifier that is being recently reported consumes a few microwatts of power, and the input-referred noise is generally several microvolts or less. Since the neural signals are widely measured from 5 mV to several tens of microvolt, at least the system noise should be less than 10 μV considering the signal-to-noise ratio.

The A/D converter type that we are designing is a successive approximation register, and we aim at a 12-bit resolution. The basic structure consists of a capacitive array, comparator, and SAR logic. After the SAR A/D logic, 16 to 1 MUX is designed for serial data transmission.

Due to the LNA implemented at each multi-electrode array, a low-noise neural signal is earned in real-time. Compared to the previous design, the gain of the amplifier is improved, and the whole chip size decreases by 8%. The data, considering the bad WDT efficiency and the idea of dividing the input serial data into two modes so that the device does not need to process all data every time, did not show many conveniences and instead had a bad influence on overall setup and increased data error rate.

For its flexibility and low threshold stimulation, the stimulator design is based on effective stimulating parameters, so selective stimulation of neurons is available. Hence, the temporal and spatial resolution could be increased compared to the number of electrodes. Each 36-bit binary data controlled the CMOS switches and changed the parameters to find optimal pulse parameters. This design is targeted to test the data transmission and verify the constant current flow while varying load impedance. Also, the electromagnetic field would be examined with the electrode attached at the back end of the system.

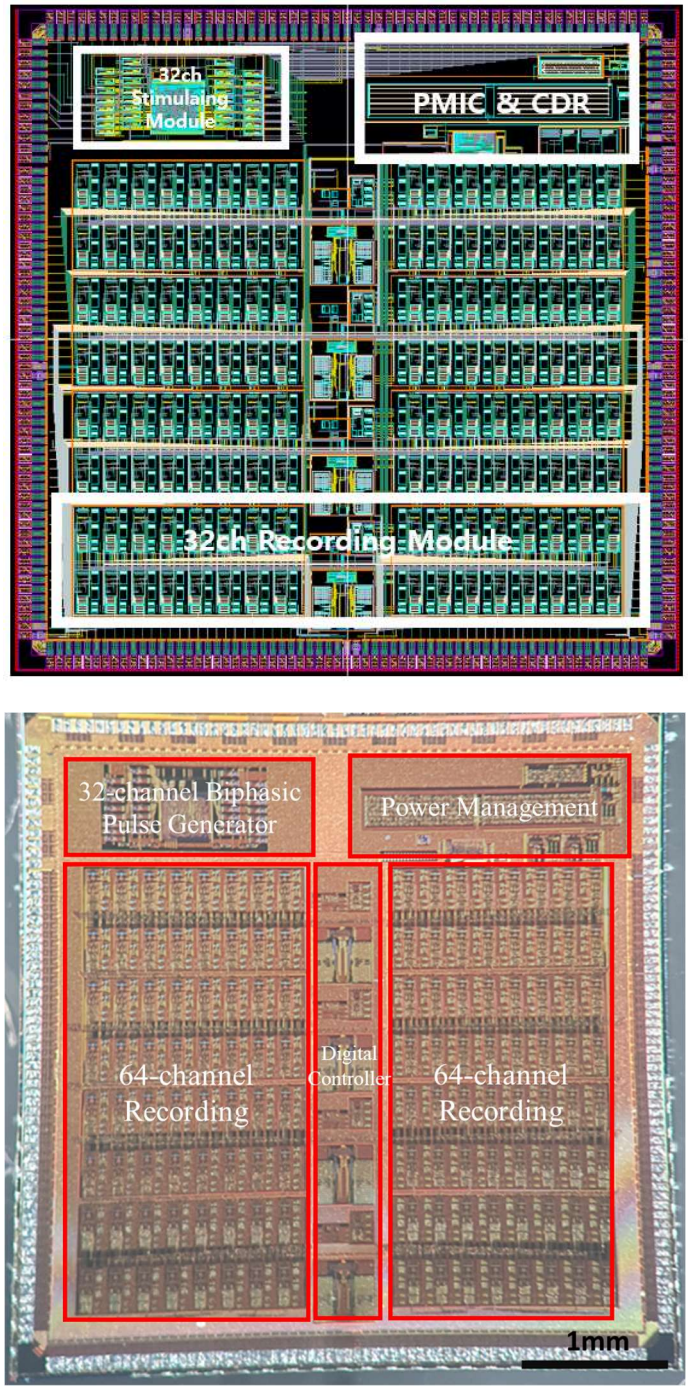

Figure 3. 21. Layout and microphotograph of bidirectional BMI IC

3.4.1. Multichannel stimulation with recording in real time

The results obtained when the recorder and the stimulator were operated concurrently are shown here. Figure 3.22 shows the analyzed results of the system in PBS solution. The result revealed that system noise up to the wireless module is about 5 μV_{rms}, consuming 390 μW when measuring a 5 Hz and 60 μV_{pp} sinusoid signal and baseline signal in PBS solution. According to the recorded frequency range, the analog filter with a cutoff frequency of 300 Hz filters out the stimulation artifact before the digital filter.

Next, the error range of stimulation pulse parameters was evaluated through repeated trials. Both resistors and PBS solution characterized the biphasic pulse generator (BPG). The maximum amplitude was 280 μA over 10 - 1 kHz pulse frequency and 50 μs - 3 ms pulse width. The stimulation pulse shape is determined by referencing the duration of the clock, which is 1 MHz. LSB of pulse width and frequency is modulated through the counter and saved in the state machine. Figure 3.23 has two different pulse shapes modulated from the phase controller. Interphase delay and first phase are defined in the serial to the parallel converter in the logic controller.

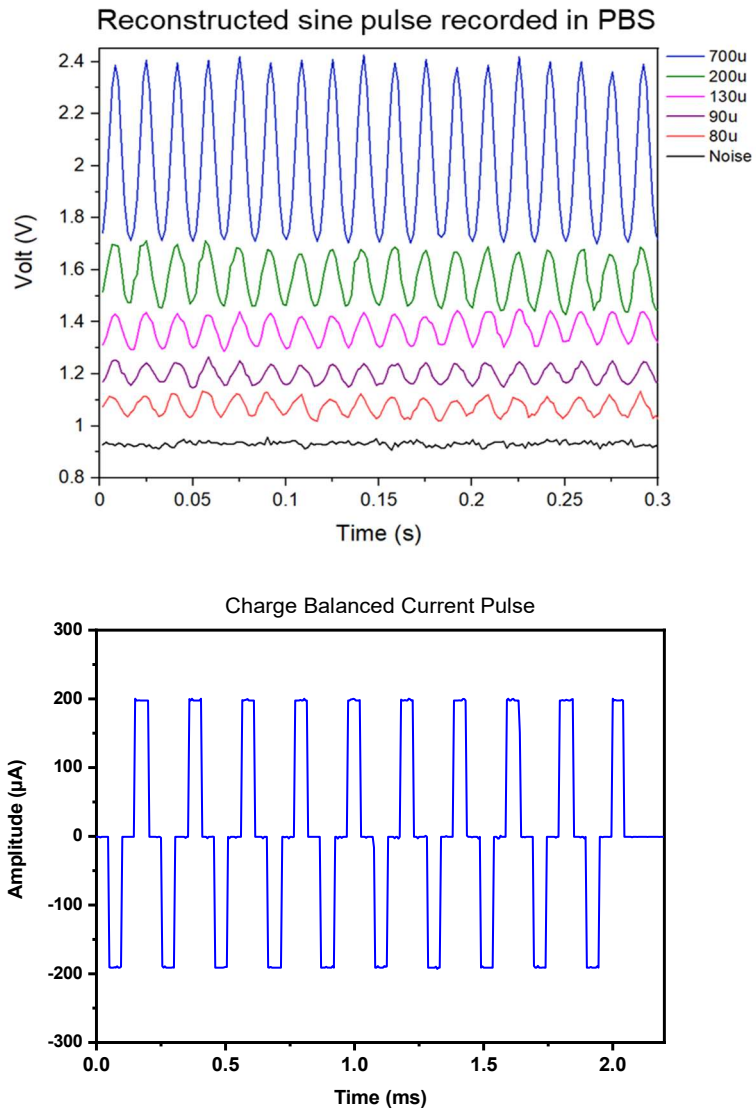

Figure 3. 22. Evaluation results in the PBS solution

The figure shows clean reconstruction results of the recorder during stimulation operation. Also, in the PBS solution, the stimulation pulse had a uniform biphasic square wave.

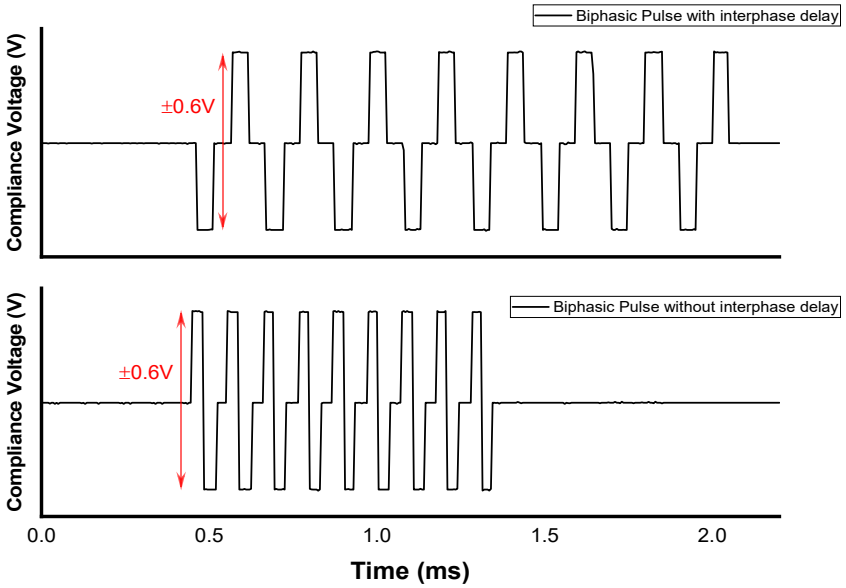

Figure 3. 23. Biphasic pulse recorded in PBS solution

Researchers have reported that the interphase delay in biphasic pulse prevents charge accumulation and dc offset from increasing near the electrode. With the programmable stimulator phase, pulse width, frequency, and amplitude could be modulated. A differential probe was used to measure the floating stimulus in the PBS solution.

3.4.2. Bidirectional Communication

The DPSK data recovery block is next to 128 channel recording module and post-data processing digital circuit. Above it is the 32-channel stimulating module and power management circuits, including 4 stage dc rectifier and regulator, using a 16 MHz carrier frequency. The area used in 5 mm × 5 mm chip space, excluding the Seal Ring and pad ring, is 4.8 mm × 4.5 mm.

In Figure 3.24., we measured the modulated RF signal received through the coil and the DPSK demodulated data and clock signal. After the phase conversion, the binary bit shows 1 for a single clock. The overall power consumption of the demodulation circuit was about 430 μW. The error rate was checked by transmitting the monotonically increasing pattern. During the benchtop test, the data reception antenna was characterized using a spectrum analyzer to accurately determine the backscattered signal's frequency bandwidth.

The results in Figure 3.25 show baseband wireless power signal and recovered bit stream transmitted to the PC using FT232RL. Since the maximum sampling rate per channel for ECoG signal measurement is 1 kS/s, for a total of 128 channels, the digital stage must be driven at a rate of 128 kS/s. It takes 16 clocks to quantize a single analog signal, and the total clock required by the system is 2.048 MHz. The maximum clock available is 2.2 MHz, the upper limit of the analog filter successfully dividing the uplink and downlink. At that clock, the power consumption at the digital section is about 200 μW.

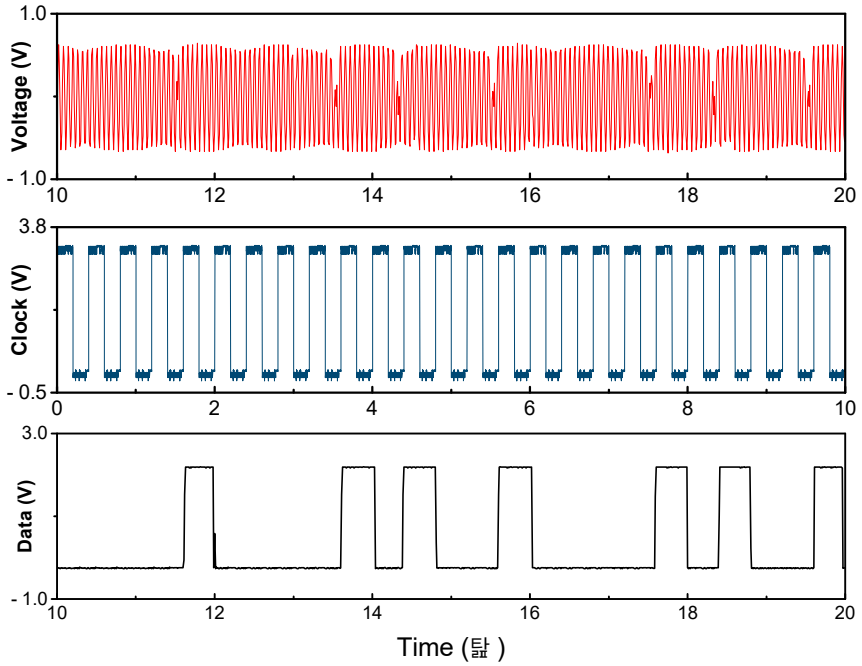

Figure 3. 24. DPSK demodulation results

It was confirmed that the downlink 2.5 MHz DPSK modulation signal, power transmission signal, and uplink signal backscattered at 1.5 MHz are separated independently by the custom-made low-frequency duplexer. With the clock, 732 kS/s sampling in ADC allowed 128 channel signal.

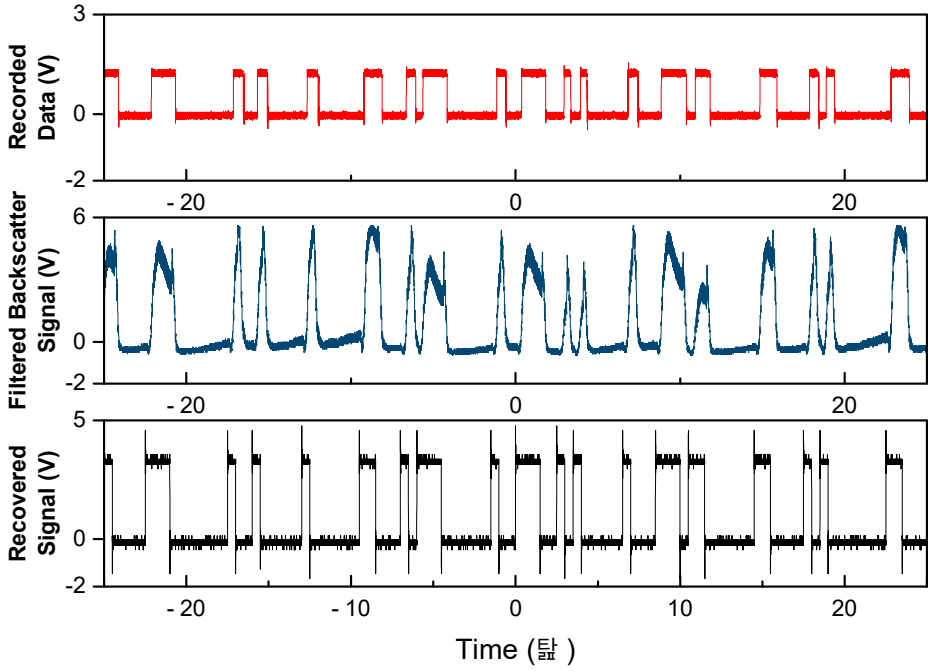

Figure 3. 25. Backscatter transceiver demodulation result

3.4.3. *In-vivo* Experiment

Figure 3.26 shows the experimental setup of the animal subject. Since the number of animal subjects was limited, a head fixation system was constructed instead of implantation in the body for safety. Bi-directional data transmission with BlueTooth and coil communicated with an external board connected to the computer. According to the in vivo experiment, bypass mode transmission with near-field RF communication Bluetooth had a negligible effect on time delay and data loss. To ensure that ECoG neural signal data from the motor cortex of a rat are received well in real-time, a two-channel recording and two-channel stimulation system were customized for the neural signal data coming from a rat. The graph in Figure 3.27 is the stack of recorded 128 channels through wireless data transmission.

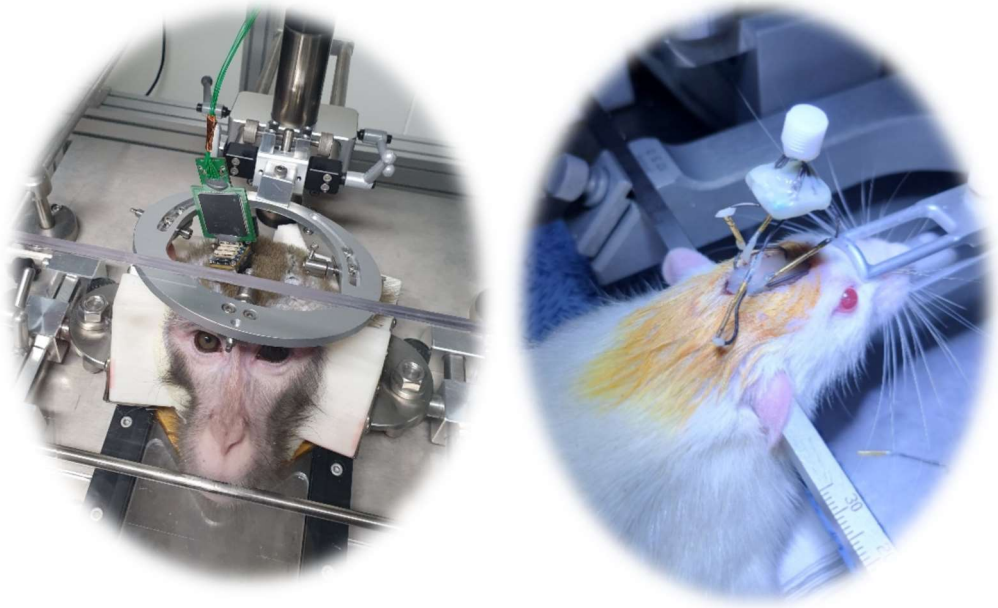

Figure 3. 26. Photograph of an animal experiment

Both monkeys and rats were the experimental subjects. Given the rat's head size, only some channels were used, and wireless communication experiments were conducted. The head-mount system with our core IC was individually designed. In both animal experiments, a rechargeable battery was additionally installed for stability to prepare for long-term experiments and sudden movements.

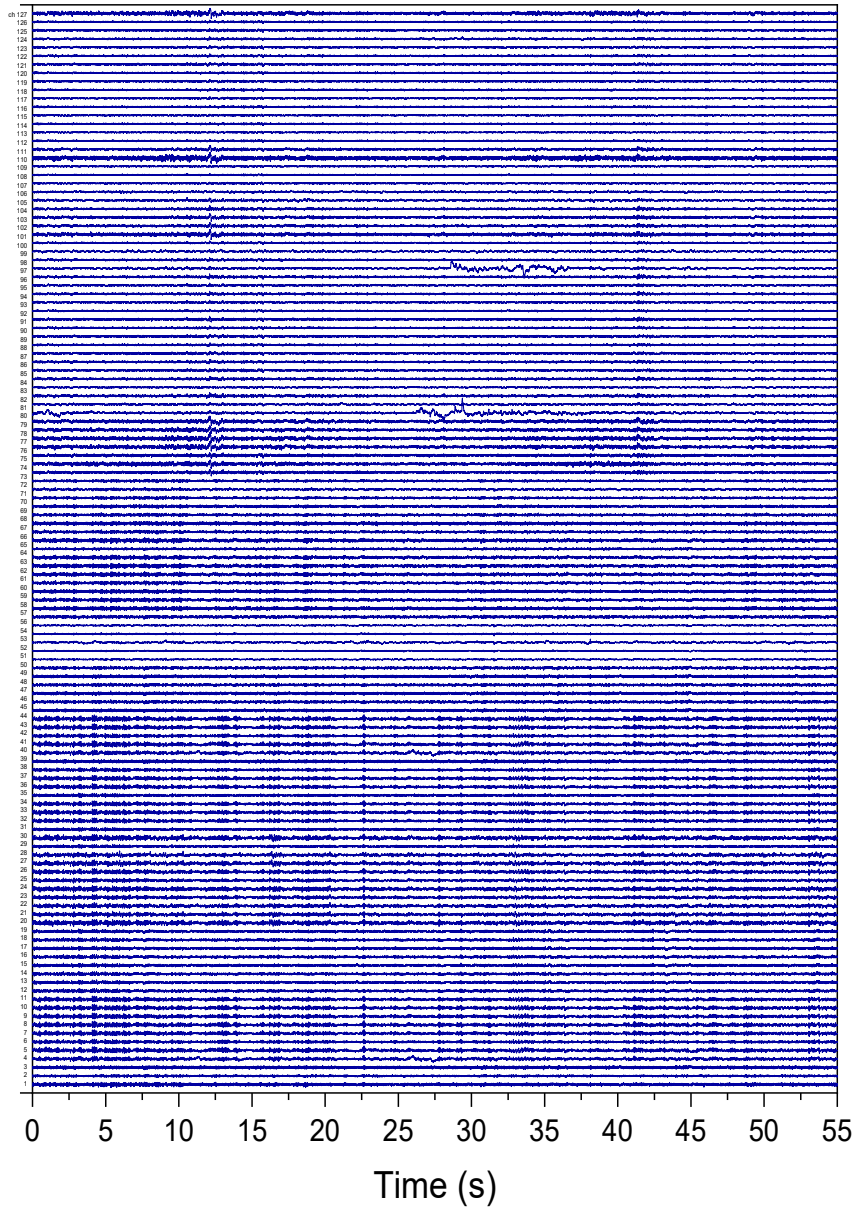

Figure 3. 27. Fully recorded ECoG signal. One-minute trial of 128-channel recording working with a sampling rate of 730 Hz in ADC.

Figure 3.28 (a) signal plots of recovered 64-channel recording of ECoG. The reference electrode sets the baseline of signal reconstruction. Digitized signals were calculated considering the sampling rate of 1 kHz and the total gain of 60 dB. The entire stimulus waveforms are not visible because the recording module's sampling rate per channel is lower than the stimulus's frequency component. In addition, the signal attenuation at a few kHz is insignificant because the analog filter embedded in the chip has only one pole. Thus, the applied current stimulation is not fully recorded but is monitored as a significant high-frequency component. Artifact removal with a moving average filter deleted the distortion from the raw ECoG signal. We displayed the raw ECoG signal with the artifact and after the removal, as shown in Figure 3.28 (b). The black line passes the ECoG signal verification algorithm using the water feeding tube for the feedback experiment.

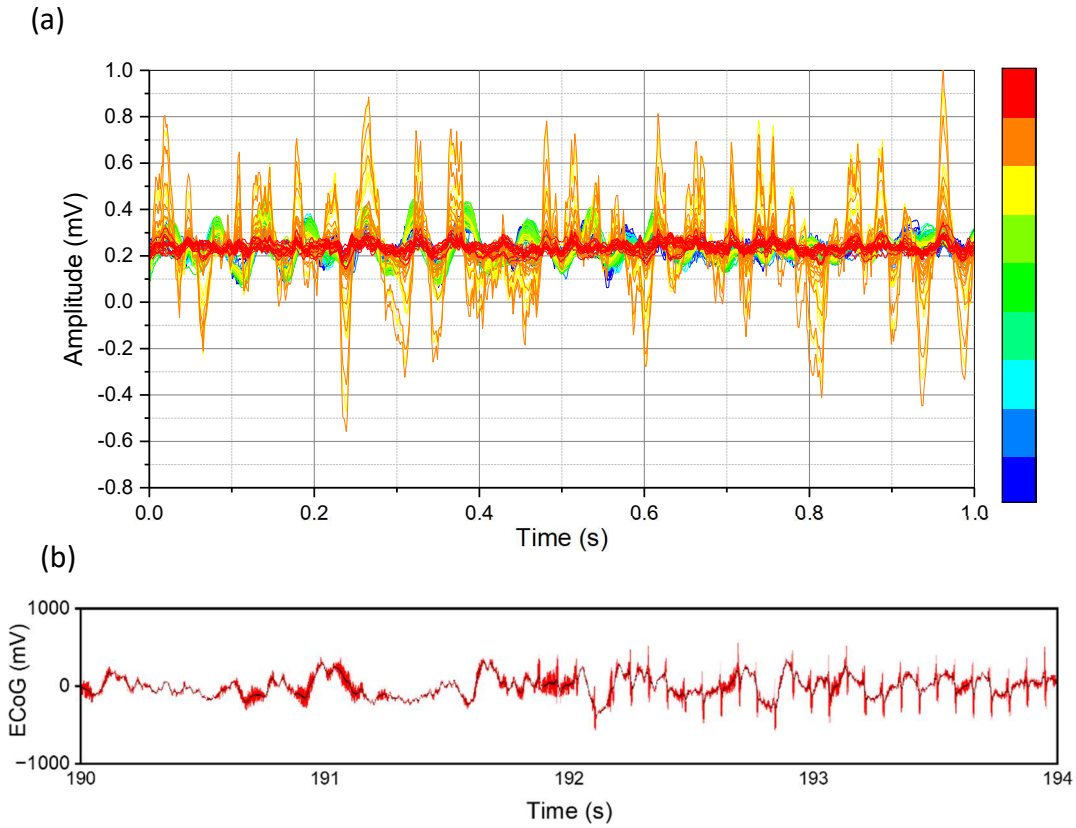

Figure 3. 28. Recorded multichannel signal and post-processing (a) ECoG signal recorded with 128 channel recorder (b) Recorded ECoG neural data with stimulation artifact and after its removal

MATLAB shows the partial elements of neural signal with a 4 s window. The placement of the window plot shown in Figure 3.29 in the GUI is related to the actual mapping with the implanted electrode. The buffer contains the data amount of 6 s and sends the packet of 2 s depending on the queue flag. This algorithm minimizes the data loss through a tight data rate and takes time to fix the error due to the lost bit.

The hand grasp response was induced at times t=10 s and t=30 s. In Figure 3.30, each trial was conducted for 60 s and recorded with both electrode and camera. 128 electrodes record continuous neural signals, which takes 60 s for a single trial. MATLAB captures the ECoG signal with every window size of 2 s and displays it in 4 s to show it as moving on one side. Subplots show the PSD of the single window during Trial 1. The PSD before, during, and after the stimulation shows the variation of the ECoG signal in different frequency bands. Also, we used Blackrock multichannel recording system to reference the noise level. The wireless system is well known for noise independence from ground noise. Figure 3.31 compares the noise level using the BlackRock recording system as a reference.

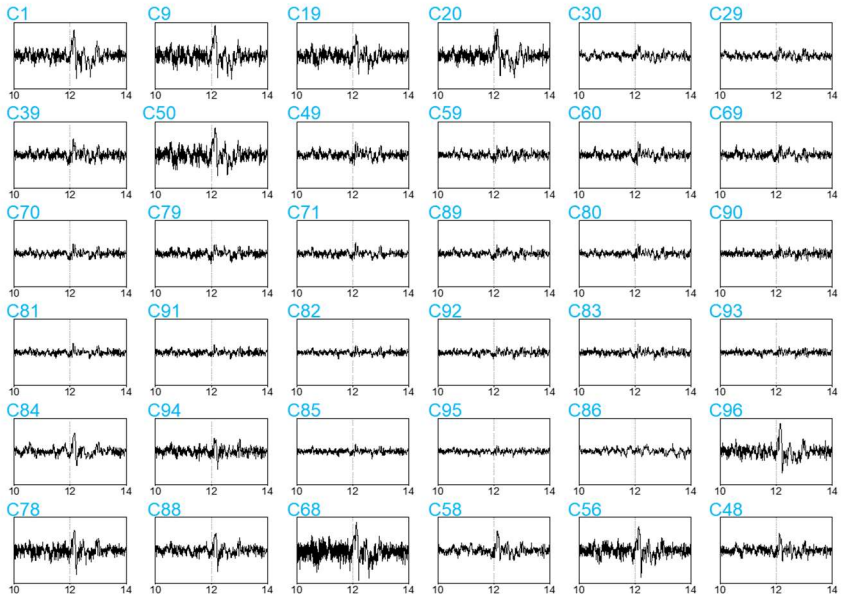

Figure 3. 29. The capture of the experimental results from 36 out of 128 channels in real-time through MATLAB. The chosen raw signal are mapped according to the channels in MEA

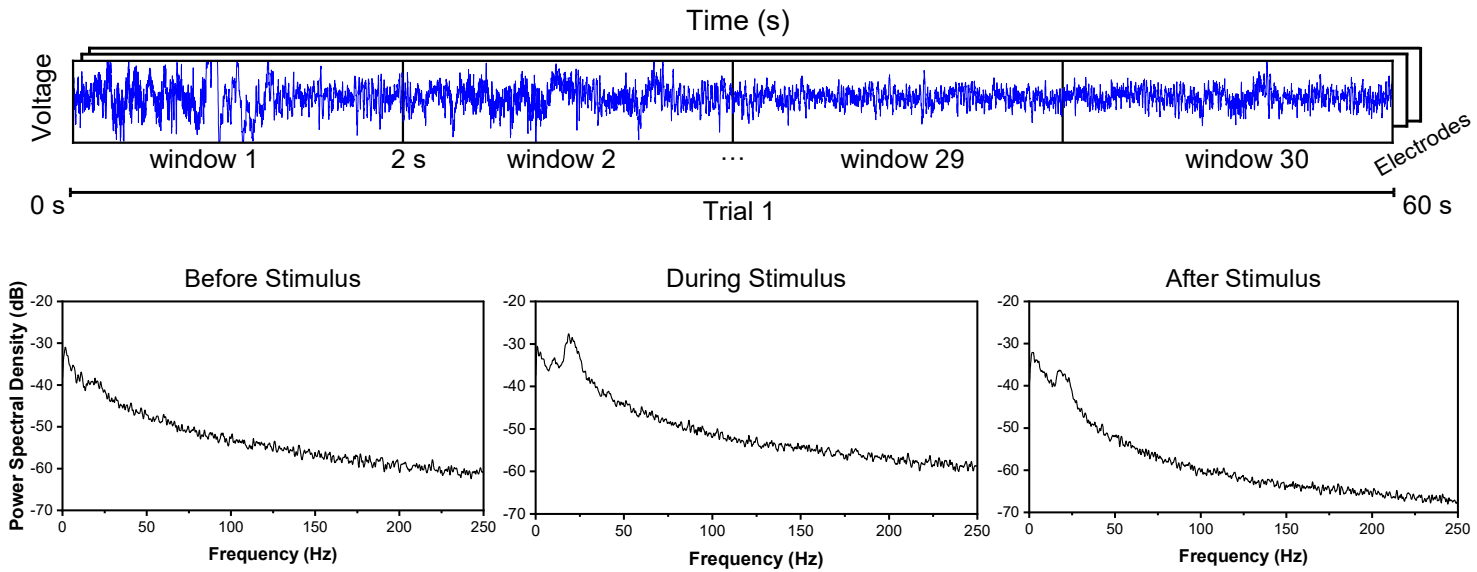

Figure 3. 30. Schematic of the real-time neural signal plot

128 electrodes record the continuous neural signal, which takes 60 s for a single trial. The window size of data processing is 2 s. Subplots show the PSD of the single window during Trial 1.

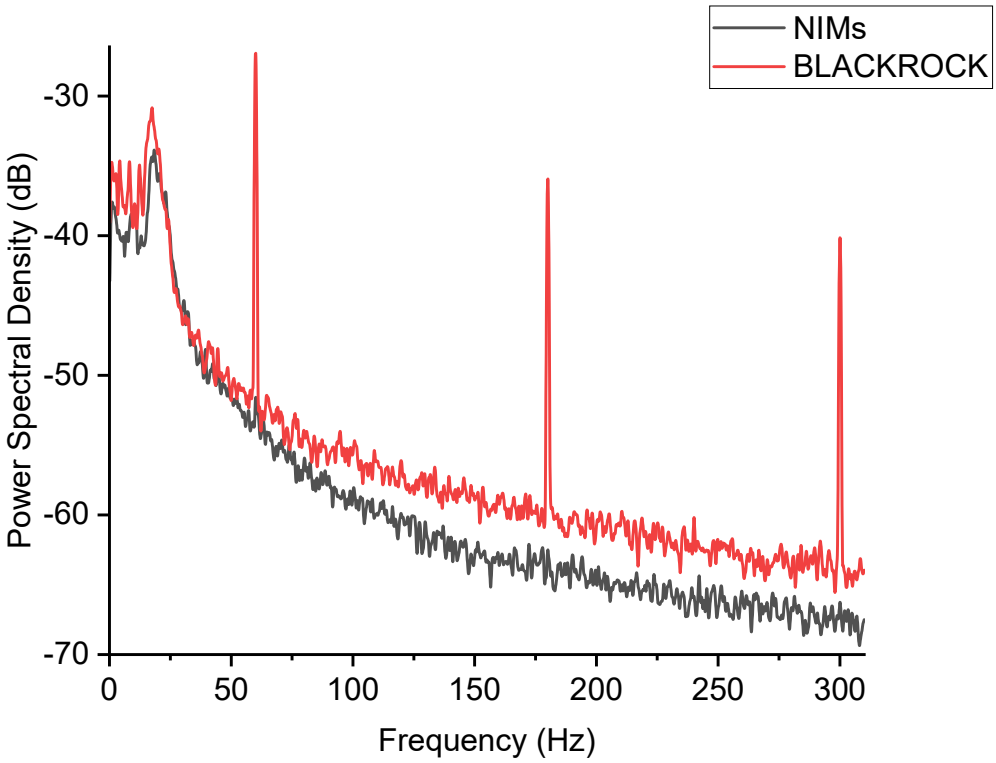

Figure 3. 31. Noise level comparison with commercial wired implant

Blackrock multichannel recording system with wired data transmission interface is used as noise reference.

3.5. Summary

Fully integrated bidirectional BMI implants and system efficiency are necessary from a cosmetic perspective. Also, the increased number of channels in a single system raises data bandwidth and makes it impossible to stream raw data wirelessly to the control unit. Internal signal processing of the implant is essential to reduce the bandwidth to enable wireless transmission. We designed an ultra-low power bidirectional BMI microsystem for electrocortical recording and stimulation. 128-channel recording and 32-channel stimulator are integrated into a single IC but work independently in real-time. Design considerations were to minimize noise and interference from the stimulus analog backend and affect the recording analog frontend.

Furthermore, our system has the advantages of having a higher number of channels in both recording and stimulating, fabricating at a smaller size, and operating with low power. The A/D converter type we designed is a successive approximation register with a 10-bit resolution. The basic structure consists of a capacitive array, comparator, and SAR logic. After the SAR A/D logic, 16 to 1 MUX is designed for serial data transmission. In the microstimulator, choosing charge balancing biphasic current pulse for stimulation allows it to give selective and precise stimulation without making leakage charge and high power consumption. Backscatter communication is an excellent way of transferring a large amount of data with low power consumption. The DPSK modulation method could sustain the rippling carrier wave and demodulate data. Since the fabricated system in this study transmits the measured neural signals

and receives the command by backscattering, thus the compact size and ease of operation are beneficial features for implantable devices. Also, the rechargeable battery guarantees a full-time investigation of approximately one hour. The system was integrated on a single IC occupying a 4.8 mm × 4.5 mm area. The detailed specification of the system is analyzed in Table V.

In addition, the efficiency of the wireless power receiving circuit, the efficiency measured at the bench top, and the efficiency of the fully integrated system with the antenna and packaging are pretty different. When inserted into a body full of electrolytes, the operating efficiency is often reduced to less than half due to various interferences such as scar tissue, water, or bones. Moreover, design specifications are given tight in the case of a low-power ultra-small system. As mentioned above, other factors that decrease efficiency are stimulation rate, mode, the number of electrodes (channels) used, and stimulation pulse parameters varying depending on the subject and disease. Therefore, it is vital to give a sufficient margin because factors decrease efficiency when applied to an animal model.

Regarding upper extremity rehabilitation, the bidirectional wireless operation with a transmission distance of over 1min shows benefits. However, sampling frequency and recording channel limitations remain unsolved. Based on our prototype, we would continue further study this system to develop an implantable system for behavioral tasks.

Table V System specification

	This work	[101]	[102]	[88]
Supply voltage	1.2 V / 3.3 V	3.3 V	1.8 V/3.3 V	0.8 V/1.2 V/5.5 V
Total Power Consumption	1.4 mW (rest) 20 mW (stim) 600 μW(record)	12-51 mW	172 mW	1.4 mW
Total Chip Areas	4.8 × 4.5 mm^2	35 mm (di) 10 mm (thick)	36 × 33 × 15 mm^3	3.2 × 0.8 mm^2
# of channels	128 max.	32	128	16
ENOB	9.3 bits	-	-	9.0/6 bits
Total Gain/sampling rate	60 dB / ~1 kHz	192/ 800 SPS/ch ~30 kSPS/ch	1000/ 1 kSPS/ch	34 dB/ 1 MHz,5 kHz
Bandwidth	3 Hz ~ 330 kHz	0.1-20 kHz	1-500 Hz	0.3-1 kHz
Input referred noise	~3 μV_{rms}	-	1.6 μV_{rms}	1.58 μV_{rms}
# of channels	32 max	4	8	16
Stim Current	~280 μA	40 μA	100 μA	~255 μA/2 mA
DATA RF link	DPSK/ Backscatter	2.4 GHz RF link with >uESB protocol	Bluetooth	UWB transceiver
Transmission	16 MHz	2.4 GHz RF	Bluetooth	1.6-1.7 GHz
High data rate	2.2 Mbps	-	Baud rate	10 Mbps

Chapter 4. Addressable Microstimulator with new ID-Generation Method

4.1. Introduction

Unlike conventional stimulators, distributed neural interface microsystems have the advantage over expendable and flexible system architecture. Challenges in scaling down the size of the system are not on the circuit integration [103]. The remarkable development of the semiconductor industry has made it possible to process a few nanometers. The biggest obstacle to reducing the size of integrated systems is the characteristics of devices that must be inserted into the body and communicate wirelessly. Existing multi-channel recording and stimulation systems have the same number of channels per unit area as microminiature single-channel systems, but there is a big difference in data and power supply and packaging for insertion into the body. Since the conventional system is relatively small, it is possible to add external passive parts, and above all, the energy harvesting efficiency is acceptable.

Taking an antenna as an example, as the size of the system decreases, the resonant frequency of the smaller antenna gradually increases. It is usually more than 10 mm in diameter when it is about NFC ~13.56 MHz and goes up to about 900 MHz at about 1 mm [104], [105]. Although there is no problem

communicating using the RF band, frequency scattering occurs due to moisture in the body environment, and reception efficiency is rapidly reduced. Even when using ultrasound [106] or a light source [107], the energy harvesting efficiency reduces because of size shrinkage.

Here, regarding power management, there are more problems than the recorder in the microstimulator. In the case of a stimulator, there is a significant difference in power consumption between resting and active states. In the case of high-rate stimulation, the fluctuation of the output waveform shakes the supply power as it is. In general, when the power source fluctuates, the amount of charge is supplemented using a charging capacitor, or the load in the circuit holds it. However, in the microsystem, there is a limit on the capacity of the capacitor that can be mounted. Some studies have reported using supercapacitors to complement the power management circuit [108]. Through diverse attribution and trials, the size of the microstimulator has decreased from more than 100 mm^2 in 2007 [109] to less than 0.1 mm^2 in 2019 [110].

The distinguishing feature of distributed microsystems from conventional neural interfaces is the ID generation circuit. It is designed to be a data transceiver sequentially communicating according to the order of IDs. ID is required to connect with numerous devices distinguishing each multi-channel node to verify the origin of the data.

However, conventional ID generation methods cause problems as the size of the system shrinks. A sub-mm micro-implant circuit is usually fully integrated, so there is little design space allocated to address the circuit. Table VI compares the recent development trend of microstimulator. With size

limitation, the circuit should be easy to encode as the broad aim of the distributed system is to expend hundreds to thousands of nodes. It is difficult to do one by one because it is substantial, and the number of address bits increases. Therefore, it is necessary to have one copy device and to grant it through post-processing.

The disadvantage of the existing method is that the pad size is too large. The number of pads decides the size of the system. The pad size of 70 × 70 μm for a 1-bit ID takes up quite a bit of area for up to 10-bit addresses. At least 10 bits of address units are required to configure an extensible system.

Among the methods, people study a lot in the early days. Large circuits are included (about 10 transistors). This has the disadvantage of having to allocate too much area for ID. Encoding using eFuse or PAD has problems because external voltage must be applied. Fuses made of metal or polysilicon can be optically cut by laser easily. However, the width and space of fuses cut by laser are not scalable in micro-implant, and the manual process is less efficient [114].

One of the methods being developed recently is to use PUF [115], [116]. The PUF is floating, and the process state and initial voltage determine the bias. So, the predictability is 50%. Due to process fluctuations, the probability becomes 50:50 (random number) [117]. There is a possibility of overlap, so make enough of them to reduce the possibility of overlap. It is challenging to overlap if you increase from 4 bits to about 10 bits. 20 bits are needed for 1 million pieces, but if 30 bits are used, it becomes a 1/1000 possibility and can be reduced.

Table VI Comparison of state-of-art microstimulators

	Microbead [111]	Stimdust [106]	ONG [107]	MagNI [112]	Charthad, Jayant, et al. [113]
Size	0.3 × 0.34 mm^3	2.2 mm^3	1.7 × 2.9 mm^2	1.5 mm^2	39 mm^3
Type	Voltage Stim	Current Stim	Current Stim	Current Stim	Current Stim
current	< 40μA	400 μA	25 μA	0.05–1.5 mA	22–5000 μA
power	RF	US	NIR	magnetoelectric (ME)	US
Target	Cortex	Peripheral	Intracortical	Spinal cord	Peripheral
tech	130 nm RF CMOS	TSMC 65 nm LPCMOS	TSMC 180 nm RFCMOS	TSMC 180 nm CMOS	180 nm HV BCD CMOS

4.2. Circuit Description

The system consists of the coil, power management circuits, stimulation core circuits, data demodulation circuits, ID-generation circuits, and digital control logic. Two different CMOS technologies are used for system design. Based on the design data from the existing 180 nm process, a single-channel micro-neural stimulator was designed in the 28 nm process. By using the 28 nm process, it was possible to utilize CMOS cells by classifying them according to circuit characteristics. Besides, the same design circuit can be implemented in a much smaller area through high-capacity capacitors such as VNCAP.

Table VII Stimulator specification

Supply voltage	1.2 V	1.8 V
Mode	Biphasic current stim.	Biphasic current stim.
Channel	8	1
Current	120 μA	100 μA
Pulse width	50 μs – 1 ms	50 μs – 1 ms
Frequency	5 – 1 kHz	1 – 400 Hz
Power Consumption	9.7 μW / 2.1 mW	1.96 mW
Power & Data Transmission	RF / On-chip coil	RF / Off-chip coil
Area	1 mm^2	0.41 × 0.39 mm^2
CMOS technology	180 nm	28 nm

4.2.1. Photodiode-based gate oxide anti-fuse cell structure

This section proposes a gate oxide anti-fuse one-time programmable ID array in a standard CMOS process. The schematic of the ID generation circuit and architectures of the anti-fuse and photodiode are illustrated in Figure 4.1. Since it is a method of controlling the anti-fuse from the outside using a photodiode, there is no need for a separate in-out pad or complicated circuit. When light is applied to the aligned photodiode while the setting voltage is applied, the anti-fuse is broken down, and a permanent volt is given, like OTP. This method has beneficial attributes in area utilization and time-saving in the encoding process.

ID generation array of the anti-fuse array consists of one thin oxide CMOS, one photodiode, and a CMOS readout switch. The source, drain, and transistor body are connected to form terminal 1 and gate form terminal 2. These connections are equal to MOSCAP architecture.

The breakdown path has been identified between the p+ polysilicon and the p+ source/drain diffusion. The body is connected to the terminal of higher voltage to prevent incorrect readings in case the breakdown happens between the gate electrode and the n-well. The unprogrammed anti-fuse stands high impedance, interpreted as high to the digital circuit.

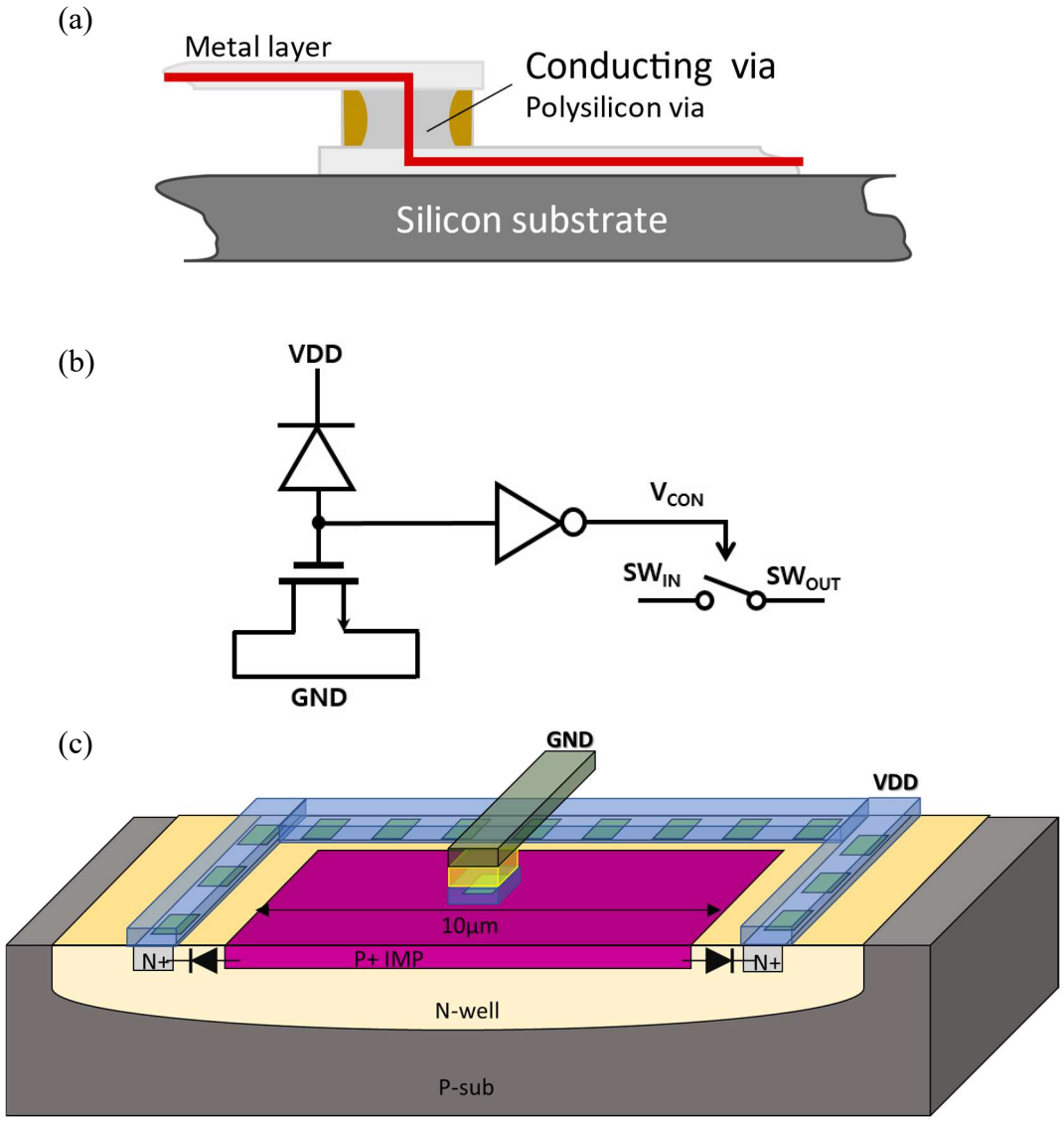

Figure 4. 1. Structural information of photodiode and anti-fuse (a) Gate oxide anti-fuse (b) Conceptual circuit diagram of ID generation circuit with photodiode and anti-fuse (c) Photodiode in 3-dimension

As the bias voltage of node 1 is determined by the relative capacitance-voltage of the photodiode and anti-fuse, the size of the transistor is deliberately decided based on the simulation result. Photodiode work as a triggering force to drive breakdown. According to the voltage supply, the current is minimal. Photocurrents help the system break down on smaller bias voltage. Figure 4.2 (a) depicts the layout of the photodiode and anti-fuse in the ID generation array.

Photodiode customized based on the simulation result. Fabricated photodiode layers utilized standard CMOS technology, and the relative layer thickness of the metal is as in Figure 4.2 (b). An ESD-connected high current blocker was added to prevent leakage current from causing breakdown. Current flows concentrate on increasing the stress level of the system. Also, bulk and ground separation from the reading circuit help remove different routes of leakage current. A high current is applied to the anti-fuse gate by irradiating light to the photodiode. A binary ID code is generated by selectively breaking down anti-fuse gate oxide.

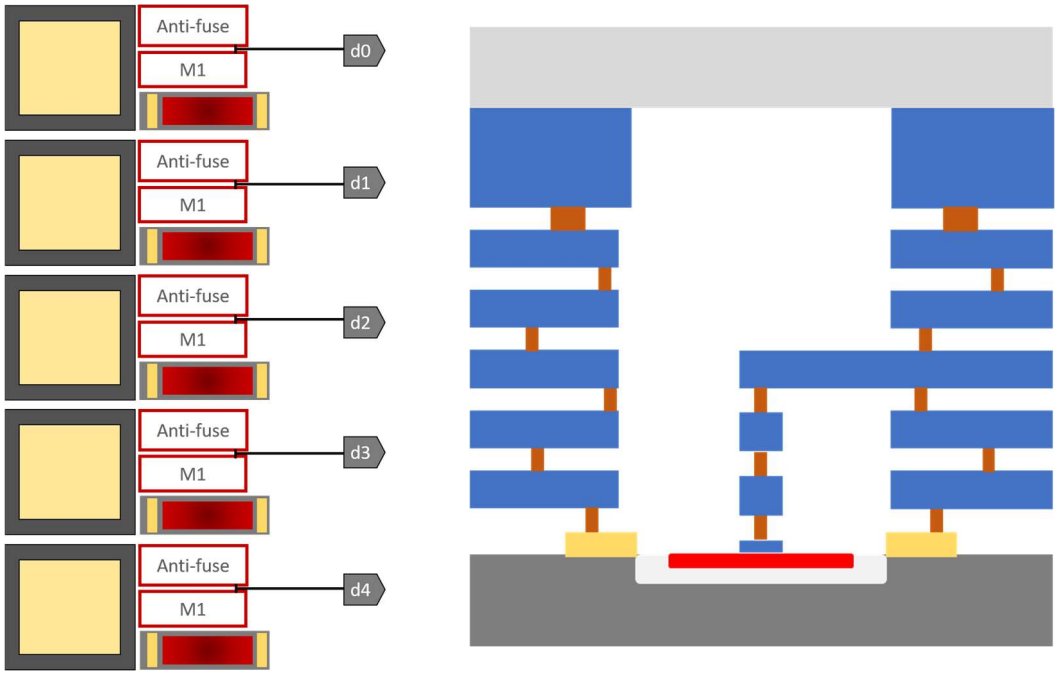

Figure 4. 2. Illustration of ID generation circuit. (a) 5-bit array (b) cross-section of the photodiode in standard CMOS process

4.2.2. Ultra-small microstimulator in 28 nm and 180 nm

- *Single channel microstimulator in 28 nm Low power process*

The proposed design utilized the high-density metal VNCAP, considering the capacitance ratio in the area. The actual capacitance of the NCAP and VNCAP are calculated with a parasitic value. Figure 4.3 shows the digital circuit layout and 1 pF unit capacitor made of VNCAP.

Constant current stimulation (CCS) is used mainly because of its advantages in better control of the amount of charge transferred during stimulation, high calibration accuracy, and better stimulation efficiency. It is also believed that the CCS provides a constant charge regardless of the impedance change at the electrode-tissue interface. For a current source, a 5-bit binary-weighted current steering DAC delivers up to 100 μA of stable current to each output stage. Bandgap voltage reference circuit provides stable bias voltage to DAC, delivering 2.2 μA. The summed current of the 5-stage DAC is transmitted to the biphasic pulse generator through the current mirror. Generally, the current source-sink structure could be vulnerable to changes in output load due to the reduced voltage swing in half. In this system, the output voltage swing was maximized by switching the bias of the reference electrode in the bipolar-type stimulus structure. Also, the output stage of the current source-sink design increases the output impedance by adding feedback to the regulated cascoded current mirror, as shown in Figure 4.4.

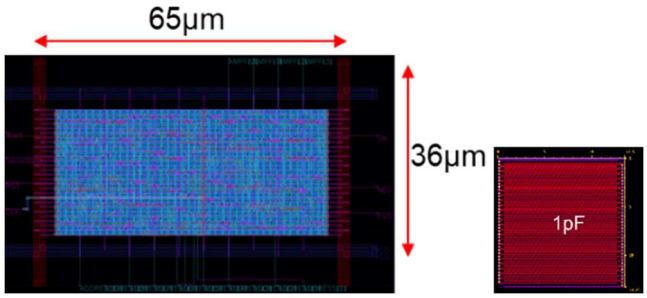

Figure 4. 3. Layout and size comparison of the digital logic circuit and VNAP for 1 pF

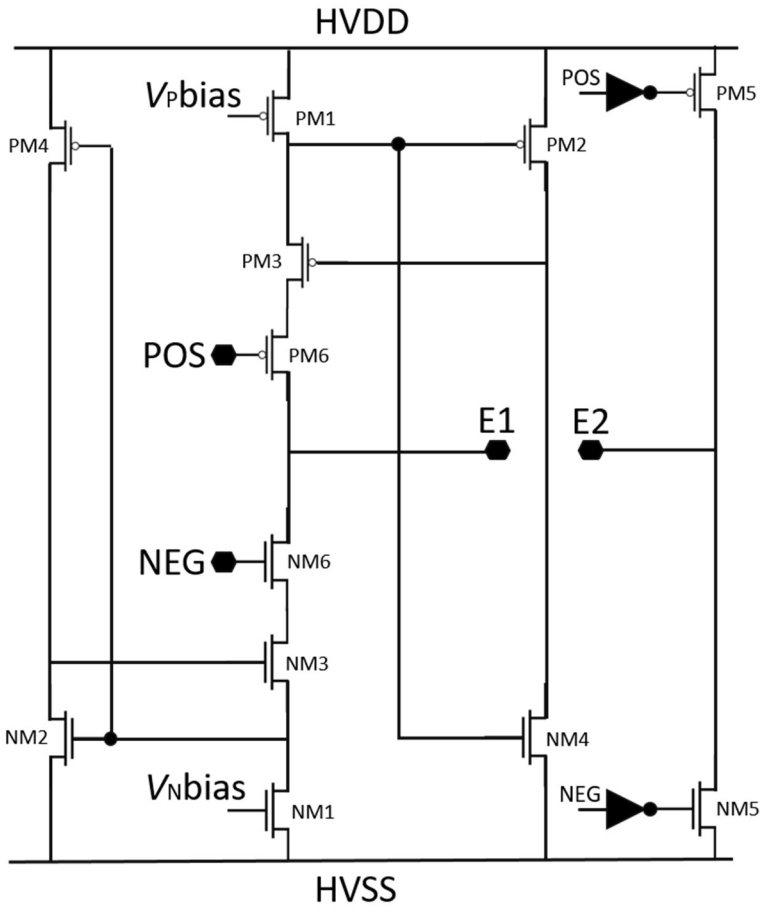

Figure 4. 4. Schematic of CCS

When power is transmitted through the off-chip coil antenna, it is rectified by a rectifier, and stable power is supplied through the regulator [118], [119]. The rectifier is designed in a mixed structure with the charge pump, and when 0 dBm is received, the entire system is stably driven [94], [120]. The regulator is designed as capacitor-less[121], [122], and the required load-end capacitance is about 70 pF. The regulator supplies 1.8 V and is designed to withstand up to about 1.5 mA.

When power is transmitted through the chip coil antenna, it is rectified by a rectifier, and stable power is supplied through the regulator [14-16]. The rectifier is designed in a composite structure with the charge pump, and when 0 dBm is received, the entire system is stably driven. The regulator is designed as capacitor-less, and the required load-end capacitance is about 70 pF (Figure 4.5). The regulator is supplied with 1.8 V and is designed to withstand up to about 1.5 mA.

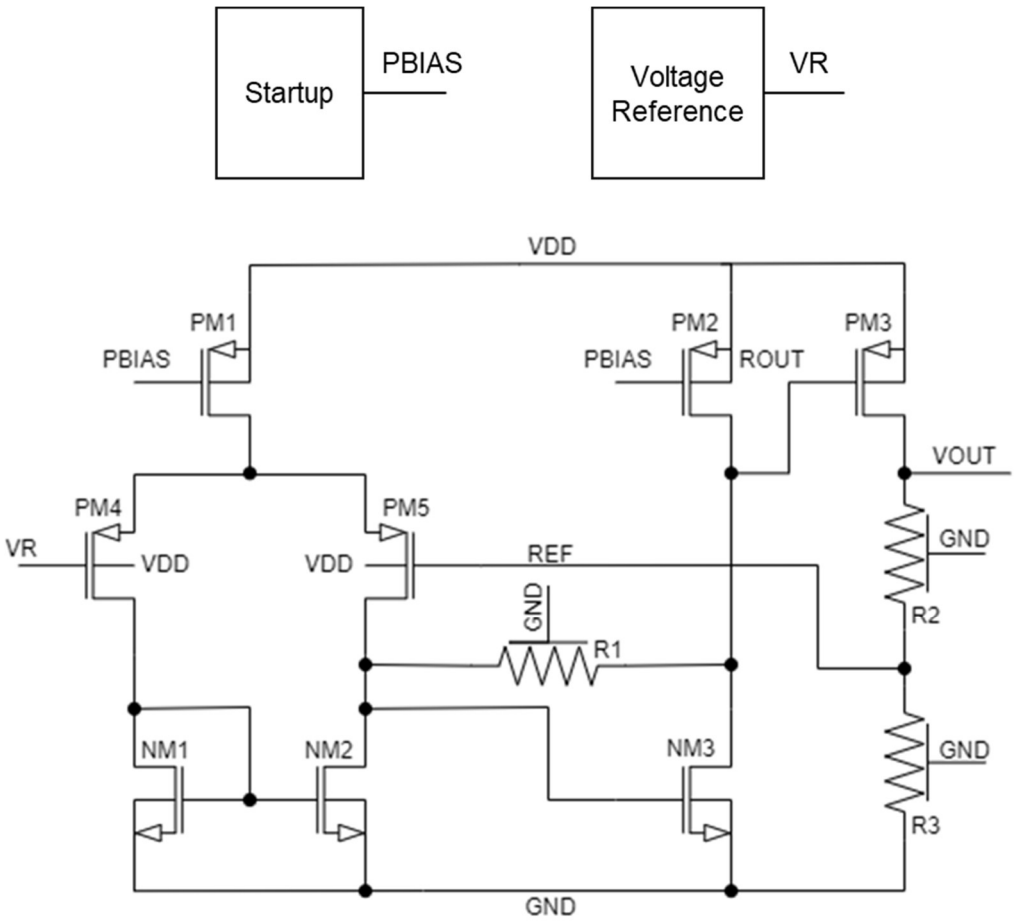

Figure 4. 5 . Schematic of the capacitor-less regulator

A system in which the substrate is separated is synchronized with a reset signal. Therefore, a module that generates a reset signal by sensing the amount of power received wirelessly is designed in the manufactured system. When power is received from the outside, and the power is momentarily strong, a reset signal is generated, and all digital blocks are initialized. This method synchronizes all systems by adjusting the amount of externally applied power even if the board is separated [123]. The power sensing module consists of an envelope detector; when the power is increased, a high signal is transmitted through the inverter. The simulation confirmed that the system operates stably when the power of 0 dBm is transmitted to the rectifier. The reset signal is generated when about 4 dBm or more power is transmitted.

Data demodulation used for serial commands is amplitude shift keying (ASK) [124]–[126], which transmits digital data as variations in the amplitude of a carrier wave. Low voltage CS amplifier and additional gain stages amplify input signal through the coil. Data buffer after the ASK demodulator to help the serial data to reach digital logic without a loss (Figure 4.6). The comparator shown in Figure 4.7 converts the analog input signals into a digital bitstream with a 500 mV threshold. Although the circuits are conventional architecture, scaling down to 28 nm creates design issues. Additional guard rings and a symmetrical layout enhance the performance. However, routing and impedance-matching techniques are essential.

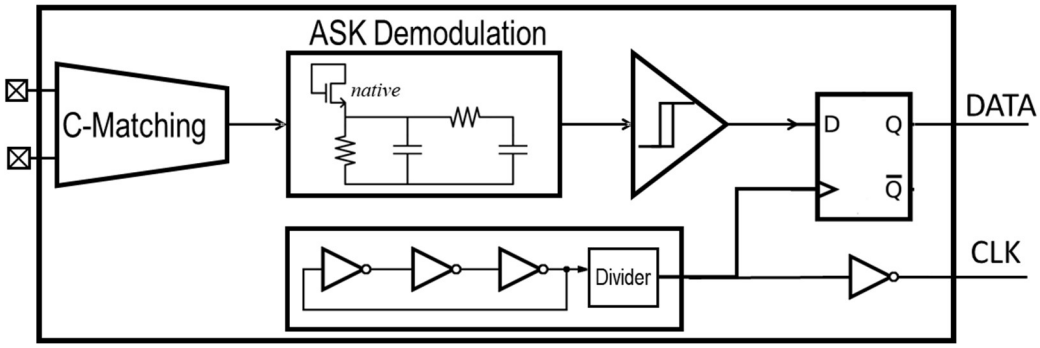

Figure 4. 6. Noncoherent receiver with ASK demodulation circuit

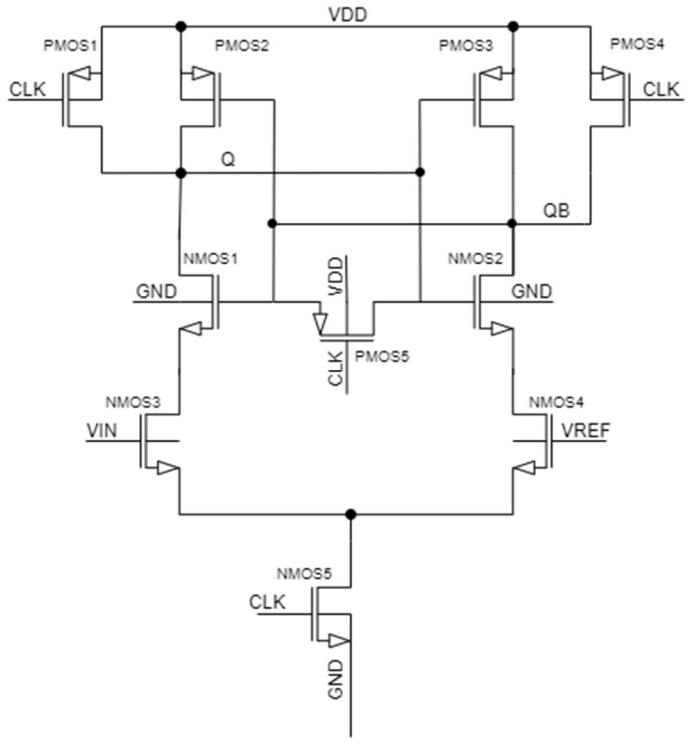

Figure 4. 7. Schematic of the comparator used in the ASK demodulation circuit

- *Multichannel microstimulator in 180 nm RFCMOS process*

The structure of the antenna coil was designed and simulated using ANSYS HFSS. Additional antenna efficiency, resonant frequency matching, and matching circuits were verified by Cadence Design Simulator using simulation data extracted from HFSS. In Figure. 4.8, The simulation model is a silicon-based chip of 1 mm × 1 mm, designed to implement the dielectric property of substrate silicon, an oxide layer, a polysilicon layer, and metal layers. The in-vivo dielectric condition of multi-layer tissue was constructed 1 mm skin, 0.14 mm fat, 7 mm skull, 0.5 mm dura, 0.2 mm cerebrospinal fluid (CSF), and 81 mm Greymatter assuming the relay coil is inserted in CSF. The size of the on-chip coil is chosen to maximize coil efficiency and utilization of the area within the 1 mm × 1 mm boundary. 2 turn coil structure was selected to secure inside the CMOS fabrication area. The width and spacing of the metal were swept to maximize coil efficiency under 915 MHz transmission frequency. The 915 MHz frequency of transmission RF signal was selected to withstand tissue absorption while providing enough powering through mm-sized coils. The on-chip coil was fabricated with Metal 6 in TSMC 180 nm RFCMOS process

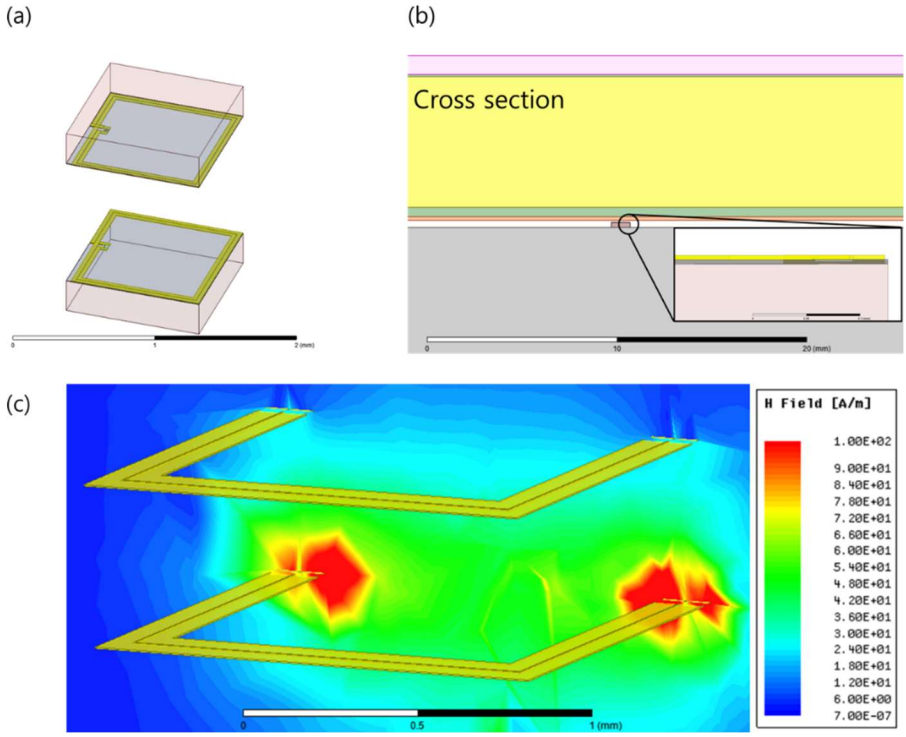

Figure 4. 8. HFSS simulation. (a) 3D modeling of 1 mm × 1 mm on-chip coil facing toward each other, (b) cross-section of chip mounted inside the head with upper layers, (c) magnetic field simulation result

In a multi-node distributed system with a separate substrate, there are only four pads in total: an active electrode, a reference electrode, and a VDD and ground pad. Dual VDD and ground pad are designed to be cut later when the address code and channel are designated. An antenna is required to receive power. We designed a chip coil antenna (Figure 4.9) with a top metal thickness of 2 μm among the metals provided in the library. The chip coil antenna was designed using HFSS from Ansys, an electromagnetic field analysis tool, and it was confirmed that it had an inductance of 8 nH and a quality factor of 5 at 900 MHz. The width of the coil is 35 μm, and the space between the coils and the metal is 15 μm. A capacitor is connected so that it can resonate at 900 MHz according to the inductance of the chip coil antenna.

From the ISM band frequency, the suitable frequency for wireless data transmission of the recording and the stimulating module is decided considering the size of the system and penetration depth of field interacting between the inner and outer devices. 915 MHz frequency seems appropriate for their antenna size and 4 cm depth.

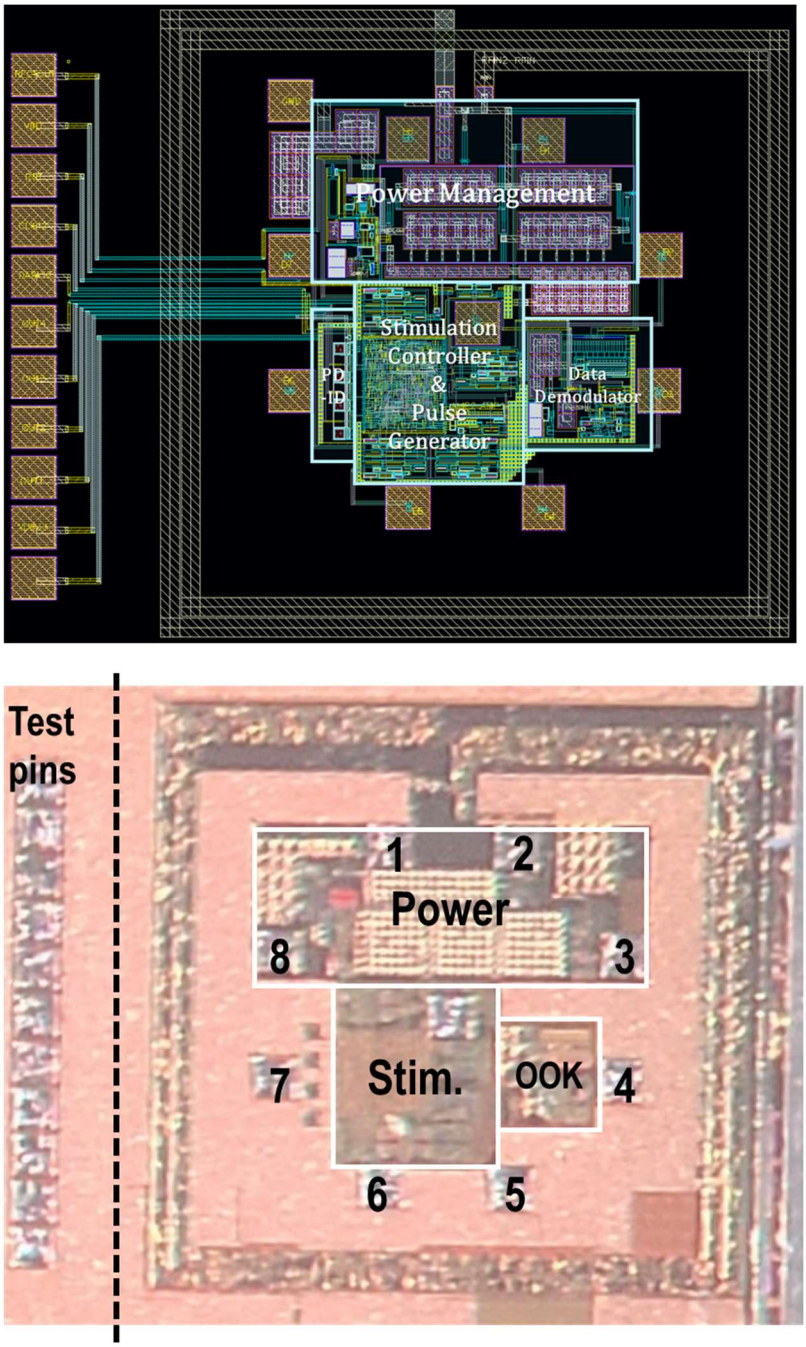

Figure 4. 9. Eight-channel microstimulator layout (top) and microphotograph (bottom)

A 2-stage bridge rectifier with 5 pF charging capacitors and a capless LDO regulator modulates the power management circuit's 900-915 MHz carrier frequency. With a 3 dBm input power, the rectifier generates a 1.6 V dc voltage. The capless regulator is turned on when the designed rectifier receives sufficient power. The regulator supplies a stable supply voltage to the stimulation IC and the spike recording IC. The regulator consists of a conventional PASS transistor, an error amplifier, a start-up circuit, and a reference voltage generator. The overall target gain is over 80 dB, and the phase margin is 60°.

An envelope detection circuit with additional passive LPF is implemented for the downlink communication in stimulation IC. The ASK demodulation circuit with a 915 MHz carrier frequency sends the demodulated signal to a comparator. Also, the internal ring oscillator provides the clock to the comparator and digital logic, lowering the bit error rate. The demodulated binary signal works as the clock synchronization input to the digital logic circuit. There are several counters and registers in digital logic for generating a sequential switching signal passed to an analog switch that provides a programmable stimulation pulse. Also, it controls the current amplitude using an on-chip 4-bit DAC, generates timing signals for the pulse width and frequency, and sets the current direction using the switch at the biphasic pulse generator.

Pads of the 8-channel active electrode are arranged in a regular hexagonal structure with the reference pad placed in the center. The electrode arrangement in the regular hexagonal shape can precisely designate the location of the

stimulus according to the channel selection, and it is possible to predict the amount of charge reaching the target with high precision by calculating the amount of reduction in current diffusion in the electrolyte.

4.3. Experimental Methods

4.3.1. Optic setup with lasers

The figures below are experimental setups for PD measurement and anti-fuse post-processing. In Figure 4.10(a), I-V characteristics were confirmed using a source meter controlled by LabVIEW after the laser light passed through the microscope. M is the mirror, and BS stands for a beam splitter. As the green laser is a 100 mW 520 nm solid-state laser, the experimental setup is as in Figure 4.10(b).

For the laser-guided PD, we measured the I-V characteristics using a source meter according to the laser power applied to the PD. Considering the absorption band of the photodiode, we used a laser with a wavelength of 520 nm. The position of the PD was confirmed using an illumination lamp then a laser beam was projected onto a PD connected to the source meter. Herein, to observe PD effectively, it was confirmed by attaching a ×20 objective lens to the microscope.

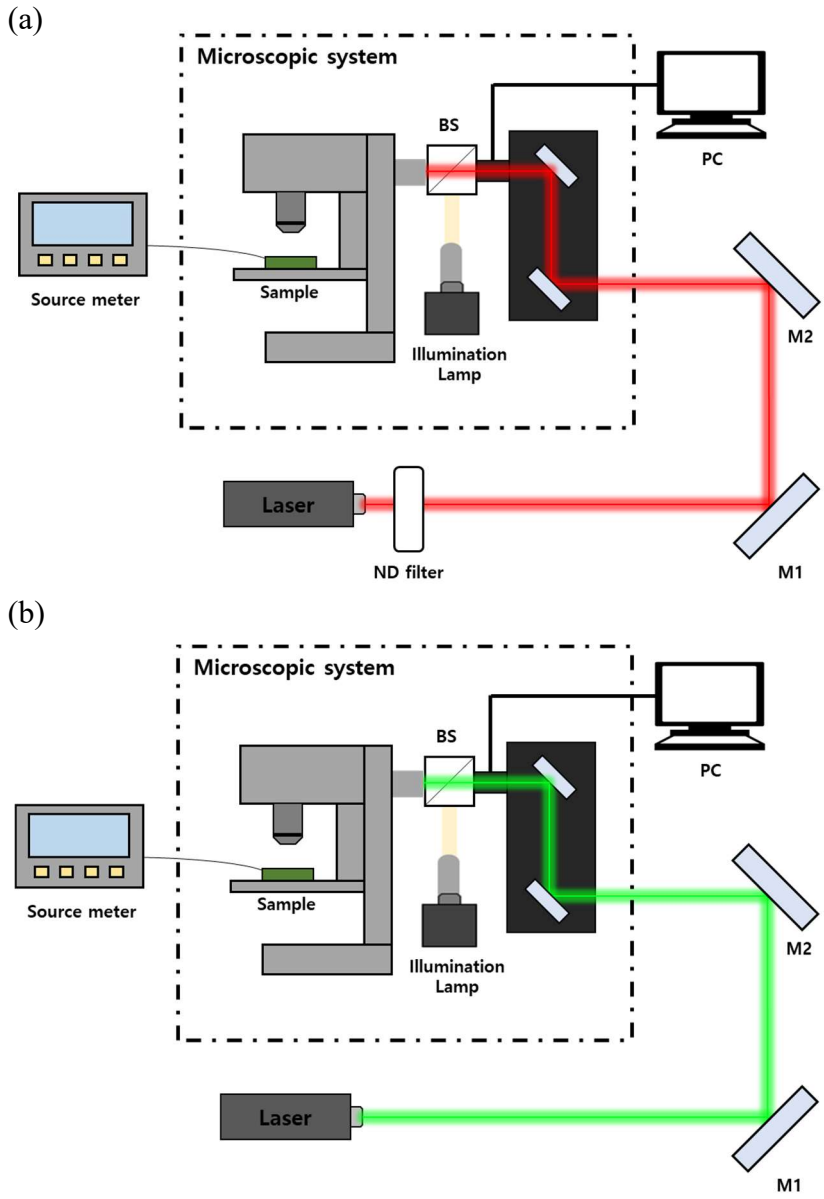

Figure 4. 10. Optical setup: (a) 473 nm 5 mW Red Laser. Laser wavelength: 473 nm. (b) 520 nm 100 mW Solid State Laser (Green Semiconductor Laser)

4.4. Results

4.4.1. Photodiode characterization

We used four lasers in different wavelengths to know the layer characteristics of TSMC 180 nm standard technology (laser information corresponding to the wavelength is shown in Appendix 1). The layer information's silicon absorption rate can be found in Appendix 2, considering the light spectrum. The measurement result of the photodiode and anti-fuse id array from the TSMC 180 nm process is provided.

The results indicated that the green laser was adequate for the fabricated photodiode. Figure 4.11 (a) graph shows the photodiode I-V curve measured with different light sources. With the same emission power of 5 mW, the green laser reached the polysilicon layer of the photodiode. The instant response time of the photodiode reduces the time the system has to withstand large breakdown currents. An average of 42 μA current was generated.

We conducted focusing on multi-array for simultaneous irradiation. Although we focused the laser on the photodiode through the camera during the experiment, tight focus on the diffusion region was hard. Also, the microscope and mirror degenerated the input power to the photodiode. However, it was sufficient to turn on the diode.

Photocurrents generated from laser input with different focuses and distances from the photodiode are depicted in the graph in Figure 4.11 (b). Figure 4.11 (c) shows the beam size of a 473 nm red laser. Since the microscope's focus may miss the focus of the photodiode, a photomicrograph

was taken at the position where the photocurrent is maximized for comparison. As shown in Figure 4.12, the SEM image has shown the layer information of standard CMOS technology. The measured result indicated that the diffusion layer is around the n+ doped guard ring.

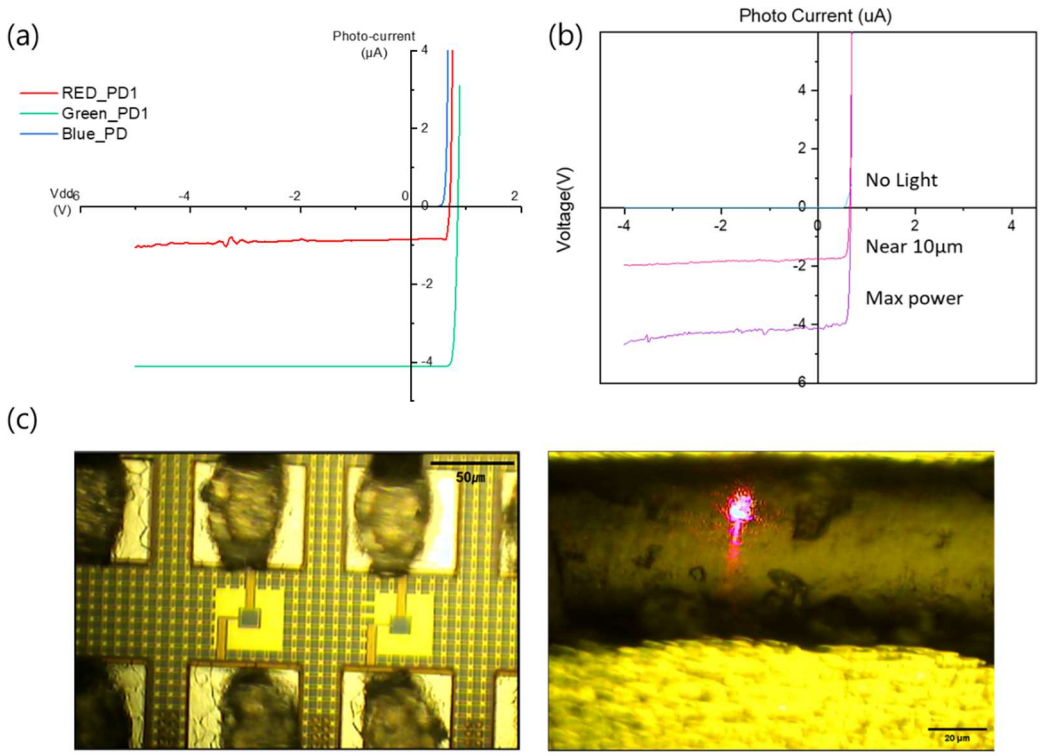

Figure 4. 11. I-V curve of (a) different light sources applied to the photodiode, (b) different focus and distance from the photodiode. (c) Microphotograph of photodiode (PD) array and beam size

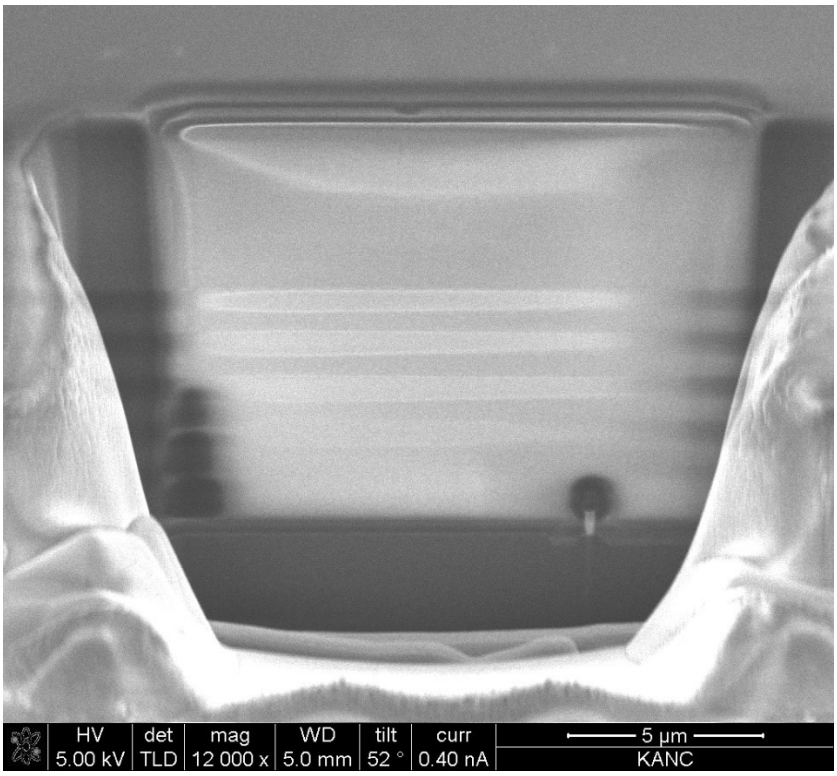

Figure 4. 12. SEM image of PD layer

We conducted FIB (Focused Ion Beam) SEM with our fabricated photodiode. The silicon substrate was placed under 10µm from the top seal layer based on the length and milling time.

4.4.2. Gate anti-fuse characterization

The diode-based gate oxide anti-fuse cell works similarly to the one-time programmable (OTP) memory cell. ID generation cannot be undone when the array is encoded through breakdown. The breakdown voltage depends on the thickness of the gate oxide. The anti-fuse ID array's programming needs a higher voltage, much larger than I/O cells. Thus, we used a thin oxide low-voltage cell for the anti-fuse and thick gate oxide high-voltage cell for the readout circuit. I-V characteristics of the anti-fuse with and without laser irradiation are shown in Figure 4.13. The anti-fuse memory cell is broken down at 4.8 V with 1 mA current compliance.

The resistance variation of the anti-fuse array was measured using different types of transistors. The average resistance of 1.8 V standard cell NMOS is 12 kΩ while 3.3 V standard cell exhibited 23 kΩ. after the breakdown, the resistance decreased instantly.

.

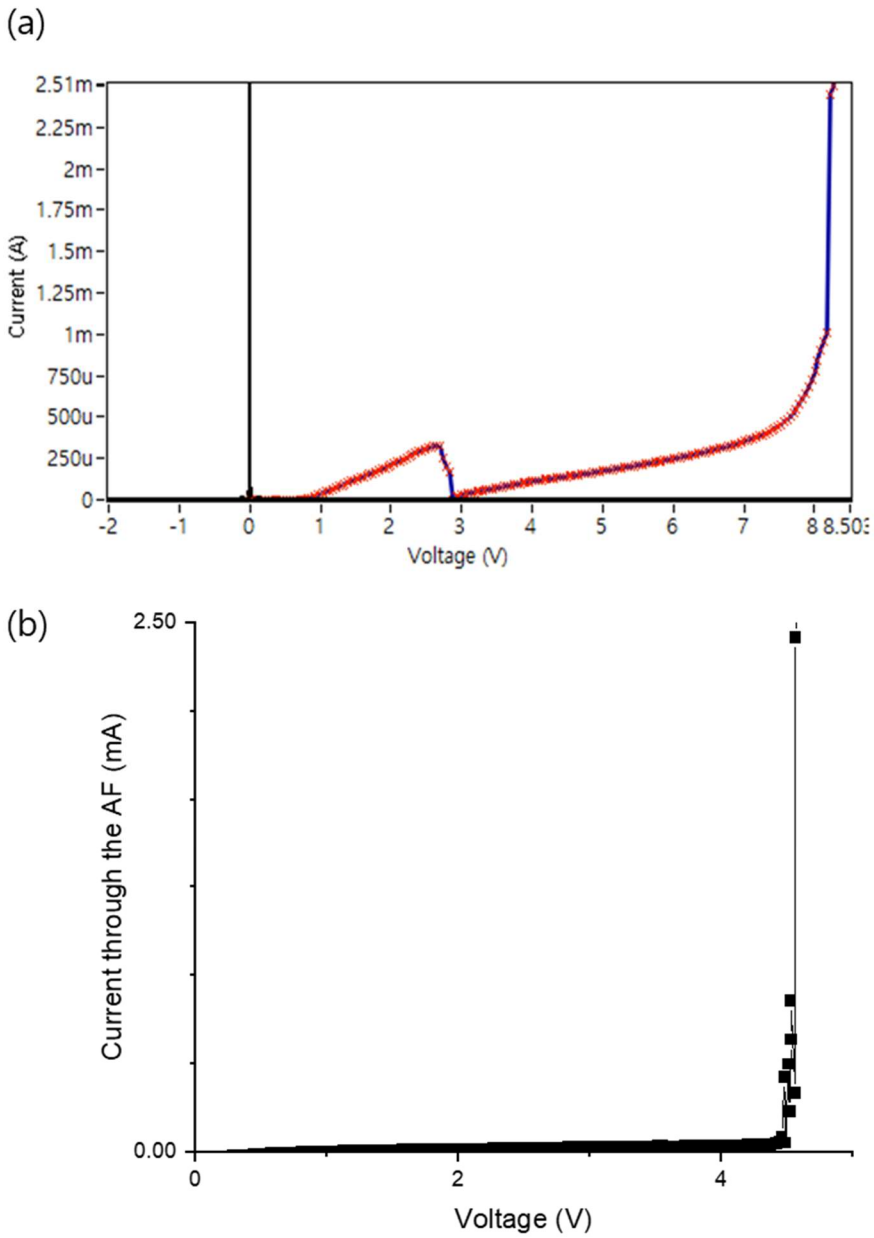

Figure 4. 13. I-V curve (a) Double breakdown due to the leakage current (b) Breakdown with photodiode signal

4.4.3. Microstimulator measurement result

The concept of this system is that the expandable module communicates with an external controller with an individual address. Flexible manipulation is possible, and interference between systems can be reduced by freely arranging the recording module and the stimulation module to a desired location to form a bidirectional neural interface. Spike detection, used in a recorder, preprocessed and transmitted the neural data to the outside. Thanks to this, the amount of data the external network controller handles is relatively reduced, freeing the system from tight data handling.

The block diagram of the designed distributed neural interface (Figure 4.14) and microphotograph of the microstimulator (Figure 4.15) depict the final system. The independent implants have an integrated core operation circuit, wireless data transmission/reception circuit, and power supply circuit. Each implant has an ID generation circuit of anti-fuse-based PD-ID (Photodiode-ID). Network controller (NC) provides bidirectional communication through RF signal.

In wireless power transceivers, insufficient power is received by the implant because of their on-chip antenna size and scattering. Bypass and charging capacitors are the main components that help stabilize the power supply. The experimental result indicated that a 10 nF charging capacitor is sufficient to endure burst stimulation.

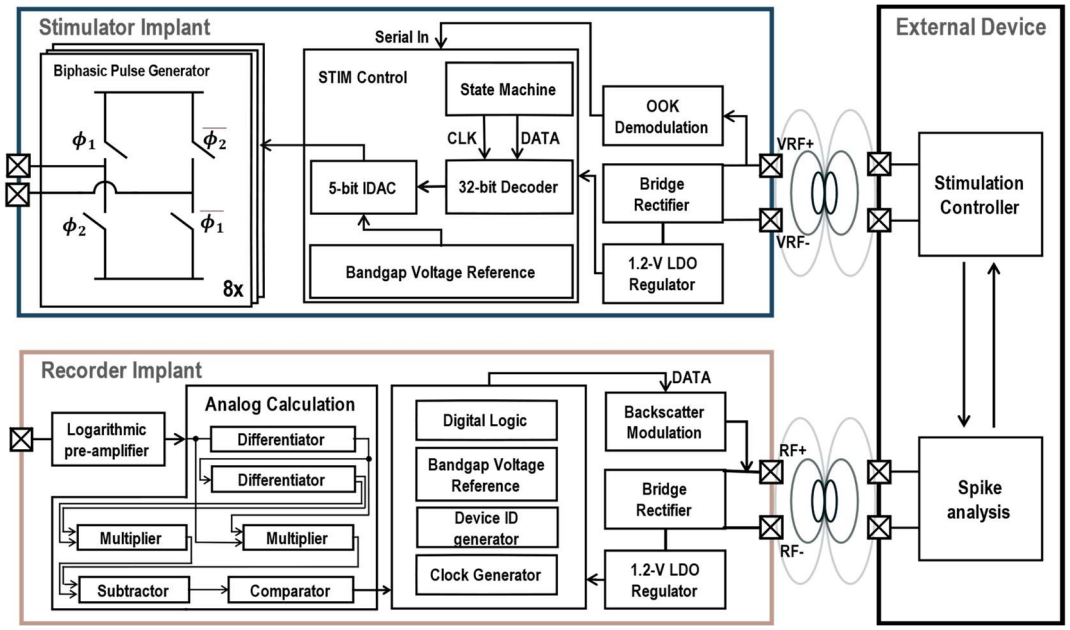

Figure 4. 14. Block diagram of wireless microstimulator and micro-recorder composing distributed neural interface. There is no on-chip coil in 28 nm technology

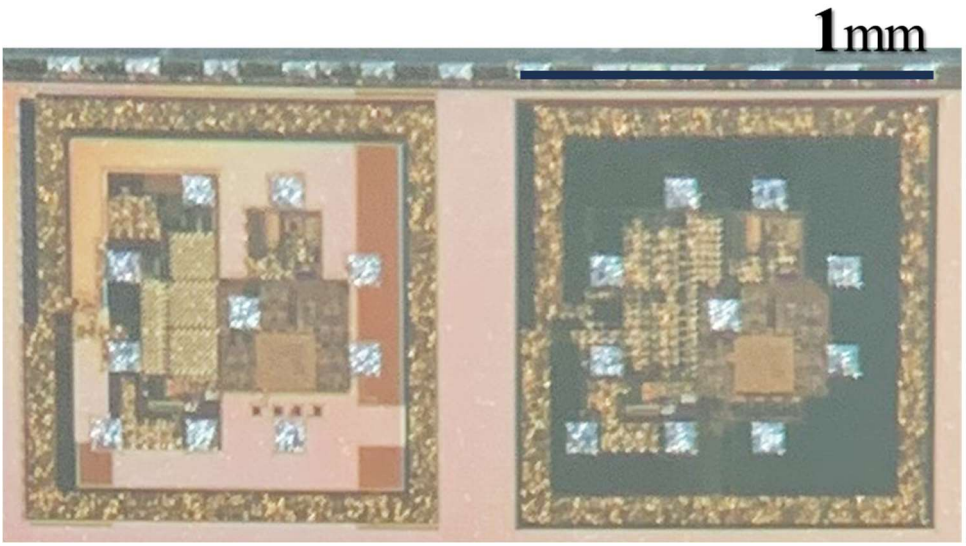

Figure 4. 15. Microphotograph of fabricated IC

Stimulation voltage is measured between the active electrode and the reference electrode placed in the PBS 1× solution. The resistance of the electrode was 8-11 kΩ. The interphase delay between the cathodic and anodic phases is optional. As shown in Figure 4.16, stimulation frequency have a discrete stage according to the universal clock. For example, if the fastest clock is determined to be 20 kHz, the maximum excitation frequency is 1 kHz.

The ASK demodulation circuit detects amplitude change up to 50% of the original RF signal. Noncoherent data receiver uses a ring oscillator to synchronize and regenerate clock signal. 12.8 MHz ring oscillator is connected to the clock divider to earn a 1 MHz clock signal. Based on the regenerated clock data demodulation with envelope detection circuit and comparator recovers transmitted data.

Figure 4.17 and Figure 4.18 show the RF signal demodulation with the OOK demodulator. The result indicates that a low pass filter reduces the amplitude of PREDATA. However, it is sufficient for demodulation because the comparator got 320 mV as the reference voltage below the PREDATA. The system clock of 1.07 MHz was divided from a 12 MHz ring oscillator, and an additional D-Flip-flop synchronized the DATA and CLK.

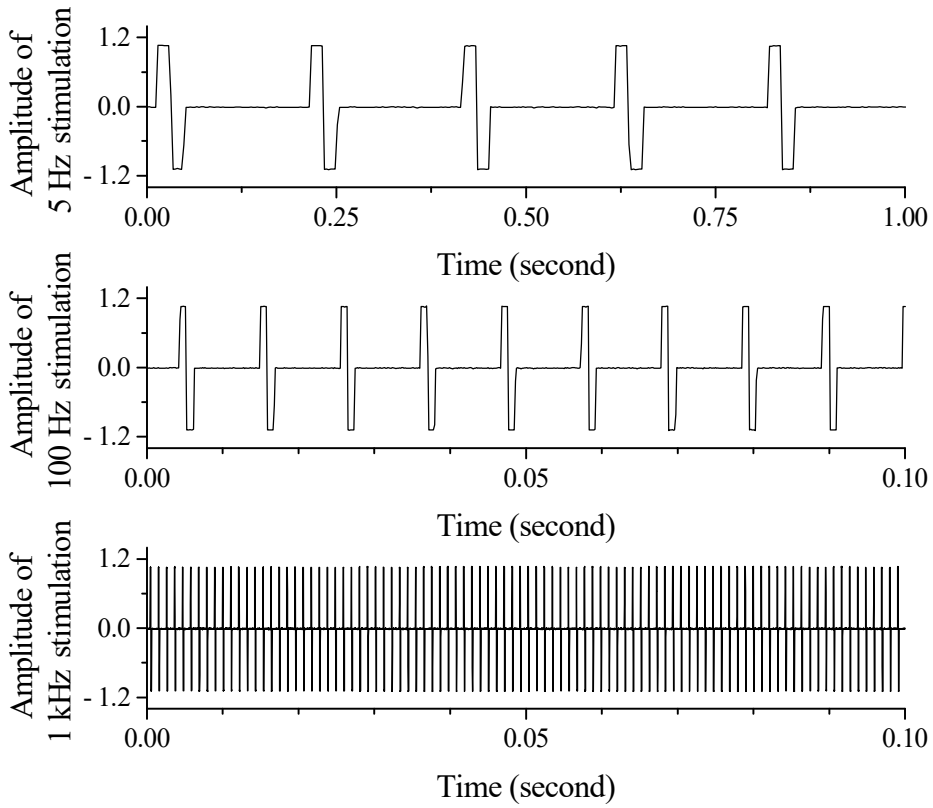

Figure 4. 16. Frequency modulation of stimulus in PBS solution

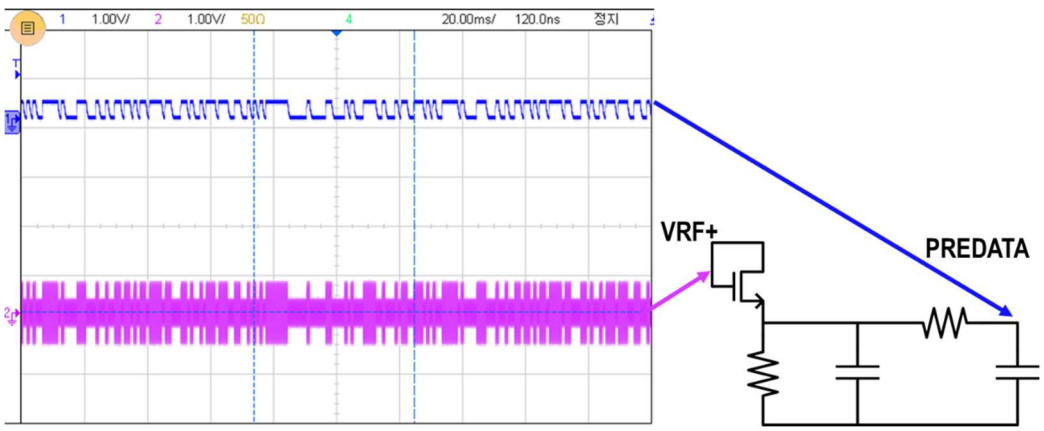

Figure 4. 17. Signal measured at each demodulation point

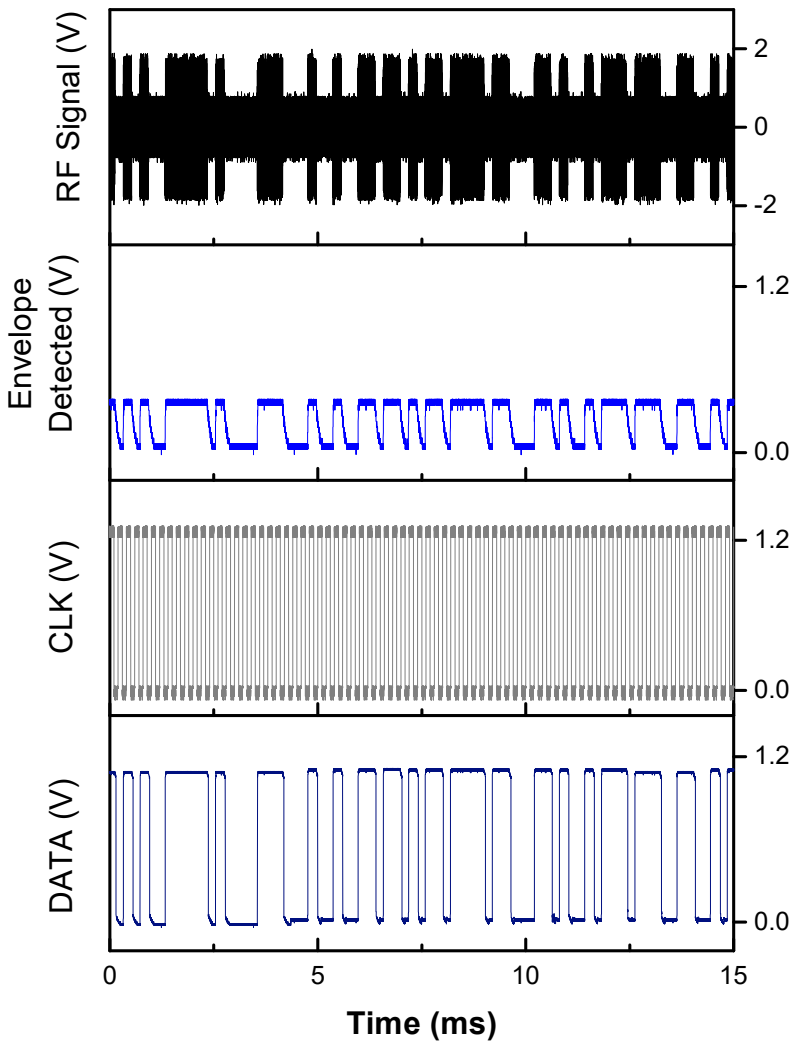

Figure 4. 18. ASK demodulation signal process

RF signal detected at the on-chip coil antenna was a 2 V_{pp} sinusoidal wave. After the envelope detection, a low pass filter used to remove the ripple attenuated the signal. Serial data was synchronized with a clock signal by D-flipflop.

4.5. Summary

A diode-based gate oxide anti-fuse memory array without an additional I/O pad and the functionality of the array is confirmed by measuring the results of the circuit design fabricated in a 180 nm standard CMOS process.

The proposed structure of the anti-fuse array coupled with the photodiode has an anti-fuse designed to be broken even at a relatively low voltage and a photodiode that serves as a voltage switch. It is necessary to test the performance of the structure. Thus the photodiode's structure was first analyzed. In the case of the standard CMOS process, all information on the process layer and doping level is not disclosed, so it was inferred based on the experimental results. When comparing the SEM images taken with the output values of the photocurrent using the four lasers, it was confirmed that the silicon substrate started from below 10 μm. Then it was confirmed that a deep n-well exists at a depth three times that of the N-well.

Based on the information on the photodiode and anti-fuse characteristics obtained earlier, an addressable OTP structure was created. Through this, it was possible to cause a breakdown with a voltage of 4.8 V when there was a photodiode. Also, it was confirmed that the shorter the voltage applied over time, the smaller the range of influence on the surrounding circuit. In addition, the ground separation method using ESD was applied to the layout to prevent leakage current from being concentrated in other circuits.

Next, a microstimulator for a distributed system to be combined with the addressing circuit was fabricated. Each stimulation module using the two

processes has the same central circuit but exhibits several different characteristics. After checking the operation of the core circuit, the wireless power transmission and data communication were verified. Data communication using the ASK method allows fast detection by increasing the conversion threshold even when the power transmission efficiency of the micro-antenna is low. This was confirmed by using an external coil resonating at 900 MHz. Details are summarized in the table below.

Chapter 5. Conclusion

5.1. Thesis Summary

Applying the bidirectional neural interface to humans is challenging because the electronic device must be inserted into the body without a sense of heterogeneity and harmonized with the natural neural circuit. The brain receives and processes complex signals and interacts with the outside world. Currently, the implant system that records, analyzes, and gives feedback as stimulation needs to record and analyze numerous nerve signals to replace them. Also, when electrical stimulation is given to the brain to recognize it as a naturally occurring nerve signal, different nerve cells must continuously produce various signals.

This study presents a detailed method of developing a wireless programmable microstimulator with low power and high stimulation efficiency. The core of this method contains a circuit design method to ensure system operation even at low power due to implant size scaling and parameter optimization for high-efficiency stimulation. The digital stage, which accounts for the majority of power consumption, and the data communication that enables a stable power supply are dominant considerations for reducing the power consumption of microstimulators. The optimized implant was designed by analyzing the threshold and response range of target neurons through electrophysiology experiments in regular neural networks.

Various applications of neural prostheses were attempted with the fabricated device. Low power microstimulator for retinal prosthesis was

optimized according to an ex vivo experiment of WT and rd1 mouse retina. Next, a multichannel stimulator as bidirectional BMI was integrated into IC with a recorder and wireless telemetry. Backscatter and DPSK communication with a single coil antenna has shown that power efficiency can be increased, energy consumption can be reduced, and the system can be compact.

Finally, this study proposed a new ID generation method for a distributed system along with wireless microstimulator design and fabrication. We have analyzed the characteristics of photodiodes and gate oxide anti-fuse cells in the standard CMOS process. Photodiode connected to the anti-fuse forms OTP array using 30 μm × 30μm area.

5.2. Future Directions

Implantable neural interface systems continue evolving toward more intelligent, multi-modal, high-performance solutions and closed-loop operation. Thus, the designs must deal with increased channel count, minimal invasiveness, longevity, and scalability. The large amount of neural data collected from multiple channels burdens external and internal modules that transmit, receive, and process them. Even if preprocessed data is sent within the implant, there is a burden in bi-directional communication. Additionally, to minimize invasiveness and increase implant longevity, both size and power consumption must be optimized in system design, manufacturing, and integration. Miniaturization combined with a high level of integration and wireless power/data transfer enables high-performance interfacing with the

nervous system. Therefore, the added complexity is that you must meet all these requirements without sacrificing performance.

Implantable ASICs record weak biological signals with fidelity, stimulate neural activity, and extract critical biological features under stringent power and size constraints. Additionally, incorporating machine learning with a high number of recording and stimulation channels enables new treatment techniques to restore health from chronic pain or other disorders without the side effects of drugs. For example, small programmable low-power stimulators open various applications for the central and peripheral nervous systems.

As such, the miniaturization of neural interface implants has become a natural trend. Thus, a low-power, the high-efficiency multifunctional integrated system has become a goal to be reached. Looking at the research results, we have researched a distributed system to give scalability to the existing centralized system and remove the limit on the number of channels. To reduce the size of the system, the unnecessarily wasted area was minimized, and a structure was devised to increase the number of channels with simple post-processing using optimized modules. In addition, research has been conducted to drastically reduce power consumption and size using a highly integrated CMOS process, such as 28nm.

Based on the results of several studies, the development of microstimulators should consider two aspects. The development of microstimulator needs to consider two aspects. First, as the system size shrinks, the average power received and the capacity of power in the system reduces. Since the stimulator uses sudden power consumption, which intrigues unstable

power sources, energy regeneration and storage are essential to implantable systems. Furthermore, unlike a recorder that records and observes the action potential of a nerve cell from the side, a stimulator must respond flexibly to stimulation. From a clinical point of view, different stimulation methods are used depending on the patient and the target organ. For this, calibration and optimization must be performed to achieve effective stimulation. System research and development flow is moving toward fully implantable micro-devices, and smooth communication between interfaces is essential. An effective communication method considering the internal environment and conditions, including the electromagnetic communication method, determines whether or not it would succeed as a stimulation device.

References

[1] P. C. Loizou, “Introduction to cochlear implants,” *IEEE Eng. Med. Biol. Mag.*, vol. 18, no. 1, pp. 32–42, 1999, doi: 10.1007/978-3-319-69743-7_4.

[2] B. S. Wilson and M. F. Dorman, “The surprising performance of present-day cochlear implants,” *IEEE Trans. Biomed. Eng.*, vol. 54, no. 6, pp. 969–972, 2007, doi: 10.1109/TBME.2007.893505.

[3] M. A. Lebedev and M. A. L. Nicolelis, “Toward a whole-body neuroprosthetic,” in *Progress in Brain Research*, vol. 194, 2011, pp. 47–60. doi: 10.1016/B978-0-444-53815-4.00018-2.

[4] X. Liu *et al.*, “A wireless neuroprosthetic for augmenting perception through modulated electrical stimulation of somatosensory cortex,” *Proc. - IEEE Int. Symp. Circuits Syst.*, pp. 2–5, 2017, doi: 10.1109/ISCAS.2017.8050364.

[5] C. Pandarinath and S. J. Bensmaia, “The science and engineering behind sensitized brain-controlled bionic hands,” *Physiol. Rev.*, vol. 102, no. 2, pp. 551–604, 2022, doi: 10.1152/physrev.00034.2020.

[6] S. Miocinovic, S. Somayajula, S. Chitnis, and J. L. Vitek, “History, applications, and mechanisms of deep brain stimulation,” *JAMA Neurol.*, vol. 70, no. 2, pp. 163–171, 2013, doi: 10.1001/2013.jamaneurol.45.

[7] J. Jankovic, “Medical treatment of dystonia,” *Mov. Disord.*, vol. 28, no. 7, pp. 1001–1012, 2013, doi: 10.1002/mds.25552.

[8] G. A. Worrell, “Electrical Brain Stimulation for Epilepsy and Emerging Applications,” *J. Clin. Neurophysiol.*, vol. 38, no. 6, pp. 471–477, 2021, doi: 10.1097/WNP.0000000000000819.

[9] S. F. Cogan, K. A. Ludwig, C. G. Welle, and P. Takmakov, “Tissue damage thresholds during therapeutic electrical stimulation,” *J. Neural Eng.*, vol. 13, no. 2, 2016, doi: 10.1088/1741-2560/13/2/021001.

[10] H. Yuk, B. Lu, and X. Zhao, “Hydrogel bioelectronics,” *Chem. Soc. Rev.*, vol. 48, no. 6, pp. 1642–1667, 2019, doi: 10.1039/c8cs00595h.

[11] S. Washburn, R. Catlin, K. Bethel, and B. Canlas, “Patient-perceived differences between constant current and constant voltage spinal cord stimulation systems,” *Neuromodulation*, vol. 17, no. 1, pp. 28–36, 2014, doi: 10.1111/ner.12085.

[12] D. S. Kern, A. Fasano, J. A. Thompson, A. Abosch, S. Ojemann, and R. P. Munhoz, “Constant Current versus Constant Voltage: Clinical Evidence Supporting a Fundamental Difference in the Modalities,” *Stereotact. Funct. Neurosurg.*, vol. 99, no. 2, pp. 171–175, 2021, doi:

10.1159/000510803.

[13] D. A. Wagenaar, J. Pine, and S. M. Potter, “Effective parameters for stimulation of dissociated cultures using multi-electrode arrays,” *J. Neurosci. Methods*, vol. 138, no. 1–2, pp. 27–37, 2004, doi: 10.1016/j.jneumeth.2004.03.005.

[14] D. Boinagrov, J. Loudin, and D. Palanker, “Strength-duration relationship for extracellular neural stimulation: Numerical and analytical models,” *J. Neurophysiol.*, vol. 104, no. 4, pp. 2236–2248, 2010, doi: 10.1152/jn.00343.2010.

[15] D. B. Koch, M. Downing, M. J. Osberger, L. Litvak, and S. Greco, “Using current steering to increase spectral resolution in CII and HiRes 90K users,” *Ear Hear.*, vol. 28, no. SUPPL.2, pp. 38–41, 2007, doi: 10.1097/AUD.0b013e31803150de.

[16] A. G. Srinivasan, R. V. Shannon, and D. M. Landsberger, “Improving virtual channel discrimination in a multi-channel context,” *Hear. Res.*, vol. 286, no. 1–2, pp. 19–29, 2012, doi: 10.1016/j.heares.2012.02.011.

[17] W. Nogueira, L. Litvak, B. Edler, J. Ostermann, and A. Büchner, “Signal processing strategies for cochlear implants using current steering,” *EURASIP J. Adv. Signal Process.*, vol. 2009, 2009, doi: 10.1155/2009/531213.

[18] G. Dumm, J. B. Fallon, C. E. Williams, and M. N. Shivdasani, “Virtual electrodes by current steering in retinal prostheses,” *Investig. Ophthalmol. Vis. Sci.*, vol. 55, no. 12, pp. 8077–8085, 2014, doi: 10.1167/iovs.14-15391.

[19] Y. T. Wong, S. C. Chen, J. M. Seo, J. W. Morley, N. H. Lovell, and G. J. Suaning, “Focal activation of the feline retina via a suprachoroidal electrode array,” *Vision Res.*, vol. 49, no. 8, pp. 825–833, 2009, doi: 10.1016/j.visres.2009.02.018.

[20] C. C. Hsieh and M. D. Ker, “Monopolar Biphasic Stimulator with Discharge Function and Negative Level Shifter for Neuromodulation SoC Integration in Low-Voltage CMOS Process,” *IEEE Trans. Biomed. Circuits Syst.*, vol. 15, no. 3, pp. 568–579, 2021, doi: 10.1109/TBCAS.2021.3087036.

[21] J. Y. Son and H. K. Cha, “An Implantable Neural Stimulator IC with Anodic Current Pulse Modulation Based Active Charge Balancing,” *IEEE Access*, vol. 8, pp. 136449–136458, 2020, doi: 10.1109/ACCESS.2020.3012028.

[22] Z. Luo and M. D. Ker, “A High-Voltage-Tolerant and Power-Efficient Stimulator with Adaptive Power Supply Realized in Low-Voltage CMOS Process for Implantable Biomedical Applications,” *IEEE J. Emerg. Sel. Top. Circuits Syst.*, vol. 8, no. 2, pp. 178–186, 2018, doi:

10.1109/JETCAS.2018.2796381.

[23] W. Y. Hsu and A. Schmid, “Compact, Energy-Efficient High-Frequency Switched Capacitor Neural Stimulator with Active Charge Balancing,” *IEEE Trans. Biomed. Circuits Syst.*, vol. 11, no. 4, pp. 878–888, 2017, doi: 10.1109/TBCAS.2017.2694144.

[24] B. Lee *et al.*, “An Inductively-Powered Wireless Neural Recording and Stimulation System for Freely-Behaving Animals,” *IEEE Trans. Biomed. Circuits Syst.*, vol. 13, no. 2, pp. 413–424, 2019, doi: 10.1109/TBCAS.2019.2891303.

[25] G. S. Stickney, F.-G. Zeng, R. Litovsky, and P. Assmann, “Cochlear implant speech recognition with speech maskers,” *J. Acoust. Soc. Am.*, vol. 116, no. 2, pp. 1081–1091, 2004, doi: 10.1121/1.1772399.

[26] J. F. Patrick, P. A. Busby, and P. J. Gibson, “The Development of the Nucleus®Freedom™ Cochlear Implant System,” *Trends Amplif.*, vol. 10, no. 4, pp. 175–200, 2006, doi: 10.1177/1084713806296386.

[27] J. M. Bronstein *et al.*, “Deep brain stimulation for Parkinson disease an expert consensus and review of key issues,” *Arch. Neurol.*, vol. 68, no. 2, pp. 165–171, 2011, doi: 10.1001/archneurol.2010.260.

[28] M. S. Okun *et al.*, “Subthalamic deep brain stimulation with a constant-current device in Parkinson’s disease: An open-label randomised controlled trial,” *Lancet Neurol.*, vol. 11, no. 2, pp. 140–149, 2012, doi: 10.1016/S1474-4422(11)70308-8.

[29] Y. H. L. Luo and L. da Cruz, “The Argus® II Retinal Prosthesis System,” *Prog. Retin. Eye Res.*, vol. 50, pp. 89–107, 2016, doi: 10.1016/j.preteyeres.2015.09.003.

[30] B. K. Tran and T. J. Wolfensberger, “Retina-Implant Interaction after 16 Months Follow-up in a Patient with an Argus II Prosthesis,” *Klin. Monbl. Augenheilkd.*, vol. 234, no. 4, pp. 538–540, 2017, doi: 10.1055/s-0042-121660.

[31] Z. M. Hafed, K. Stingl, K. U. Bartz-Schmidt, F. Gekeler, and E. Zrenner, “Oculomotor behavior of blind patients seeing with a subretinal visual implant,” *Vision Res.*, vol. 118, pp. 119–131, 2016, doi: 10.1016/j.visres.2015.04.006.

[32] T. L. Edwards *et al.*, “Assessment of the Electronic Retinal Implant Alpha AMS in Restoring Vision to Blind Patients with End-Stage Retinitis Pigmentosa,” *Ophthalmology*, vol. 125, no. 3, pp. 432–443, 2018, doi: 10.1016/j.ophtha.2017.09.019.

[33] W. Tong, H. Meffin, D. J. Garrett, and M. R. Ibbotson, “Stimulation Strategies for Improving the Resolution of Retinal Prostheses,” *Front. Neurosci.*, vol. 14, no. March, pp. 0–7, 2020, doi: 10.3389/fnins.2020.00262.

[34] Y. H. Liu *et al.*, “Assessment of neurovascular dynamics during transient ischemic attack by the novel integration of micro-electrocorticography electrode array with functional photoacoustic microscopy,” *Neurobiol. Dis.*, vol. 82, pp. 455–465, 2015, doi: 10.1016/j.nbd.2015.06.019.

[35] K. W. Yang, K. Oh, and S. Ha, “Challenges in Scaling down of Free-Floating Implantable Neural Interfaces to Millimeter Scale,” *IEEE Access*, vol. 8, pp. 133295–133320, 2020, doi: 10.1109/ACCESS.2020.3007517.

[36] K. Agarwal, R. Jegadeesan, Y. X. Guo, and N. V. Thakor, “Wireless Power Transfer Strategies for Implantable Bioelectronics,” *IEEE Rev. Biomed. Eng.*, vol. 10, pp. 136–161, 2017, doi: 10.1109/RBME.2017.2683520.

[37] S. R. Khan, S. K. Pavuluri, G. Cummins, and M. P. Y. Desmulliez, “Wireless power transfer techniques for implantable medical devices: A review,” *Sensors (Switzerland)*, vol. 20, no. 12, pp. 1–58, Jun. 2020, doi: 10.3390/s20123487.

[38] J. Park, C. Kim, A. Akinin, S. Ha, G. Cauwenberghs, and P. P. Mercier, “Wireless powering of mm-scale fully-on-chip neural interfaces,” *2017 IEEE Biomed. Circuits Syst. Conf. BioCAS 2017 - Proc.*, vol. 2018-Janua, pp. 1–4, 2018, doi: 10.1109/BIOCAS.2017.8325186.

[39] IEEE International Committee on Electromagnetic Safety, “IEEE Standard for Safety Levels with Respect to Human Exposure to Electric, Magnetic, and Electromagnetic Fields, 0 Hz to 300 GHz,” 2019.

[40] P. Zradziński, “Modelling and Evaluating Electromagnetic Field Exposure in the Multiple-Source Scenario of Using IoT HF RFID Readers,” *Int. J. Environ. Res. Public Health*, vol. 19, no. 6, 2022, doi: 10.3390/ijerph19063274.

[41] J. Besnoff, M. Abbasi, and D. S. Ricketts, “High Data-rate communication in near-field RFID and wireless power using higher order modulation,” *IEEE Trans. Microw. Theory Tech.*, vol. 64, no. 2, pp. 401–413, 2016, doi: 10.1109/TMTT.2016.2515586.

[42] G. Retz *et al.*, “A highly integrated low-power 2.4 GHz transceiver using a direct-conversion diversity receiver in 0.18 μm CMOS for IEEE802. 15.4 WPAN,” in *IEEE International Solid-State Circuits Conference-Digest of Technical Papers*, 2009, pp. 414–415.

[43] P. Husted *et al.*, “A single-chip CMOS Bluetooth v. 2.1 radio SoC,” *IEEE Commun. Mag.*, vol. 47, no. 4, pp. 144–151, 2009, doi: 10.1109/MCOM.2009.4907421.

[44] K. Matsushita *et al.*, “Development of an implantable wireless ECoG 128ch recording device for clinical brain machine interface,” *Proc.*

Annu. Int. Conf. IEEE Eng. Med. Biol. Soc. EMBS, pp. 1867–1870, 2013, doi: 10.1109/EMBC.2013.6609888.

[45] K. Matsushita *et al.*, "A fully implantable wireless ECoG 128-channel recording device for human brain–machine interfaces: W-HERBS," *Front. Neurosci.*, vol. 12, no. July, pp. 1–11, 2018, doi: 10.3389/fnins.2018.00511.

[46] H. Ando, K. Takizawa, T. Yoshida, K. Matsushita, M. Hirata, and T. Suzuki, "Wireless Multichannel Neural Recording with a 128-Mbps UWB Transmitter for an Implantable Brain-Machine Interfaces," *IEEE Trans. Biomed. Circuits Syst.*, vol. 10, no. 6, pp. 1068–1078, Dec. 2016, doi: 10.1109/TBCAS.2016.2514522.

[47] S. K. Kelly and J. Rizzo, "The Boston Retinal Implant," *Artif. Vis.*, pp. 85–97, 2017, doi: 10.1007/978-3-319-41876-6_7.

[48] L. da Cruz *et al.*, "Five-Year Safety and Performance Results from the Argus II Retinal Prosthesis System Clinical Trial," *Ophthalmology*, vol. 123, no. 10, pp. 2248–2254, 2016, doi: 10.1016/j.ophtha.2016.06.049.

[49] B. Laha, B. K. Stafford, and A. D. Huberman, "Regenerating optic pathways from the eye to the brain," *Science (80-.).*, vol. 356, no. 6342, pp. 1031–1034, 2017, doi: 10.1126/science.aal5060.

[50] E. J. Chichilnisky and R. S. Kalmar, "Functional Asymmetries in ON and OFF Ganglion Cells of Primate Retina," *J. Neurosci.*, vol. 22, no. 7, pp. 2737–2747, 2002, doi: 10.1523/jneurosci.22-07-02737.2002.

[51] T. Guo *et al.*, "Mediating retinal ganglion cell spike rates using high-frequency electrical stimulation," *Front. Neurosci.*, vol. 13, no. APR, pp. 1–12, 2019, doi: 10.3389/fnins.2019.00413.

[52] T. R. Projection, Q. Investigation, C. With, and R. Pathway, "The Retinal Projection to the Thalamus in the Cat : A Quantitative Investigation and a Comparison With the Retinotectal Pathway," *J. Comp. Neurol.*, vol. 285, pp. 265–285, 1981.

[53] J. D. Weiland, S. T. Walston, and M. S. Humayun, "Electrical Stimulation of the Retina to Produce Artificial Vision," *Annu. Rev. Vis. Sci.*, vol. 2, pp. 273–294, 2016, doi: 10.1146/annurev-vision-111815-114425.

[54] E. W. Schmid and W. Fink, "Operational design considerations for retinal prostheses," *IEEE Circuits Syst. Mag.*, vol. 16, no. 3, pp. 31–44, 2016, doi: 10.1109/MCAS.2016.2583678.

[55] R. Liu, Y. Wang, M. Pu, and J. Gao, "Effect of alpha lipoic acid on retinal ganglion cell survival in an optic nerve crush model," *Mol. Vis.*, no. September, pp. 1122–1136, 2016.

[56] X. Liu, M. Zhang, A. G. Richardson, T. H. Lucas, and J. Van Der Spiegel,

"A 12-channel bidirectional neural interface chip with integrated channel-level feature extraction and PID controller for closed-loop operation," *IEEE Biomed. Circuits Syst. Conf. Eng. Heal. Minds Able Bodies, BioCAS 2015 - Proc.*, pp. 8–11, 2015, doi: 10.1109/BioCAS.2015.7348339.

[57] C. C. Chen and K. T. Tang, "A 12V-500μA neuron stimulator with current calibration mechanism in 0.18μm standard CMOS process," *IEEE Biomed. Circuits Syst. Conf. BioCAS*, pp. 57–60, 2011, doi: 10.1109/BioCAS.2011.6107726.

[58] E. Pepin, J. Uehlin, D. Micheletti, S. I. Perlmutter, and J. C. Rudell, "A high-voltage compliant, electrode-invariant neural stimulator front-end in 65nm bulk-CMOS," *Eur. Solid-State Circuits Conf.*, vol. 2016-Octob, pp. 229–232, 2016, doi: 10.1109/ESSCIRC.2016.7598284.

[59] D. Osipov *et al.*, "HV compliant current driver with on-chip read-out protection switch for neural stimulation," *Analog Integr. Circuits Signal Process.*, vol. 92, no. 3, pp. 415–426, 2017, doi: 10.1007/s10470-017-1022-3.

[60] X. Li, S. Zhong, and J. Morizio, "16-Channel biphasic current-mode programmable charge balanced neural stimulation," *Biomed. Eng. Online*, vol. 16, no. 1, p. 104, 2017, doi: 10.1186/s12938-017-0385-0.

[61] Y. J. Jeon, L. Yao, Y. Gao, and M. A. Arasu, "A 0.034% Charge-Imbalanced Neural Stimulation Front-End (SFE) IC with on-Chip Voltage Compliance Monitoring Circuit and Analysis on Resting Potential by Utilizing the SFE IC," *IEEE Trans. Circuits Syst. I Regul. Pap.*, vol. 66, no. 10, pp. 3797–3810, 2019, doi: 10.1109/TCSI.2019.2919333.

[62] J. L. Valtierra, R. Fiorelli, N. Perez-Prieto, M. Delgado-Restituto, and A. Rodriguez-Vazquez, "A High TCMRR, Inherently Charge Balanced Bidirectional Front-End for Multichannel Closed-Loop Neuromodulation," *BioCAS 2019 - Biomed. Circuits Syst. Conf. Proc.*, pp. 7–10, 2019, doi: 10.1109/BIOCAS.2019.8919111.

[63] Y. Zhou, Z. Wang, K. Wang, and R. Wang, "A Closed-loop Controlled Neural Stimulator with High Voltage Compliance in 0.18-μm Low Voltage CMOS Teachnology," *2019 IEEE Int. Conf. Integr. Circuits, Technol. Appl. ICTA 2019 - Proc.*, no. c, pp. 158–159, 2019, doi: 10.1109/ICTA48799.2019.9012885.

[64] C.-E. Lee, Y. Jung, and Y.-K. Song, "8-Channel Biphasic Current Stimulator Optimized for Retinal Prostheses.," *J. Nanosci. Nanotechnol.*, vol. 21, no. 8, pp. 4298–4302, 2021, doi: 10.1166/jnn.2021.19405.

[65] B. Y. R. M. Shapley and J. D. Victor, "The effect of contrast on the transfer properties of cat retinal ganglion cells," *J. Physiol.*, vol. 285, pp.

275–298, 1978.

[66] M. N. Shivdasani *et al.*, “Identification of characters and localization of images using direct multiple-electrode stimulation with a suprachoroidal retinal prosthesis,” *Investig. Ophthalmol. Vis. Sci.*, vol. 58, no. 10, pp. 3962–3974, 2017, doi: 10.1167/iovs.16-21311.

[67] A. G. Rouse *et al.*, “A chronic generalized bi-directional brain-machine interface,” *J. Neural Eng.*, vol. 8, no. 3, 2011, doi: 10.1088/1741-2560/8/3/036018.

[68] M. A. Romero-Laiseca *et al.*, “A Low-Cost Lower-Limb Brain-Machine Interface Triggered by Pedaling Motor Imagery for Post-Stroke Patients Rehabilitation,” *IEEE Trans. Neural Syst. Rehabil. Eng.*, vol. 28, no. 4, pp. 988–996, 2020, doi: 10.1109/TNSRE.2020.2974056.

[69] H. Toda, T. Suzuki, H. Sawahata, K. Majima, Y. Kamitani, and I. Hasegawa, “Simultaneous recording of ECoG and intracortical neuronal activity using a flexible multichannel electrode-mesh in visual cortex,” *Neuroimage*, vol. 54, no. 1, pp. 203–212, 2011, doi: 10.1016/j.neuroimage.2010.08.003.

[70] E. Formaggio *et al.*, “Frequency and time-frequency analysis of intraoperative ECoG during awake brain stimulation,” *Front. Neuroeng.*, vol. 6, no. FEB, pp. 1–8, 2013, doi: 10.3389/fneng.2013.00001.

[71] J. Cho, G. Seong, Y. Chang, and C. Kim, “Energy-Efficient Integrated Circuit Solutions Toward Miniaturized Closed-Loop Neural Interface Systems,” *Front. Neurosci.*, vol. 15, no. May, pp. 1–18, 2021, doi: 10.3389/fnins.2021.667447.

[72] N. V Thakor, “Translating the Brain-Machine Interface,” *Sci. Transl. Med.*, vol. 5, no. 210, pp. 1–8, 2013.

[73] J. Van Der Spiegel, “System-on-a-Chip Brain-Machine-Interface Design - a Review and Perspective,” pp. 3–6, 2016.

[74] A. V. Peterchev, D. L. Murphy, and S. H. Lisanby, “Repetitive transcranial magnetic stimulator with controllable pulse parameters,” *J. Neural Eng.*, vol. 8, no. 3, pp. 2922–2926, 2011, doi: 10.1088/1741-2560/8/3/036016.

[75] Y. T. Li, S. C. Chen, L. Y. Yang, T. H. Hsieh, and C. W. Peng, “Designing and implementing a novel transcranial electrostimulation system for neuroplastic applications: A preliminary study,” *IEEE Trans. Neural Syst. Rehabil. Eng.*, vol. 27, no. 5, pp. 805–813, 2019, doi: 10.1109/TNSRE.2019.2908674.

[76] T. Yousefi *et al.*, “Bidirectional Optogenetic Neuro-Stimulator,” vol. 14, no. 6, pp. 27–30, 2020.

[77] Y. Jia *et al.*, “A mm-Sized Free-Floating Wirelessly Powered

Implantable Optical Stimulating System-on-a-Chip," *IEEE Int. Solid-State Circuits Conf.*, vol. 61, pp. 468–470, 2018, doi: 10.1109/ISSCC.2018.8310387.

[78] H. M. Lee, K. Y. Kwon, W. Li, and M. Ghovanloo, "A wireless implantable switched-capacitor based optogenetic stimulating system," *2014 36th Annu. Int. Conf. IEEE Eng. Med. Biol. Soc. EMBC 2014*, pp. 878–881, 2014, doi: 10.1109/EMBC.2014.6943731.

[79] S. Shahdoost *et al.*, "A miniaturized brain-machine-spinal cord interface (BMSI) for closed-loop intraspinal microstimulation," *Proc. - 2016 IEEE Biomed. Circuits Syst. Conf. BioCAS 2016*, pp. 364–367, 2016, doi: 10.1109/BioCAS.2016.7833807.

[80] T. S. Davis *et al.*, "Restoring motor control and sensory feedback in people with upper extremity amputations using arrays of 96 microelectrodes implanted in the median and ulnar nerves," *J. Neural Eng.*, vol. 13, no. 3, 2016, doi: 10.1088/1741-2560/13/3/036001.

[81] R. Muller, M. M. Ghanbari, and A. Zhou, "Miniaturized Wireless Neural Interfaces: A tutorial," *IEEE Solid-State Circuits Mag.*, vol. 13, no. 4, pp. 88–97, 2021, doi: 10.1109/MSSC.2021.3111387.

[82] S. Casco, I. Fuster, R. Galeano, J. C. Moreno, J. L. Pons, and F. Brunetti, "Towards an ankle neuroprosthesis for hybrid robotics: Concepts and current sources for functional electrical stimulation," *IEEE Int. Conf. Rehabil. Robot.*, pp. 1660–1665, 2017, doi: 10.1109/ICORR.2017.8009486.

[83] D. Borton *et al.*, "Corticospinal neuroprostheses to restore locomotion after spinal cord injury," *Neurosci. Res.*, vol. 78, no. 1, pp. 21–29, 2014, doi: 10.1016/j.neures.2013.10.001.

[84] J. T. Ramshur, A. L. De Jongh Curry, and R. S. Waters, "Wireless simultaneous stimulation-and-recording device to train cortical circuits in somatosensory cortex," *2014 36th Annu. Int. Conf. IEEE Eng. Med. Biol. Soc. EMBC 2014*, vol. 38163, pp. 426–429, 2014, doi: 10.1109/EMBC.2014.6943619.

[85] J. P. Wright *et al.*, "A fully implantable wireless bidirectional neuromodulation system for mice," *Biosens. Bioelectron.*, vol. 200, no. September 2021, p. 113886, 2022, doi: 10.1016/j.bios.2021.113886.

[86] E. Greenwald, M. R. Masters, and N. V. Thakor, "Implantable neurotechnologies: bidirectional neural interfaces—applications and VLSI circuit implementations," *Medical and Biological Engineering and Computing*, vol. 54, no. 1. 2016. doi: 10.1007/s11517-015-1429-x.

[87] M. C. Dadarlat and P. N. Sabes, "Encoding and Decoding of Multi-Channel ICMS in Macaque Somatosensory Cortex," *IEEE Trans. Haptics*, vol. 9, no. 4, pp. 508–514, 2016, doi:

10.1109/TOH.2016.2616311.

[88] X. Liu *et al.*, “A Fully Integrated Sensor-Brain-Machine Interface System for Restoring Somatosensation,” *IEEE Sens. J.*, vol. 21, no. 4, pp. 4764–4775, 2021, doi: 10.1109/JSEN.2020.3030899.

[89] E. L. Graczyk, B. P. Delhaye, M. A. Schiefer, S. J. Bensmaia, and D. J. Tyler, “Sensory adaptation to electrical stimulation of the somatosensory nerves,” *J. Neural Eng.*, vol. 15, no. 4, 2018, doi: 10.1088/1741-2552/aab790.

[90] A. J. Herrera, E. C. Tyler-kabara, and M. L. Boninger, “A brain-computer interface that evokes tactile sensations improves robotic arm control,” *Neuroscience*, vol. 836, no. May, pp. 831–836, 2021.

[91] R. Tegner, “Tactile sensibility in parietal lesions,” *J. Neurol. Neurosurg. Psychiatry*, vol. 52, no. 5, pp. 669–670, 1989, doi: 10.1136/jnnp.52.5.669.

[92] E. Grayver and B. Daneshrad, “A low-power all-digital FSK receiver for space applications,” *IEEE Trans. Commun.*, vol. 49, no. 5, pp. 911–921, 2001, doi: 10.1109/26.923814.

[93] M. Zhou, M. R. Yuce, W. Liu, and S. Member, “A Non-Coherent DPSK Data Receiver With Interference Cancellation for Dual-Band Transcutaneous Telemetries,” *IEEE J. Solid-State Circuits*, vol. 43, no. 9, pp. 2003–2012, 2008, doi: 10.1109/JSSC.2008.2001881.

[94] Y. Yao, J. Wu, Y. Shi, and F. F. Dai, “A fully integrated 900-MHz passive RFID transponder front end with novel zero-threshold RF-DC rectifier,” *IEEE Trans. Ind. Electron.*, vol. 56, no. 7, pp. 2317–2325, 2009, doi: 10.1109/TIE.2008.2010180.

[95] J. Harries *et al.*, “A realistic phantom of the human head for PET-MRI,” *EJNMMI Phys.*, vol. 7, no. 1, 2020, doi: 10.1186/s40658-020-00320-z.

[96] W. Wang, S. S. Chan, D. A. Heldman, and D. W. Moran, “Motor cortical representation of position and velocity during reaching,” *J. Neurophysiol.*, vol. 97, no. 6, pp. 4258–4270, 2007, doi: 10.1152/jn.01180.2006.

[97] T. Pistohl, T. Ball, A. Schulze-Bonhage, A. Aertsen, and C. Mehring, “Prediction of arm movement trajectories from ECoG-recordings in humans,” *J. Neurosci. Methods*, vol. 167, no. 1, pp. 105–114, 2008, doi: 10.1016/j.jneumeth.2007.10.001.

[98] J. C. Sanchez, A. Gunduz, P. R. Carney, and J. C. Principe, “Extraction and localization of mesoscopic motor control signals for human ECoG neuroprosthetics,” *J. Neurosci. Methods*, vol. 167, no. 1, pp. 63–81, 2008, doi: 10.1016/j.jneumeth.2007.04.019.

[99] “Kubánek et al._2009_Decoding flexion of individual fingers using

electrocorticographic signals in humans.pdf."

[100] P. Khanna and J. M. Carmena, "Beta band oscillations in motor cortex reflect neural population signals that delay movement onset," *Elife*, vol. 6, pp. 1–31, 2017, doi: 10.7554/eLife.24573.

[101] Y. Su, S. Routhu, K. S. Moon, S. Q. Lee, W. S. Youm, and Y. Ozturk, "A wireless 32-channel implantable bidirectional brain machine interface," *Sensors (Switzerland)*, vol. 16, no. 10, pp. 1–18, 2016, doi: 10.3390/s16101582.

[102] A. Zhou *et al.*, "A wireless and artefact-free 128-channel neuromodulation device for closed-loop stimulation and recording in non-human primates," *Nat. Biomed. Eng.*, vol. 3, no. 1, pp. 15–26, 2019, doi: 10.1038/s41551-018-0323-x.

[103] A. Nurmikko, "Challenges for Large-Scale Cortical Interfaces," *Neuron*, vol. 108, no. 2, pp. 259–269, 2020, doi: 10.1016/j.neuron.2020.10.015.

[104] Y. Tanabe, T. Chang, A. J. Yeh, and A. S. Y. Poon, "A small dual-band asymmetric dipole antenna for 13.56 MHz power and 2.45 GHz data transmission," *IEEE Antennas Wirel. Propag. Lett.*, vol. 13, no. c, pp. 1120–1123, 2014, doi: 10.1109/LAWP.2014.2330496.

[105] A. Sharma, E. Kampianakis, and M. S. Reynolds, "A Dual-Band HF and UHF Antenna System for Implanted Neural Recording and Stimulation Devices," *IEEE Antennas Wirel. Propag. Lett.*, vol. 16, pp. 493–496, 2017, doi: 10.1109/LAWP.2016.2585650.

[106] B. C. Johnson *et al.*, "StimDust: A 6.5mm3, wireless ultrasonic peripheral nerve stimulator with 82% peak chip efficiency," *2018 IEEE Cust. Integr. Circuits Conf. CICC 2018*, pp. 1–4, 2018, doi: 10.1109/CICC.2018.8357047.

[107] A. H. Lee, J. Lee, J. Jang, A. Nurmikko, and Y. K. Song, "Wireless Addressable Cortical Microstimulators Powered by Near-Infrared Harvesting," *ACS Sensors*, vol. 6, no. 7, pp. 2728–2737, 2021, doi: 10.1021/acssensors.1c00813.

[108] L. G. Tran, H. K. Cha, and W. T. Park, "A compact wireless power transfer system at 915 MHz with supercapacitor for optogenetics applications," *Sensors Actuators, A Phys.*, vol. 285, pp. 386–394, 2019, doi: 10.1016/j.sna.2018.11.029.

[109] M. Ghovanloo and K. Najafi, "A wireless implantable multichannel microstimulating system-on-a-chip with modular architecture," *IEEE Trans. Neural Syst. Rehabil. Eng.*, vol. 15, no. 3, pp. 449–457, 2007.

[110] A. Khalifa *et al.*, "The Microbead: A 0.009 mm3 Implantable Wireless Neural Stimulator," *IEEE Trans. Biomed. Circuits Syst.*, vol. 13, no. 5, pp. 971–985, 2019, doi: 10.1109/TBCAS.2019.2939014.

[111] A. Khalifa *et al.*, "The Microbead: A Highly Miniaturized Wirelessly Powered Implantable Neural Stimulating System," *IEEE Trans. Biomed. Circuits Syst.*, vol. 12, no. 3, pp. 521–531, 2018, doi: 10.1109/TBCAS.2018.2802443.

[112] Z. Yu *et al.*, "MagNI: A Magnetoelectrically Powered and Controlled Wireless Neurostimulating Implant," *IEEE Trans. Biomed. Circuits Syst.*, vol. 14, no. 6, pp. 1241–1252, Dec. 2020, doi: 10.1109/TBCAS.2020.3037862.

[113] J. Charthad *et al.*, "A mm-Sized wireless implantable device for electrical stimulation of peripheral nerves," *IEEE Trans. Biomed. Circuits Syst.*, vol. 12, no. 2, pp. 257–270, 2018, doi: 10.1109/TBCAS.2018.2799623.

[114] X. Li, H. Zhong, Z. Tang, and C. Jia, "Reliable antifuse one-time-programmable scheme with charge pump for postpackage repair of DRAM," *IEEE Trans. Very Large Scale Integr. Syst.*, vol. 23, no. 9, pp. 1956–1960, 2015, doi: 10.1109/TVLSI.2014.2354836.

[115] J. Lee *et al.*, "Wireless ensembles of sub-mm microimplants communicating as a network near 1 GHz in a neural application," 2020. doi: 10.1101/2020.09.11.293829.

[116] K. Yang, Q. Dong, D. Blaauw, and D. Sylvester, "A 553F2 2-transistor amplifier-based Physically Unclonable Function (PUF) with 1.67% native instability," *Dig. Tech. Pap. - IEEE Int. Solid-State Circuits Conf.*, vol. 60, pp. 146–147, 2017, doi: 10.1109/ISSCC.2017.7870303.

[117] G. E. Suh and S. Devadas, "Physical unclonable functions for device authentication and secret key generation," *Proc. - Des. Autom. Conf.*, pp. 9–14, 2007, doi: 10.1109/DAC.2007.375043.

[118] G. G. and D. G. N. Rani, "Review—Power Approaches for Biosensors based Bio-Medical Devices," *ECS J. Solid State Sci. Technol.*, vol. 9, no. 12, p. 121005, 2020, doi: 10.1149/2162-8777/abcdfd.

[119] H. Bhamra, Y. W. Huang, Q. Yuan, and P. Irazoqui, "An Ultra-Low Power 2.4 GHz Transmitter for Energy Harvested Wireless Sensor Nodes and Biomedical Devices," *IEEE Trans. Circuits Syst. II Express Briefs*, vol. 68, no. 1, pp. 206–210, 2021, doi: 10.1109/TCSII.2020.3005332.

[120] H. Lyu, A. Babakhani, and S. Member, "A 13.56-MHz− 25-dBm-Sensitivity Inductive Power Receiver System-on-a-Chip With a Self-Adaptive Successive Approximation Resonance Compensation Front-End for Ultra-Low-Power Medical Implants," *IEEE Trans. Biomed. Circuits Syst.*, vol. 15, no. 1, pp. 80–90, 2021.

[121] Y. Il Kim and S. S. Lee, "A capacitorless LDO regulator with fast feedback technique and low-quiescent current error amplifier," *IEEE*

Trans. Circuits Syst. II Express Briefs, vol. 60, no. 6, pp. 326–330, 2013, doi: 10.1109/TCSII.2013.2258250.

[122] Y. P. Lin and K. T. Tang, "An Inductive Power and Data Telemetry Subsystem with Fast Transient Low Dropout Regulator for Biomedical Implants," *IEEE Trans. Biomed. Circuits Syst.*, vol. 10, no. 2, pp. 435–444, 2016, doi: 10.1109/TBCAS.2015.2447526.

[123] H. Lyu, J. Wang, J. H. La, J. M. Chung, and A. Babakhani, "An Energy-efficient Wirelessly Powered Millimeter-scale Neurostimulator with Optimized Inductive Loop Antenna and Custom Rectifier," *IEEE MTT-S Int. Microw. Symp. Dig.*, vol. 2018-June, no. 5, pp. 1401–1404, 2018, doi: 10.1109/MWSYM.2018.8439143.

[124] S. Y. Lee, P. H. Cheng, C. F. Tsou, C. C. Lin, and G. S. Shieh, "A 2.4 GHz ISM Band OOK Transceiver with High Energy Efficiency for Biomedical Implantable Applications," *IEEE Trans. Biomed. Circuits Syst.*, vol. 14, no. 1, pp. 113–124, 2020, doi: 10.1109/TBCAS.2019.2963202.

[125] J. P. Curty, N. Joehl, C. Dehollain, and M. J. Declercq, "Remotely powered addressable UHF RFID integrated system," *IEEE J. Solid-State Circuits*, vol. 40, no. 11, pp. 2193–2202, 2005, doi: 10.1109/JSSC.2005.857352.

[126] R. Guerra *et al.*, "An RF-powered FSK/ASK receiver for remotely controlled systems," *Dig. Pap. - IEEE Radio Freq. Integr. Circuits Symp.*, vol. 2016-July, pp. 226–229, 2016, doi: 10.1109/RFIC.2016.7508292.

Appendix

Appendix I – Map of Blackrock MEA matched with omnetics connector

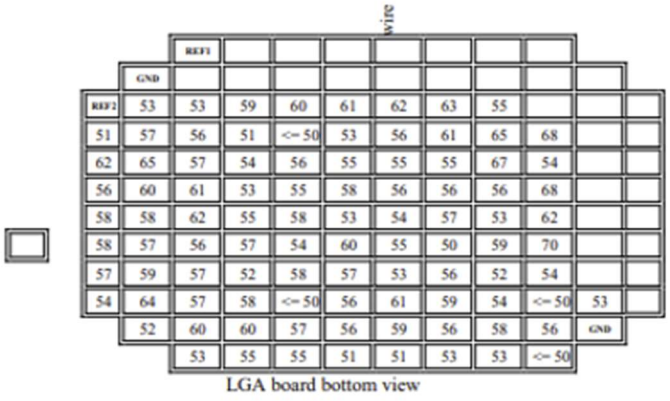

	Elec#	IDC C		Elec#	
65	96	<= 50	56	87	66
67	95	53	58	86	68
69	94	53	56	85	70
71	93	51	59	84	72
73	92	51	56	83	74
75	91	55	57	82	76
77	90	55	60	81	78
79	89	53	60	80	80
81	79	52	57	71	82
83	69	54	64	70	84
85	59	57	59	60	86
87	50	57	58	49	88
89	40	58	58	39	90
91	30	60	56	29	92
93	19	62	65	20	94
95	1	53	51	9	96
		REF2	GND		
		GND	X		

70	53	<= 50	54		62			68	54	
<= 50	56	54	52	59	53	56	67	65	55	
53	58	59	56	50	57	56	55	61	63	
53	56	61	53	55	54	56	55	56	62	
51	59	56	57	60	53	58	55	53	61	wire bundle
51	56	<= 50	58	54	58	55	56	<= 50	60	
55	57	58	52	57	55	53	54	51	59	
55	60	57	57	56	62	61	57	56	53	
53	60	64	59	57	58	60	65	57	53	
	52	54	57	58	58	56	62	51	68	

Electrode Impedance viewing from pad side

NOTE: Impedance values shown as <= are below the detection limits of the Patient Cable impedance tester

Adaptor		IDC A		Adaptor	
pin #	Elec#			Elec#	pin #
1	78	<= 50	53	88	2
3	68	54	70	58	4
5	56	50	62	48	6
7	57	59	68	38	8
9	47	53	54	28	10
11	37	56	67	27	12
13	36	56	68	18	14
15	45	54	65	17	16
17	46	57	55	8	18
19	35	56	61	16	20
21	24	55	63	7	22
23	26	55	62	6	24
25	25	55	61	5	26
27	15	56	60	4	28
29	14	53	59	3	30
31	13	<= 50	53	2	32
33		REF1	GND		*34*
35		GND	X		*36*

Appendix Ⅱ - Si absorption rate

Depth : red 6-7um, green ~1um, blue 0.1um

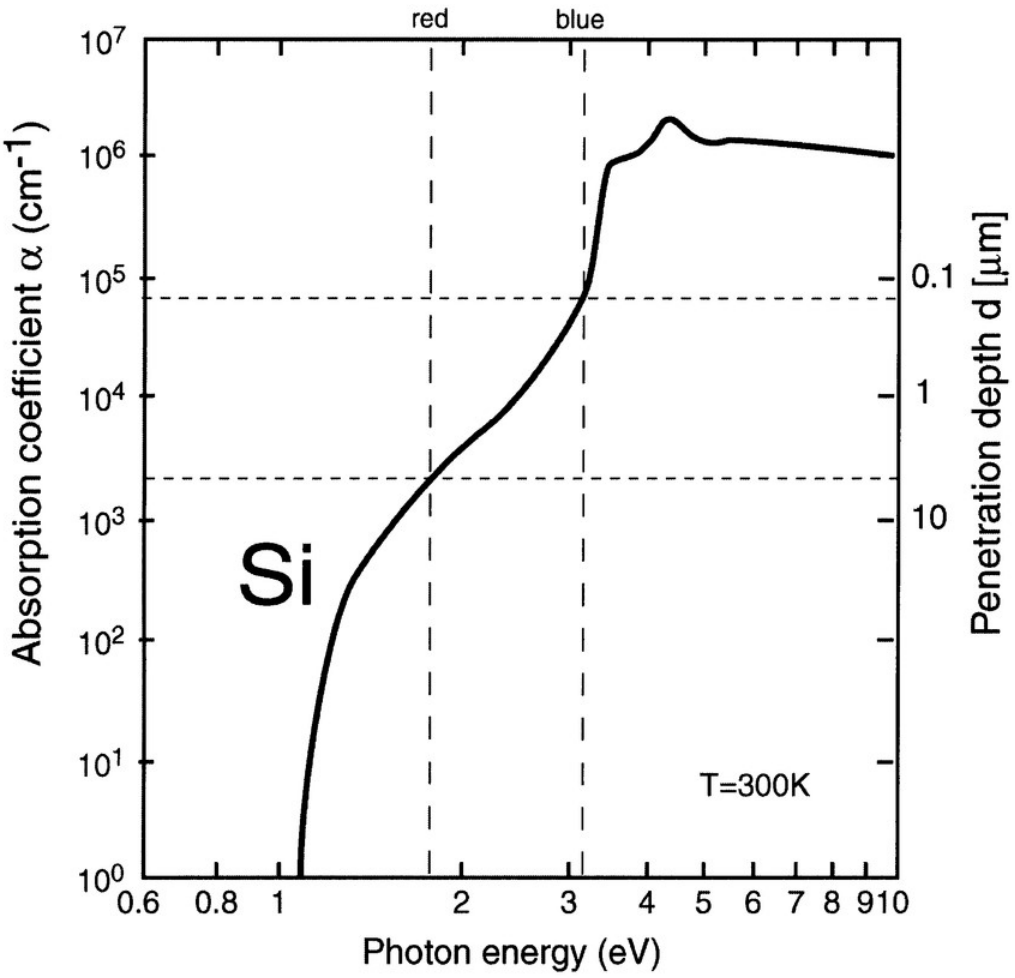

Appendix III- Laser type and popular products according to their wavelength

Laser Line	Laser Type	Popular Fluorophores
~ 405 nm	Diode	DAPI, Hoechst, Alexa Fluor 405™, BFP
~ 440 nm	Diode	CFP
473 nm	Doubled DPSS	
488.0 nm	Ar-ion gas	GFP, FITC, Alexa Fluor 488™
~ 488 nm	Doubled OPS	
514.5 nm	Ar-ion gas	YFP, Rhodamine
515.0 nm	Doubled DPSS	
561.4 nm	Doubled DPSS	TRITC, Cy3™, RFP
568.2 nm	Kr-ion gas	
593.5 nm	Doubled DPSS	Texas Red, mCherry (mRFP)
632.8 nm	HeNe gas	
~ 635 nm	Diode	Cy5™, Alexa Fluor 647™
647.1 nm	Kr-ion gas	

국문 초록

인공지능을 비롯하여 사람의 신경 네트워크에 관한 관심이 높아지면서 뇌 인터페이스에 관한 연구도 활발히 진행되고 있다. 뇌 인터페이스란 전기 신호의 형태로 발생하는 뇌 및 신경 네트워크의 활동을 기록 또는 자극하여 분석 또는 조절하는 기술이다. 여기서 신경 네트워크에 외부 자극을 가하여 인위적으로 원하는 데이터를 인코딩하는 기술은 손상된 감각 신경을 대체하여 감각을 활성화하는 데 활용되고 있다. 일반적으로 뇌 인터페이스 기기와 연결된 전극에서 전기적 자극을 세포에 인가하여 활동 전위를 일으키는 방식이 사용된다. 이러한 뇌 인터페이스 기기의 초소형화 및 네트워킹 기술의 다양화는 반도체 공정 기술과 무선 통신 기술의 눈부신 발전에 기인하였다. 특히 체내에 완전 삽입 가능한 뇌 인터페이스 기기는 감염의 위협을 없애고 심미적인 관점에서 불편함을 없애, 치료용뿐만 아니라 다 학제적으로 연구할 수 있게 하였다.

본 학위 논문에서는 확장형 신경 인터페이스에 사용할 수 있는 다중 채널, 고밀도, 저전력의 무선 초소형 자극기 개발에 대한 내용과, 이를 바탕으로 자극 대상 별 성능을 최적화하며, 최종 목표인 확장형 무선 신경 자극기에 사용될 수 있는 주소부여 방식을 설계하는 방법을 다루고 있다. 이를 위해 먼저 외부 전류 자극의 신경 네트워크 간섭에 대한 개념과 그간의 자극 기기의

개발 이력을 간략히 소개함과 동시에 고밀도 저전력 자극기가 필요한 생물학적, 전자공학적 배경에 관해 기술하고 있다.

체내에 삽입되는 시스템의 경우 시공간적으로 밀집해 있는 신경 조직의 특성상 다채널 고밀도 전극 구조가 요구되며, 자극 방식 및 자극 역치 등에 대한 최적화가 필요하다. 이 학위 논문의 첫 번째 내용은 고밀도의 전기 자극을 위한 높은 출력 임피던스를 갖는 다채널 전류 자극기 개발에 관한 것이다. 저전력 자극회로는 필연적으로 높은 컴플라이언스 전압을 버티지 못하게 되는데, 이를 위해 피드백 회로와 H-브릿지 구조를 변경함으로써 전보다 더 높은 출력 전류를 안정적으로 공급할 수 있게 하였다. 또한, SoC 설계를 통한 무선 다채널 초소형 자극기를 개발하여 다중 채널, 고밀도, 저전력으로 효율적인 신경 자극이 가능한 마이크로 시스템을 제안하였고, 다양한 조직 구조 및 신경 보철에 대한 성능을 검증하는 연구를 수행하였다.

신경자극기는 필연적으로 자극 반응을 관찰하는 분석 기기가 필요하며, 뇌-기계 인터페이스와 같은 양방향 신경 인터페이스 구조에서는 하나의 시스템으로 집적된다. 이때, 시스템의 초소형화를 위해 집적회로에 기록기, 자극기, 무선 데이터 및 전력 송수신 단 등의 구성 요소들이 통합된다. 따라서, 뇌파 기록과 체내 삽입을 위한 저전력 시스템을 바탕으로 한 양방향 뇌-기계 인터페이스 마이크로 시스템을 개발 및 검증하였고, 이 또한 이

논문의 두 번째 부분에서 논의될 것이다.

마지막으로, 광다이오드 주소 생성 회로를 포함한 분산형 자극 시스템의 설계 방법과 분석을 논의한다. 제안된 시스템은 복제 모듈을 확장하여 유연한 다채널 자극기를 만들게 되는데 이때 개별 모듈을 구분 지어줄 주소가 필수적이다. 초소형 집적회로의 특성상 주소부여 회로의 면적을 최소화하며 반도체 공정 후 후처리로 인코딩하는 기술이 요구된다. 이를 위해 알루미늄 패드 없이 광다이오드와 안티-퓨즈를 이용한 주소 생성 회로를 제안하였다.

주요어: 저전력 초소형 자극기, 삽입형 시스템, 감각 신경 보철, 무선 다채널 자극기, 초소형 분산 자극 시스템

학 번: 2017-21784